UNIVERSITÀ DEGLI STUDI DI MILANO

Dipartimento di Chimica

Dottorato in Scienze Chimiche - XXVIII ciclo

Ph.D. Thesis in Chemical Sciences

Electronic transport in graphene-based nanojunctions

Elisabetta del Castillo
Matricola *R10150*

Relatore *Prof. Rocco Martinazzo*
Relatore *Prof. Gian Franco Tantardini*
Correlatore *Dott. Mario Italo Trioni*

Anno Accademico 2014/2015

To my family

Contents

Introduction

On December 10, 1956 Shockley, Bardeen and Brattain were awarded the Nobel Prize in physics "for their researches on semiconductors and their discovery of the transistor effect"[1]. The Bell Labs team invention was the result of the interplay between technological development and theoretical research in solid state physics and would prove to be one of the most outstanding of the past century. Since then, electronics has gone through notable changes, starting from the replacement of the vacuum tubes in circuits to the construction of integrated circuits and microprocessors. Moreover, the miniaturization obeying Moore's law has persistently lead to an exponential increase in the quantity of information that can be processed, stored, and transmitted. Despite the series of successes that industrial laboratories have scored in surmounting one technical and physical barrier after the other, a qualitative change is now in store in terms of the methods of data processing, storing, encoding, and transmission. Miniaturization is in fact reaching a limit where quantum mechanical effects have to be taken into account. Thus, new routes have to be explored looking for reliable alternatives to traditional electronics. Again, a theoretical analysis of the fundamental physics is an indispensable ingredient for the engineering of novel devices based on completely new concepts.

Molecular electronics, spintronics and graphene physics all represent promising fields of investigation for the pursuit of such a compelling goal. In the last years these topics are the object of extensive research and proof of this is the fact that Nobel Prizes have been awarded for discoveries in these fields.

Molecular electronics

Atoms in molecules are bound in specific, controlled configurations. As a result, space and energy are organized very differently in molecules than in solid metals, semiconductors, or insulators. Electronic properties such as polarity, delocalization and charge density are thus specific to a given molecular environment. This sensitivity of electrons to their local environment provides the basis for building electronic functionality into molecular

[1] Nobel Organization citation, 1956.

architectures. For example, when a metal surface is covered with a molecular monolayer, the energy required to pull an electron away from the metal is changed. When a molecular ensemble is placed between two electrodes, electrical charge flows through this junction in a manner specific to the molecule and the contact. When a nanowire is covered with molecules that are sensitive to particular chemical groups, it becomes a sensor. These kinds of functional structures are the simplest examples of what makes up the rapidly growing and dynamic field of research known as molecular electronics.

The first studies conducted on molecular electronics can be traced back to the early 1970s, but the real turning point was represented by the work of Aviram and Ratner who developed a theoretical model indicating that a single molecule could exhibit preferential electronic conduction in one direction along its molecular axis [1]. It was the first time that a single molecule was investigated as a functional building block in electronic devices.

A great advance in molecular electronics development occurred in the 1980s with the invention of the scanning tunneling microscope (STM) and of the atomic force microscope (AFM), two innovating tools that enabled both the production of real-space images of surfaces with a resolution on the sub-nanometre scale and the manipulation of matter at the atomic level. Reports of intriguing electronic behavior began to appear in the 1990s in studies using single molecules and molecular monolayers. In the experimental domain, the realization of metallic atomic-sized contacts produced a significant improvement since they represent the key ingredient for contacting single molecules with dimensions of few nanometers. As a consequence, the field of molecular electronics underwent a very rapid growth. The widespread interest was and is motivated by a multitude of advances that might be possible when incorporating molecular components into microelectronic devices. For example, the potentially diverse electronic functions arising from the numerous degrees of freedom inherent in molecular structure may present new, previously unattainable functions; the promise of lower cost compared to crystalline semiconductors is attractive in manufacturing; and the much smaller size of molecules compared to standard microelectronic components may enable heightened capacities and faster performance. Nevertheless, it took more than 20 years of technological development from the brilliant work of Aviram and Ratner to realize the first transport experiment through single molecules [2]. This event marked the beginning of a long series of variegated experiments in the same spirit.

At the turn of the century, with the introduction of new experimental techniques important results were reported showing that molecules can indeed mimic the behavior of standard electronic components. At the same time, profitable theoretical methods have been developed enabling researchers to investigate the fundamental properties of single molecules under non-equilibrium conditions. All these advances have led and are still leading to the discovery of a multitude of novel effects that attract great attention of

word-wide academic institutions and research laboratories.

It seems unlikely that molecular electronics will replace silicon-based electronics, but there are good reasons to believe that it may complement it in terms of novel functionalities emerging at the nanoscale level which can integrate the standard ones. Last but not least, it should be noted that from the point of view of fundamental science molecular junctions are ideal systems to investigate electronic conduction at a scale dominated by quantum effects, and to shed light into the fundamental electron transfer mechanisms that play a key role both in chemistry and biology.

Spintronics

Magnetoresistance, a change in the electrical resistance of a conductor caused by an applied magnetic field, was first observed by William Thomson in 1857, whereas the comprehension of physics related to the electron spin - which is the ultimate source of magnetism in most materials - dates back to the work of Paul Dirac, Wolfgang Pauli and others scientists in the golden era of quantum mechanics. Nevertheless, for a long time the electron spin was essentially ignored. Then, in 1988 everything changed when Fert and Grünberg each independently discovered that the electrical resistance of an Fe/Cr multilayer structure depended on the relative orientation of the magnetization of the magnetic layers [3, 4]. The discovery of the so-called Giant Magnetoresistance (GMR) marked the birth of spintronics, the study of the role played by the electron spin in solid state physics for the fabrication of devices that exploit spin properties instead of, or in addition to, charge degree of freedom. This pioneering field of investigation immediately attracted the attention of research institutions as well as private companies, the latter interested in possible practical applications. In particular, some researchers at IBM exploited GMR to produce read heads that allowed magnetic disc drives to become smaller while holding eight times more data than before. Now, every single hard disk drive on the market - many ranging up to terabytes and more of storage - features a read head based on their discovery.

All spintronic devices act according to the simple scheme: (1) information is stored (written) into spins as a particular spin orientation (up or down), (2) the spins, being attached to mobile electrons, carry the information along a wire, and (3) the information is read at a terminal. Spin orientation of conduction electrons survives for a relatively long time (nanoseconds, compared to tens of femtoseconds during which electron momentum decays), which makes spintronic devices particularly attractive for memory storage and magnetic sensors applications, and, potentially for quantum computing where electron spin would represent a bit (called qubit) of information.

Current efforts in designing and manufacturing spintronic devices involve two different approaches. The first is perfecting the existing GMR-based technology by either developing new materials with larger spin polarization

of electrons that allow for better spin filtering. The second effort focuses on finding novel ways of both generation and utilization of spin-polarized currents. These include investigation of spin transport in semiconductors and looking for ways in which semiconductors can function as spin polarizers and spin valves. The importance of this effort lies in the fact that the existing metal-based devices do not amplify signals (although they are successful switches or valves), whereas semiconductor based spintronic devices could in principle provide amplification and serve, in general, as multi-functional devices.

The success story of giant magnetoresistance and its broad application to information technology has certainly contributed to the rapid growth of spintronics. But it would be a fallacy to consider the eventual applications more important than the fundamental insight provided by spintronics research. The spin is a purely quantum-mechanical entity and its interaction with the electron charge or the atomic environment provides a unique opportunity to understand the quantum nature of matter.

Graphene

The two-dimensional crystal known as graphene has been the object of theoretical investigations for 70 years as it represents the simplest structure to understand the electronic properties of other graphite materials with different dimensionalities, such as fullerenes (0D) or carbon nanotubes (1D). Actually, for a long time two-dimensional systems were believed non to exist in nature because of their thermodynamic instability. The experimental discovery of graphene in 2004 by Novoselov *et al.* [5] represented a major breakthrough in condensed matter physics since it paved the way to the experimental and theoretical investigations of 2D materials. The original approach to isolate a single graphene layer is the exfoliation technique which consists in using adhesive tape to peel off flakes from three-dimensional graphite. Micromechanical exfoliation is still one of the two most diffuse methods of graphene production, the other being the chemical vapor deposition (CVD), in which gaseous carbon-containing precursors are deposited onto metal substrates. Recently a new method called roll-to-roll has been proposed. Similar to the CVD method, it is believed to lead to the production of high-quality graphene layers at high speeds. Anyway, researchers and engineers are constantly looking for improved manufacturing solutions for graphene at a cost that can make it competitive with the materials it is intended to replace.

The motivation behind this considerable effort for graphene production resides in its manifold and exciting optical, thermal conductivity, electric and mechanical properties that make it an interesting and so far unique material for diversified purposes. For the same reason, in the last decade graphene has been the object of theoretical and experimental investigations by researchers

involved in many fields. In particular, because of its peculiar electronic structure graphene is considered an appealing candidate for exploitation in electronic devices. Tests have shown that mobility of graphene charge carriers is very high, with reported results above 20000 $cm^2V^{-1}s^{-1}$, to be compared with the silicon's value of 1500 $cm^2V^{-1}s^{-1}$. However, the absence of an energy bandgap in graphene limits its fruitful application in electronic switching devices, so the issue of tuning its electronic properties represents a key research topic. Many methods have been studied for this purpose, such as dopings, substrate effects, hydrogenations or atoms adsorption. Thanks to its 2D nature, the induced effects are easier to obtain in graphene with respect to 3D materials, where modifying the surface properties has little effects due to large bulk to surface ratio.

Due to its small spin-orbit coupling, magnetic graphene would be an ideal material for spintronics. However, the field of carbon-based magnetism has always been a controversial area of research which suffered from the poor reproducibility of experimental results. However, the situation seems to have improved over the last few years. Several examples of magnetism in carbon-based materials continue to be reliably reproduced by different research groups. For example, measurements of highly efficient spin information transport and very large spin signals in spintronic devices patterned on epitaxial graphene grown on SiC have been reported.

The dimensional downscaling of silicon-based electronics is approaching its limit, and semiconducting graphene with a sizable band gap could potentially replace silicon in the next generation of high-performance logic circuits. However, until now graphene has not found its ultimate role in integrated electronic devices and researchers keep on investigating all possible aspects that can lead to an advantageous exploitation of this extraordinary material.

Thesis outline

The three fields of investigation outlined above are far from being separated one from the other but are instead intimately related. For instance, organic molecules are routinely investigated as possible active elements of molecular devices. Furthermore, even if spin-related phenomena are usually considered in relation to inorganic materials, experiments have demonstrated that organic materials can preserve the spin information over extremely long times, paving the way to the integration of organic and spin electronics.

In the theoretical investigation of electronic nanojunctions presented in this work we take into account this tight correlation considering graphene as the basic material for magnetic junctions as well as for molecular junctions. Chapter 1 is devoted to the description of our computational method and to the analysis of the main properties of graphene. In Chapter 2 we

study the adsorption of $3d$ transition metals on graphene determining the structural, magnetic and electronic properties. We also investigate the spin-dependent charge transfer from the adatom to graphene and its relation with bond formation. Electronic transport is extensively treated in Chapters 3 and 4. We start with the description of the theoretical approach used for the analysis of the non-equilibrium regime induced by the application of bias voltage. Then Chapter 3 continues with the investigation of the charge transport through a graphene nanojunction adsorbed with different $3d$ transition metals. In Chapter 4 the conductance properties of an organic molecular junctions contacted with graphene leads are investigated. The consequences of the electrodes doping is also taken into account. In the final part we study a possible application of the molecular junction as gas sensor determining the effects of the adsorption of two gas molecules, CO and O_2, on the transmission properties.

Chapter 1

Graphene

In this chapter we describe the main properties of graphene. Being a system extensively studied, we will compare our theoretical results to those already available in literature to test the accuracy of our computational setup.

1.1 Computational methods

We performed first-principles calculations of the structural and electronic properties of graphene within the density functional theory (DFT) framework. We used the Spanish Initiative for Electronic Simulation with Thousand of Atoms (SIESTA) code [6, 7], which employs linear combinations of numerical atomic orbitals to solve the Kohn-Sham equations with three-dimensional periodic boundary conditions (PBC) within a supercell. This is convenient for treating infinite systems such as crystals, but can also handle finite systems by making the supercell sufficiently large separating the objects. The framework in the supercell approach is Bloch's theorem, which states that for a periodic system the electronic wavefunction can be written as a product of a wavelike part and a cell-periodic part, i.e.

$$\psi_{n,\mathbf{k}}(\mathbf{r}) = e^{i\mathbf{kr}} u_{n,\mathbf{k}}(\mathbf{r}), \tag{1.1}$$

where n is a discrete band index and $\mathbf{k}$ is a reciprocal lattice vector belonging to the first Brillouin zone (BZ) corresponding to the supercell. The theorem allows for mapping the Kohn-Sham eigenvalue problem into the reciprocal space, where one can separately obtain for each k-point a discrete set of eigenvalues and eigenstates of the Hamiltonian. The expectation value of some one-body operator $\hat{\mathrm{O}}$ is then calculated as

$$\langle \hat{\mathrm{O}} \rangle = \frac{1}{\Omega_{\mathrm{BZ}}} \int_{\mathrm{BZ}} \mathrm{d}^3\mathrm{k}\, \mathrm{O}(\mathbf{k}) \approx \sum_{\mathbf{k}\in\mathrm{BZ}} w_{\mathbf{k}} \mathrm{O}(\mathbf{k}), \tag{1.2}$$

where for practical purposes the integral over the first BZ with volume Ω_{BZ} is approximated by a sum over k-points with weight factors $w_{\mathbf{k}}$ (adding up to one). In SIESTA the discrete BZ sampling is based on the so-called Monkhorst-Pack scheme [8]. Note that the larger the supercell the smaller the corresponding BZ. For sufficiently large supercells this BZ sampling becomes less critical and using only the Γ-point might be a reasonable approximation. In most DFT implementations pseudopotentials are used to get rid of the core electrons. The idea is to replace the true atomic potential and the chemically inert core electrons with an effective potential - the pseudopotential - that provides the same description for the valence electrons. As a result the computations simplify since just the solution for the valence electronic structure is calculated. In SIESTA norm-conserving pseudopotentials according to the Troullier-Martins [9] parametrization can be used. The numerical solution of the Kohn-Sham equation implies a finite basis set for the representation of the wave functions. The SIESTA method requires the use of atomic-like localized orbitals which guarantee the Hamiltonian and overlap matrix to be sparse. For each atom I positioned at $\mathbf{R}_I$ a set of atom-centered orbitals is defined as a product of a spherical harmonic and a radial function

$$\chi_{Inlm}(\mathbf{r}) = \phi_{Inl}(r_I) Y_{lm}(\hat{\mathbf{r}}_I) \tag{1.3}$$

where the distances are conveniently written in terms of $\mathbf{r}_I = \mathbf{r} - \mathbf{R}_I$ and the angular momentum is labeled by l, m. With a multiple-ζ basis there will be several orbitals (labeled n) corresponding to the same angular momentum but with different radial dependence. The basis orbitals are strictly confined in the sense that they are zero beyond a cutoff radius which may be different for each radial function and is indirectly specified in terms of a confinement energy. The SIESTA basis implies that the calculation of the overlap matrix and most matrix elements of the Hamiltonian are two-center integrals, which are effectively calculated within Fourier space where the convolution becomes a simple product. However, the density and some Hamiltonian matrix elements are calculated on a real-space grid, whose fineness is conveniently described by an energy grid cutoff. In SIESTA different parametrizations for the local density approximation (LDA) and the generalized gradient approximation (GGA) to the exchange-correlation functional are implemented. For our calculations we selected the GGA functional as described by the Perdew-Burke-Ernzerhof (PBE) [10] which is proved to be one of the functionals that provide the smallest differences between calculated and experimental values in our field of interest [11].

In the next subsections we will see the dependence of the results on the values of some computational parameters. We concentrate on the total energy quantity.

1.1.1 Mesh cutoff

The mesh cutoff is an energy that corresponds to the fineness of the real-space grid used for the calculation of some integrals and for the representation of the charge density. A higher value of the mesh cutoff gives a finer real-space grid and hence a better accuracy, but also a longer computational time. Fig. 1.1 shows the total energy variation as a function of the mesh cutoff. We started assuming a value of 250 Ry and a BZ sampling given by a 36×36 k-point grid and we verified the accuracy of our choice.

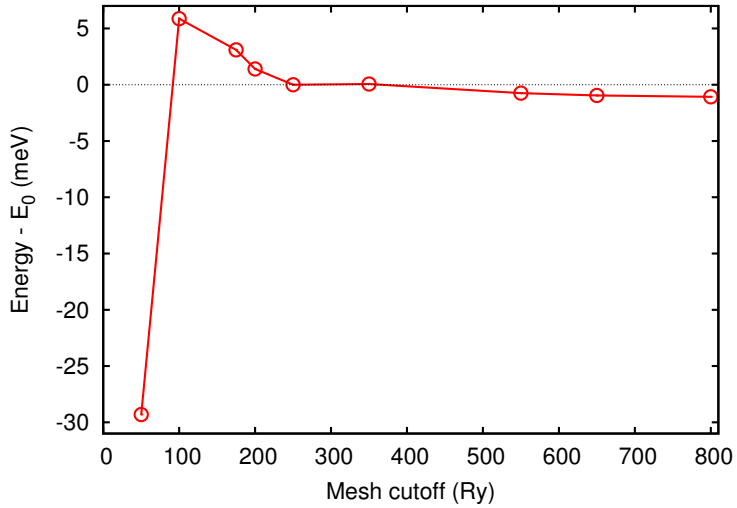

Figure 1.1: Convergence test of the mesh cutoff for a BZ sampling given by a 36×36 k-point grid. The energy values are referred to the total energy E_0 of the graphene unit cell evaluated for a mesh cutoff of 250 Ry.

1.1.2 Egg box effect

All the calculated quantities should be invariant under translation as a whole, but the unavoidable use of a grid breaks translational symmetry. As a consequence, there may be numeric variations of the total energy and of the forces over the atoms, periodic with the step of the mesh grid. To check this effect all the atoms of the system have to be progressively shifted from one point of the grid to the next one. The plot the total energy as a function of the position will resemble to an egg box. For a given mesh cutoff, the fluctuations have to stay within a fixed range. Fig. 1.2 shows the plot of the egg box effect for a mesh cutoff of 250 Ry and, for comparison, the same effect for a mesh cutoff of 100 Ry only. The value of 250 Ry is consistent with a total energy variation of 1 meV, which is the limit that we

consider appropriate for our system.

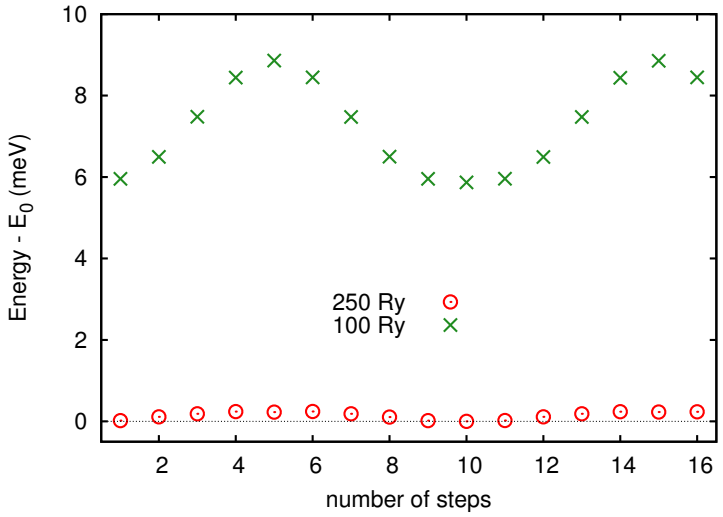

Figure 1.2: Eggbox effect. The space between two consecutive points of the real space grid has been divided in 10 regular intervals. The energy values are referred to the total energy E_0 of the graphene unit cell evaluated for a mesh cutoff of 250 Ry.

1.1.3 k-points grid

Thanks to Bloch's theorem, many integrals do not need to be performed in the real space but can be replaced by calculations in the first Brillouin zone (BZ) of the reciprocal space. In practice these integrals are carried out summing the values of the integrand (e.g. the Fourier transform of the charge density) at a finite number of points in the BZ, called the k-point grid. It is therefore important to select a large enough number of k-points to obtain reliable results.

The lattice vectors $\mathbf{b}_j$ of the reciprocal space depend on the primitive lattice vectors $\mathbf{a}_i$ by means of the relation:

$$\mathbf{a}_i \cdot \mathbf{b}_j = 2\pi\delta_{ij}, \tag{1.4}$$

which for our cell gives:

$$\mathbf{b}_1 = \frac{2\pi}{a}\left(1, -\frac{\sqrt{3}}{3}\right) \qquad \mathbf{b}_2 = \frac{2\pi}{a}\left(0, \frac{2\sqrt{3}}{3}\right). \tag{1.5}$$

The two inequivalent corners K and K′ of the BZ are of special interest

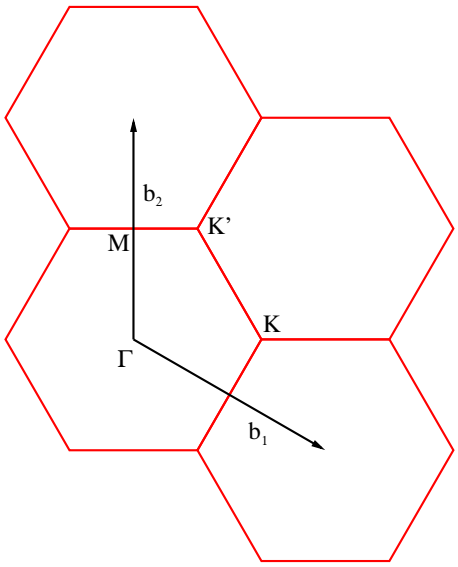

Figure 1.3: Graphene Brillouin zone with the high symmetry points K, K′, M and Γ.

for graphene physics. In fact, in the band structure the valence (π) band and the conduction (π^*) band cross in correspondence with these points, as will be discussed below (see Fig. 1.7). To obtain accurate calculations of the electronic properties it is important to include the high symmetry points K and K′ in the sampling. This can be realized dividing the sides of the cell in the reciprocal space in multiples of 3. Following this rule, the total energy as a function of k-points satisfies the variational principle, as shown in Fig. 1.4. A convenient sampling of the BZ was realized with a

$$\mathbf{k}_1 = (30, 0, 0) \quad \mathbf{k}_2 = (0, 30, 0) \quad \mathbf{k}_3 = (0, 0, 1)$$

grid, which corresponds to 466 k-points.

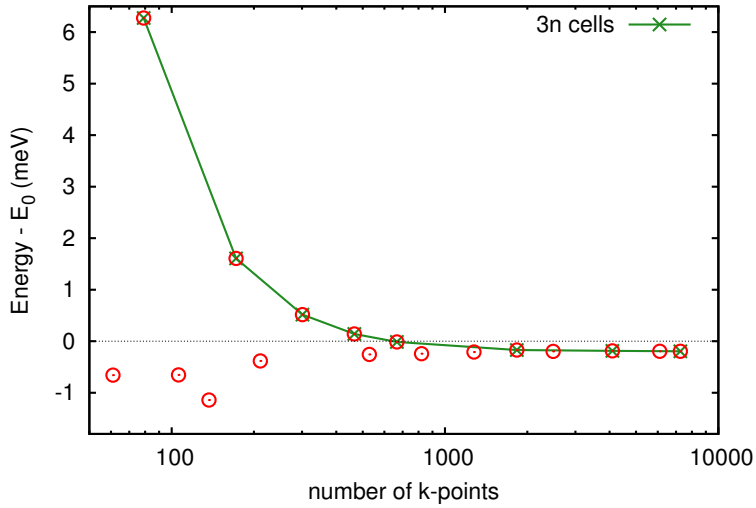

Figure 1.4: Convergence test of the number of k-points. The blue line highlights the grids obtained dividing the sides of the cell in multiples of 3. The energy values are referred to the total energy E_0 of the graphene unit cell with a BZ sampling given by a 36×36 k-point grid and a mesh cutoff of 250 Ry.

1.2 Basis set

Choosing an appropriate basis set is crucial for obtaining reliable results. In our approach we use localized atomic orbitals, i.e. orbitals that are strictly zero beyond a cutoff radius. The quality of this kind of basis can be improved increasing its size. This can be achieved both modifying the radial or the angular part of the wave function. The radial flexibilization is obtained adding one or more orbitals for each angular momentum channel, realizing the so-called double-ζ (DZ), triple-ζ (TZ) and so on basis sets. The angular improvement, crucial to take into account the possible deformations induced by the presence of other atoms, is realized adding shells with different atomic symmetry. The new polarization orbitals are obtained solving the problem of the isolated atom in the presence of a small electric field.

For our calculations we selected a double-ζ polarized (DZP) basis set, which is composed of 13 orbitals: 2 for $l = 0$, 6 for $l = 1$ and 5 for $l = 2$. In Fig. 1.5 are shown the different radial parts of the wave functions.

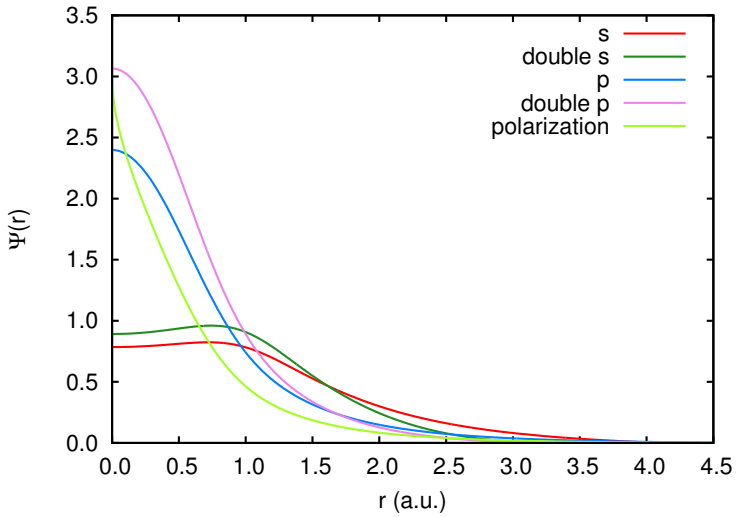

Figure 1.5: Basis set wave functions. Shape of the radial parts for the different angular momentum channels and of the polarization orbital.

1.3 Lattice constant

To determine the value of the lattice constant we analyzed the variation of the total energy E_{tot} with respect to the unit cell volume V (see Fig. 1.6). We fitted the data obtained from our DFT calculations with the Birch-Murnaghan equation of state [12, 13], that for a three dimensional system is:

$$E_{tot}(V) = \tag{1.6}$$
$$E_0 + \frac{9V_0B_0}{16}\left\{\left[\left(\frac{V_0}{V}\right)^{\frac{2}{3}} - 1\right]^3 B_0' + \left[\left(\frac{V_0}{V}\right)^{\frac{2}{3}} - 1\right]^2 \left[6 - 4\left(\frac{V_0}{V}\right)^{\frac{2}{3}}\right]\right\}$$

where V_0 is the equilibrium unit cell volume, V is the unit cell volume, B_0 and B_0' are the bulk modulus and its derivative with respect to the pressure and E_0 is the minimum energy.

Since graphene is a two dimensional material, the lattice constant is derived minimizing the energy with respect to the surface of the unit cell instead of the volume. Using our result of the total energy E_{tot} we calculated the cohesive energy of graphene:

$$E_c = \frac{NE_a - E_{tot}}{N} \tag{1.7}$$

where N is the number of atoms per unit cell and E_a is the total energy of

the isolated carbon atom. We found a value of 7.90 eV, in good agreement with literature results [14, 15]. For the lattice constant our calculated value is 2.474 Å, being the experimental one 2.46±0.02 Å [16].

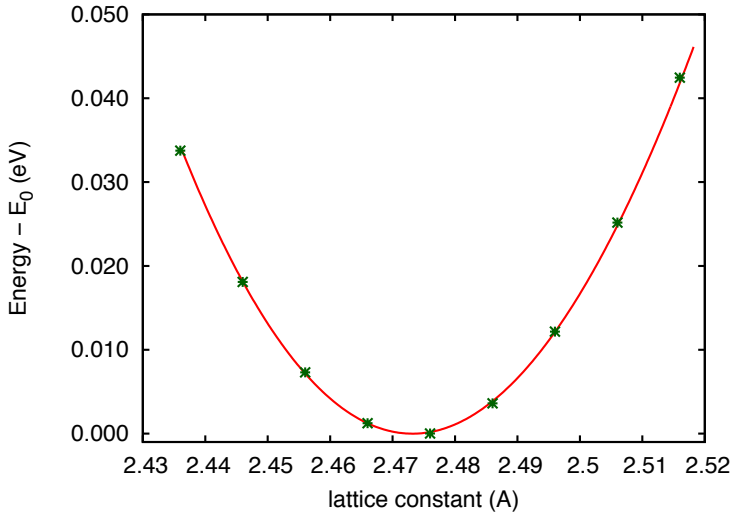

Figure 1.6: Murnaghan fit of the total energy with respect to the lattice constant. The energy values are referred to the minimum value determined with the fitting procedure. In the figure we observe the good correspondence between the data calculated with DFT (green stars) and Birch-Murnaghan equation of state (red line).

1.4 Electronic properties

In Fig. 1.7 are reported the band structure and the density of states (DOS) of pure graphene.

From the left panel we can observe that the Dirac point, i.e. the point where the conduction and the valence graphene π bands cross, is located exactly at the corner K of the Brillouin zone. Near this point the energy-momentum relation shows a linear behavior:

$$E(k) = v_F k\hbar \tag{1.8}$$

typical of massless Dirac fermions [5]. Graphene charge carriers can thus be described as a 2D gas of relativistic particles with zero mass and an effective speed of light $c \approx 10^6$ m/s. A direct consequence of the linear dispersion near K is that the density of states is linear and vanishes at the Fermi level, in contrast with classical two-dimensional electron gas where the density of states is a constant. The unique band structure is responsible

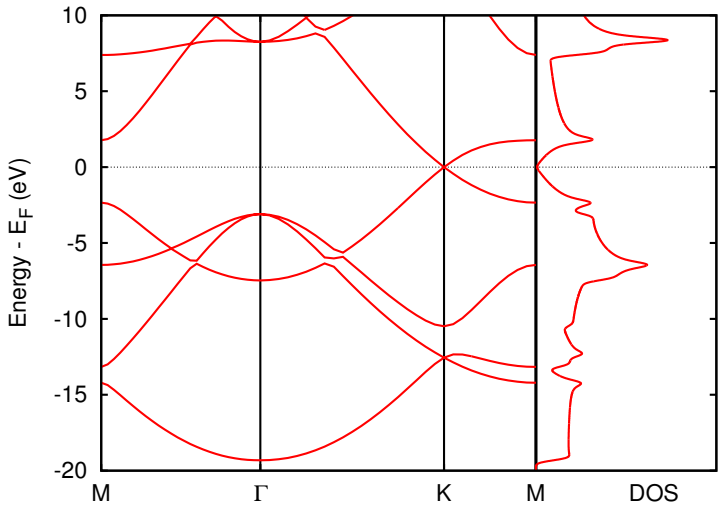

Figure 1.7: Graphene band structure and density of states (DOS). The energy values are referred to the Fermi level.

for the distinct electronic properties of graphene, such as excellent electrical conductivity even at room temperature or quantum Hall effect which make graphene a promising material for nanoelectronics applications.

Chapter 2

Transition metals on graphene

2.1 Introduction

The possibility of tailoring the electronic properties of graphene is crucial for its exploitation in beyond-silicon electronics. In the last years, several ways for engineering a band gap, such as breaking the sublattice symmetry [17], exploiting a strain effect [18] or applying a perpendicular electric field in bilayer graphene [19] have been proposed.

Thanks to its high carriers mobility and small spin orbit coupling graphene is also considered a promising candidate for spintronics applications. However, the realization of graphene-based spin filters or spin valves relies on the possibility of inducing and controlling magnetism in graphene. Many theoretical predictions and experimental evidences showed that dopants, adatoms, defects and edges could lead to the stabilization and manipulation of magnetic states in graphene [20, 21, 22, 23, 24, 25]. Among all proposed techniques to induce magnetism in graphene, the adsorption of transition metals (TM) on graphene is certainly extensively studied, both from theoretical and experimental point of view.

Experimental works span from the observation of n- or p- type doping of graphene upon TM deposition [26, 27] to the investigation of the electronic and magnetic properties of TM on single graphene layer [28]. Theoretical research is devoted to the investigation of structural, electronic and magnetic properties [29, 30, 31, 32].

In this chapter we analyze the structural, electronic and magnetic properties of the magnetic $3d$ transition metals (from Sc, $Z = 21$, to Ni, $Z = 28$) adsorbed on graphene at different coverages. Furthermore we perform a charge transfer analysis to elucidate how the individual majority and minority spin components are distributed in TM@graphene.

All calculations are performed using a standard DZP basis set for carbon

and some of the adatoms. Since preliminary tests showed an overestimation of the binding energies for Sc, Cr, Co and Ni, for these atoms the radii of the basis orbitals have been enlarged following the prescription pointed out in Ref. [33].

The computational setup of our approach, in particular the chosen localized basis set, from one side guarantees a fast and efficient performance as a function of the number of atoms but on the other side shows a smaller accuracy with respect to other possible setups like plane waves-based calculations. This is particularly evident in the calculation of the total energy of the system under investigation because of the well known basis set superposition error (BSSE) [34, 35]. The basic reasons are essentially two: first the pseudo-atomic orbital (PAO) local basis set is not orthogonal and it does not exist a unique prescription to improve its accuracy; second and perhaps more relevant is the fact that different calculations, whose total energies must be successively subtracted one with respect to the other, are performed with different basis sets (and hence with different accuracy). Aware of these facts we corrected all the computed energies by the standard approach, i.e. we used exactly the same basis set for those calculations to be compared, including the so called ghost atoms leaving the atomic basis also for the missing atoms.

The electron densities have been analyzed according to the QTAIM formalism [36].

2.2 Structural properties

Adsorption on graphene is generally considered at three high symmetry sites: hollow (H), at the center of the hexagon, bridge (B), at the midpoint of a C−C bond and top (T), exactly above a C atom.

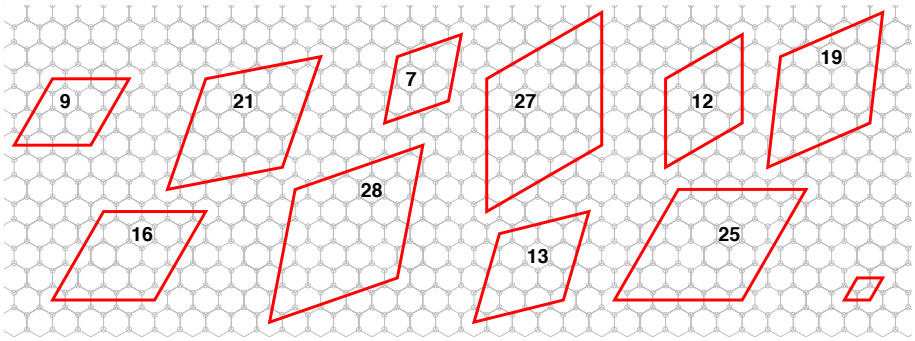

Figure 2.1: The supercells considered. The number inside each cell represents the number of elementary graphene cells included.

Previous theoretical studies proved H as the most stable adsorption site

for all the transition metals considered [37, 38, 39, 29, 40, 41, 30, 42, 43, 44, 31, 45]. Since in the case of Cr, top [41] and bridge sites [39, 44] are also reported as the most stable geometries, we verified that in our calculations Cr adsorbs most favorably in the hollow position, although for a negligible quantity. Hence we selected the center of the hexagon as the most favorable adsorption site for all the transition metals. The different coverages were realized considering rhombic cells containing a different number of elementary graphene cells and adsorbing one atom in each supercell (see Fig. 2.1). In all cases the C_{6v} symmetry for the adsorbate was preserved. The generated supercells can be divided in two classes: those that contain $3n$ graphene unit cells and those containing $3n + 1$ graphene unit cells. In this analysis we neglected the smallest supercells, i.e. very high coverages, because in these cases the properties of the system are essentially governed by the interaction between adatoms while we are mainly interested in the isolated adatom configuration. All the atoms in every supercell were allowed to relax until the residual forces were smaller than 0.01 eV/Å, while the cells were maintained at a constant size.

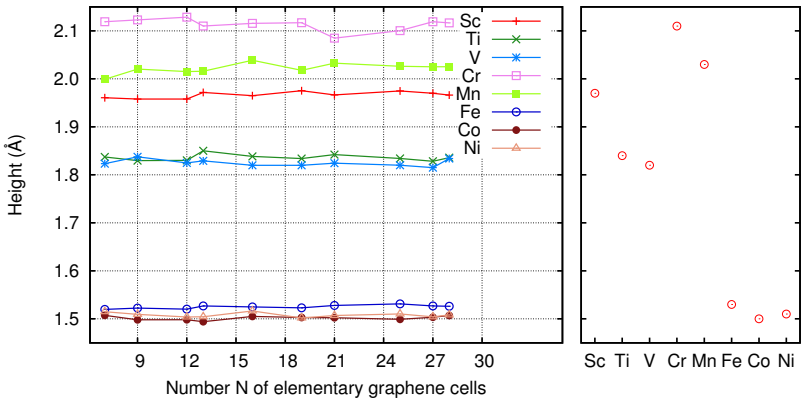

Figure 2.2: Height of the adatoms with respect to the graphene sheet. In the left panel are reported the results for all coverages. In the right panel the average values over the last five coverages (asymptotic values) for all TMs are shown.

The heights of the adatoms, defined as the distance between the TM and the plane containing the six nearest C atoms, are shown in Fig. 2.2 for all the coverages (left panel) and as a function of the atomic number Z (right panel).

Upon adsorption the graphene substrate undergoes a geometrical rearrangement whose major effect is the enlargement of the first neighboring shell. The maximum increase of 0.013 Å (∼1%) occurs in the case of late $3d$ atoms (Fe, Co and Ni). The displacement along z is toward the opposite

Table 2.1: Average Binding energies, magnetic moments, heights, empirical covalent radii, sum of the covalent radii of carbon and the TMs, TM−carbon bond lengths d. All the distances are in Å. The last column shows the differences between the bond length and the radii sum.

TM	$E_B(eV)$	μ (μ_B)	height	r_M	$r_M + r_C$	d_{M-C}	diff. (%)
Sc	1.71	2.24	1.97	1.44	2.21	2.44	10.4
Ti	1.93	3.26	1.84	1.36	2.13	2.33	9.4
V	1.92	4.44	1.82	1.25	2.02	2.32	14.9
Cr	0.30	5.58	2.11	1.27	2.04	2.54	24.5
Mn	0.28	5.44	2.03	1.39	2.16	2.49	15.2
Fe	0.90	2.06	1.53	1.25	2.02	2.10	4.0
Co	1.24	1.11	1.50	1.26	2.03	2.04	0.4
Ni	1.61	0.00	1.51	1.21	1.98	2.02	2.0

side of the adatom and amounts to a maximum value of 0.04 Å for Sc and Ti. Also the shell composed by the second neighboring atoms relaxes outward but with a minor extent. All our results are in overall agreement with previous studies [46, 45, 43, 31, 41, 44].

Table 2.1 shows a comparison between the metal−carbon distances and the sum of the covalent radii (r_M+r_C) of the TM considered. All metal−carbon bonds are longer than the corresponding sum of covalent radii. This is probably due to the fact that when adsorbed at hollow site the metal is bound to six carbon atoms and not to a single one. The difference between the two lengths is substantial (10-20%) except for Fe, Co and Ni, the three atoms with the smaller adsorption height. This late TM atoms adsorb much closer to graphene with respect to the others. The bond lengths follow the behavior suggested by the atomic radii of TM atoms [47] with the exception of Cr and Mn which show a $\sim 20\%$ longer bond length with respect to the sum of the C and TM covalent radii.

The binding energy E_B is calculated through the equation:

$$E_B = E_{\mathrm{Gr}} + E_{\mathrm{TM}} - E_{(\mathrm{TM+Gr})}, \tag{2.1}$$

where $E_{(\mathrm{TM+Gr})}$ is the total energy for the optimized equilibrium configuration of the graphene and the adatom, E_{Gr} is the total energy of pristine graphene, and E_{TM} is that of the isolated adatom. The latter one was calculated using the same pseudopotential of the TM@graphene system.

The results are shown in Fig. 2.3. For almost all adatoms E_B spans from 0.9−1.0 eV (Fe, Co) to 2.0 eV (Sc, Ti), in agreement with previously published results [32, 46, 31, 48]. Differently, Cr and Mn show smaller binding energies (0.30 and 0.28 eV). This behavior is consistent with their adsorption height which is longer than the other $3d$ metals. This point

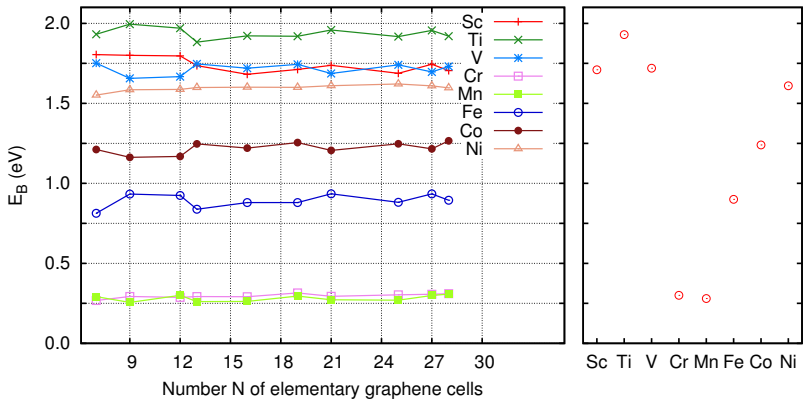

Figure 2.3: Binding energy. In the left panel are reported the results for all coverages. In the right panel the average values over the last five coverages (asymptotic values) for all TMs are shown.

can be understood considering that both Cr and Mn atoms present a filled majority shell and an empty minority one, preventing the formation of a chemical bond and leaving the adatoms only physisorbed on graphene.

Figure 2.4 displays the magnetic moments of the different systems. The discussion of the charge transfer reported in Sec. 2.4 will elucidate the magnetic behaviors of the different systems. We simply note that the adsorption of a TM induces a magnetization except in Ni@graphene, where a rearrangement of the valence electrons results in a filled outer shell.

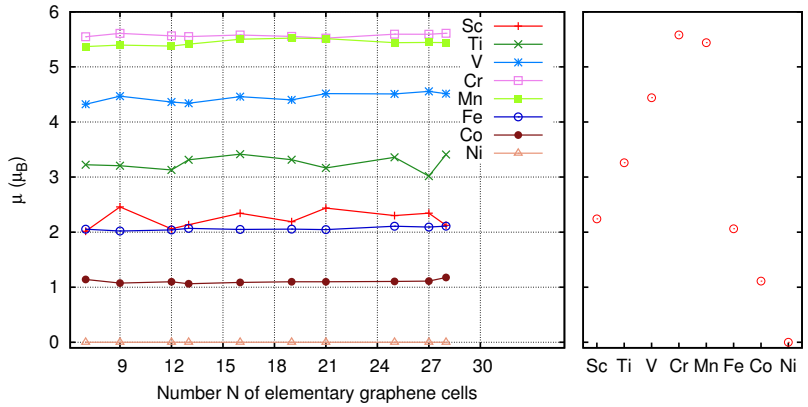

Figure 2.4: Magnetic moment. In the left panel are reported the results for all coverages. In the right panel the average values over the last five coverages (asymptotic values) for all TMs are shown.

2.3 Spectral properties

Graphene is a zero band gap semiconductor. One possible way to modify its electronic behavior is via the adsorption of impurities [49]. If the adsorbate is a magnetic atom, as in our case, different features are expected for the two spin components.

To study the spectral properties we calculated the spin-polarized density of states (DOS) and band structures for all the TM and all the coverages. The first evidence that emerges from an overall analysis of the band structures is the presence of gaps in a specific subset of coverages, i.e. the systems that contain $3n$ graphene unit cells. This feature can be rationalized with topological considerations [50, 51] but it can be easily understood considering the folding of the Brillouin zone (BZ). In the $3n$ class both K and K$'$ points of the graphene unit cell fold to Γ (see Fig. 2.5(a)). In this case the presence of a perturbation removes the degeneracy and yields the opening of a gap in the band structure. In the $3n+1$ class instead K and K$'$ fold to K and K$'$ (see Fig. 2.5(b)) of the new BZ and do not interact.

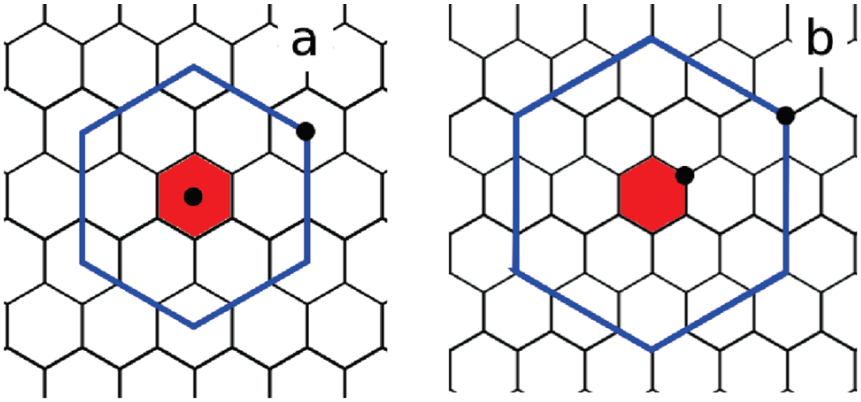

Figure 2.5: Folding of graphene Brillouin zone (BZ, blue line) into the supercell ones (red filled hexagon) for the (*a*) $3n$ and (*b*) $3n+1$ supercells. The K point of graphene BZ is labeled with a black filled dot (from Ref. [51]).

We selected the supercells labeled 27 and 28 (see Fig. 2.1) as representative of the $3n$ and $3n+1$ classes respectively. Their coverages are very similar (1.85% and 1.78%) and sufficiently low to ensure a negligible contribution of the adsorbates interaction to the spectral properties. For comparison in Fig. 2.6 are reported the band structure and the DOS of pristine graphene for the same supercells.

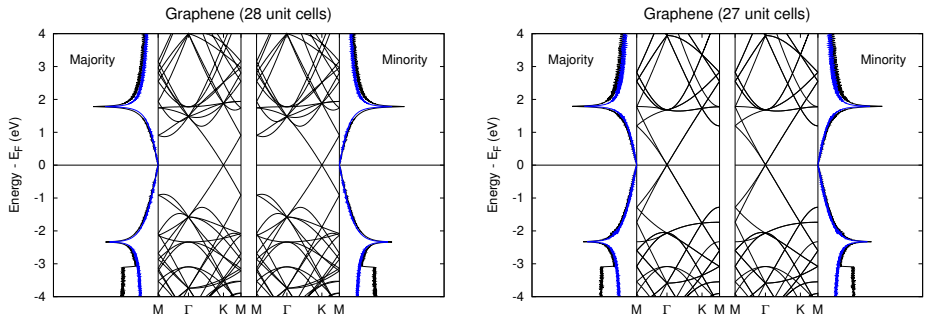

Figure 2.6: Band structure and DOS for the 28 and 27 pristine graphene supercells. π contribution to the DOS are highlighted in blue. Even if graphene is non magnetic, two spin components are depicted for an easier comparison with the other pictures.

2.3.1 Sc

In the left panel of Fig. 2.7 we show the spin resolved DOS and band structure of Sc adsorbed on the 28 supercell. In the majority spin component the band crossing at K typical of graphene is still recognizable at 0.6 eV below the Fermi level. However, moving from K the band structure is affected by the adsorbate electronic states and looses its linear behavior. Focusing on Γ we observe the $4s$ state at 0.3 eV below E_{F} showing a localized atomic character. The five-fold degenerate atomic d orbital spits in three states. The two-fold one displays an e_2 symmetry ($d_{x^2-y^2}$, d_{xy}) and is a bonding state, while the a_1 (d_{z^2}) and the e_2 (d_{xz}, d_{yz}) states lie above the Fermi level. As shown in Fig. 2.8, this coupling is equivalent to what takes place in the case of adsorption of a transition metal atom on a benzene molecule [46]. Moving from Γ the e_1 and e_2 states partially hybridize with carbon states while a_1 preserves its atomic-like shape.

In the minority spin component the rigid downshift of the graphene bands is even more easily distinguishable thanks to the absence of Sc states below the Fermi level. In this case however the rationalization of the $3d$ and $4s$ states is more complex due to the strong hybridization with the substrate.

In the free atomic configuration Sc has three valence electrons ($3d^1 4s^2$). As a consequence of its interaction with graphene some electronic rearrangements take place. Firstly, all the valence electrons show the same spin orientation, i.e. the minority component is empty. Secondly, some bands that in pristine graphene lie above E_{F} are now filled indicating a charge transfer from the adatom to the substrate. Interestingly, both these features are observed for all the transition metals studied.

In the right panel of Fig. 2.7 are shown the band structure and DOS of the 27 supercell. The overall properties, such as the depletion of the

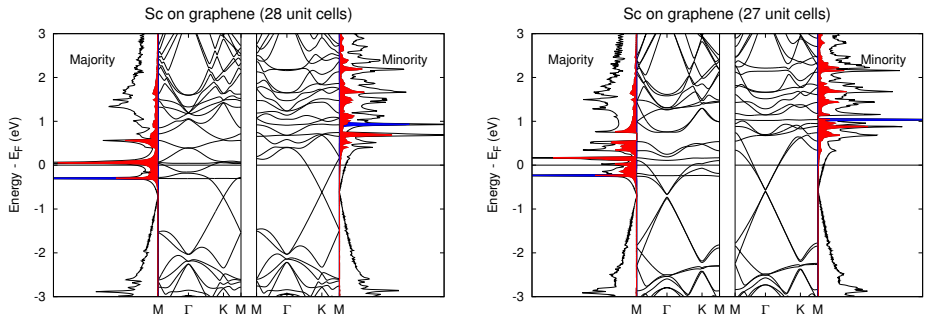

Figure 2.7: Spin-resolved band structure and DOS for the 28 and 27 supercells of Sc adsorbed on graphene. The projected densities of states on the $3d$ and $4s$ orbitals are highlighted in red and blue, respectively.

$4s$ minority orbital or the energetic rearrangement of the five $3d$ majority states are essentially the same of the 28 supercell. However, the feature that mainly characterizes the supercells belonging to the $3n$ class is the presence of gaps in the band structure. Two small gaps ($\sim$0.05 eV) separate the graphene-like bands at -0.7 eV, while other three gaps delimited by the $3d$ adatom bands are located above the Fermi level. The fact that all these gaps do not comprise E_{F} suggests that the properties depending on low energy excitations (e.g. electronic transport or specific heat) should not be influenced by their presence.

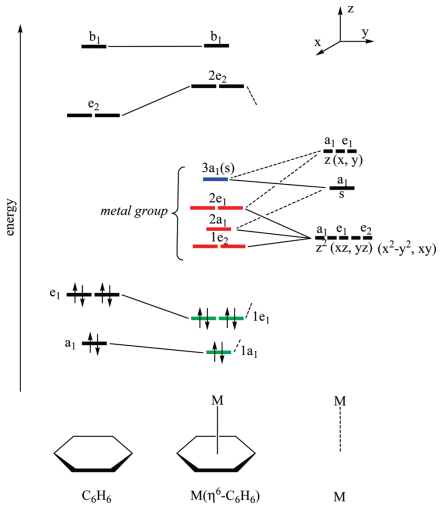

Figure 2.8: Qualitative molecular orbital interaction diagram for TM + C_6H_6 (from Ref. [46]).

2.3.2 Ti-V-Cr

Moving from Sc to higher atomic numbers we find Ti, V and Cr, whose band structure and DOS are displayed in Fig. 2.9. Similarly to what happens with Sc, the adsorption of these atoms on graphene is characterized by the presence of a partially filled majority shell while the minority one is totally empty. A distinct feature is now the position of the 4*s* majority state, which lies at the Fermi level for all the metals and all the coverages. The major characteristics of the 28 supercell are essentially those described for Sc. However, with increasing of the atomic number the Dirac point becomes more and more indistinguishable as a consequence of the hybridization with

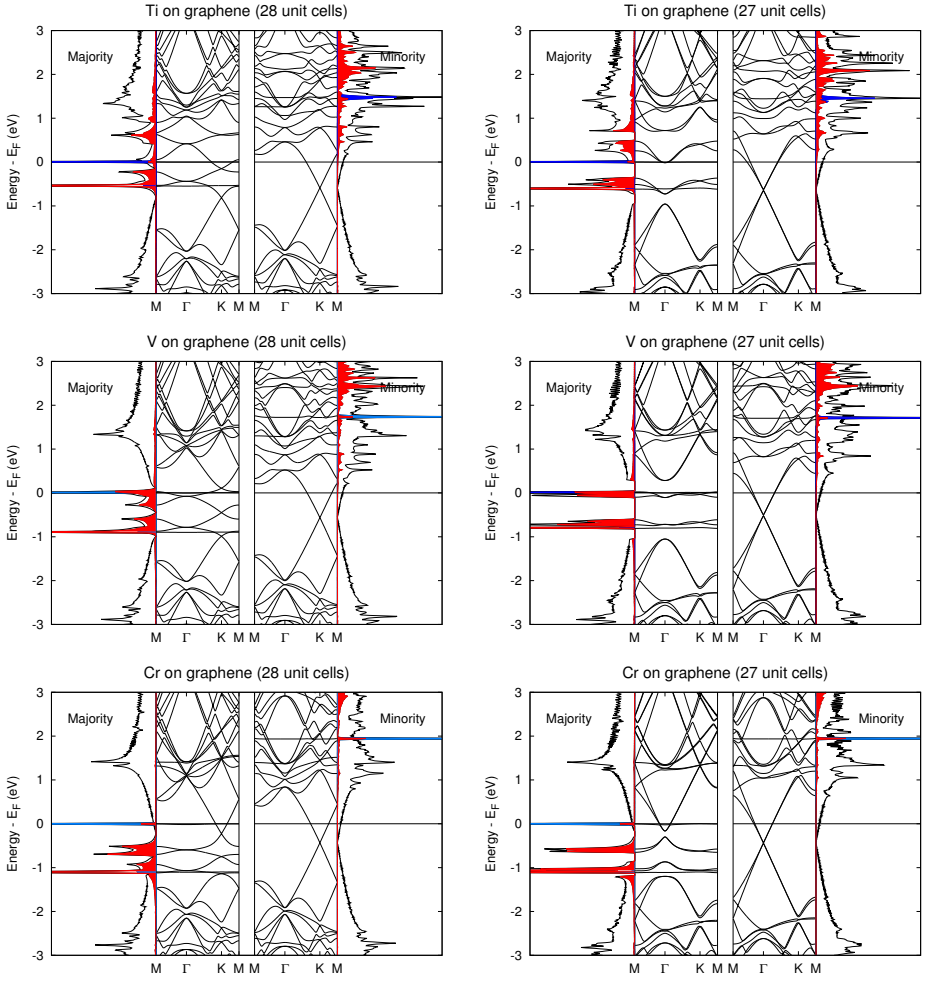

Figure 2.9: Spin-resolved band structure and DOS for the 28 and 27 supercells of Ti, V and Cr adsorbed on graphene. The projected densities of states of the 3*d* and 4*s* orbitals are highlighted in red and blue, respectively.

the substrate. For what concerns the 27 supercell the main feature is the position of the adatoms $3d$ states, which are located at lower energies passing from Ti to Cr. Consequently, the gaps in the majority component happen to lie around the Fermi level. In particular, in case of Ti a gap of about 0.30 eV separating the e_2 and e_1 states is situated just below E_{F}. As concerns V, the $3d$ e_1 states pinned at E_{F} are separated from carbon states (at higher energies) an from other $3d$ states (at lower energies) by two significant gaps amounting at least at 0.30 eV. On the other hand, the minority bands of these three TM display a graphene-like shape but for a downshift already observed for Sc. This notable spin-dependent behavior suggests possible consequences on the electron transport properties of these systems. On the other hand, in case of Cr the $3d$ majority band is completely filled while the minority one is totally empty. The gaps are now located well below E_{F} and should not be relevant for the low excitations properties.

2.3.3 Mn

The adsorption of Mn on graphene results in similar electronic properties for the two coverages analyzed (see Fig. 2.10). In the 28 supercell the $3d$ majority states are totally occupied and lie well below the Fermi level. Also the $4s$ atomic-like majority orbital is full and situated at -0.9 eV.

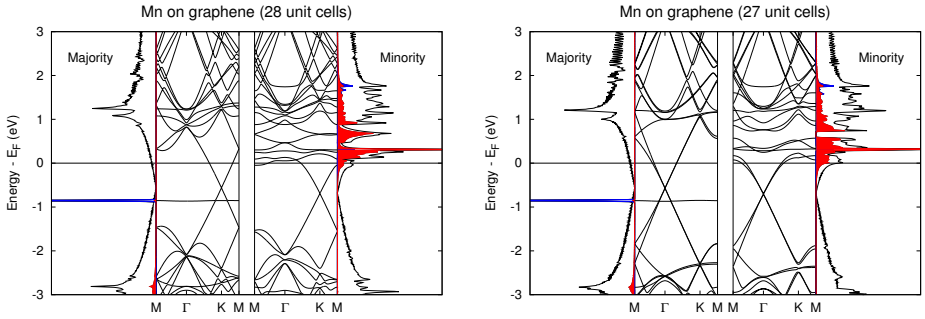

Figure 2.10: Spin-resolved band structure and DOS for the 28 and 27 supercells of Mn adsorbed on graphene. The projected densities of states of the $3d$ and $4s$ orbitals are highlighted in red and blue, respectively.

The Dirac cone is now clearly observable in both spin components, downshifted with respect to E_{F}. The majority bands around the Dirac point display a linear behavior similar to that of the unperturbed system, while in the minority component the bands hybridize with the substrate just above the Fermi level. A feature that is worth mentioning is that, differently from what happens for the TM already discussed, the $4s$ minority state hybridizes with the graphene conduction electrons.

2.3.4 Fe-Co

Figure 2.11 shows the band structures and DOS of Fe and Co adsorbed on graphene. As for Mn, the 3*d* majority orbitals are totally filled, while the 4*s* state is now empty. Comparing the 28 supercells we observe that the spectral properties are essentially indistinguishable for both spin components. The only feature worth mentioning is a minor downshift of the bands in the case of cobalt, clearly noticeable considering the different position of the Dirac point.

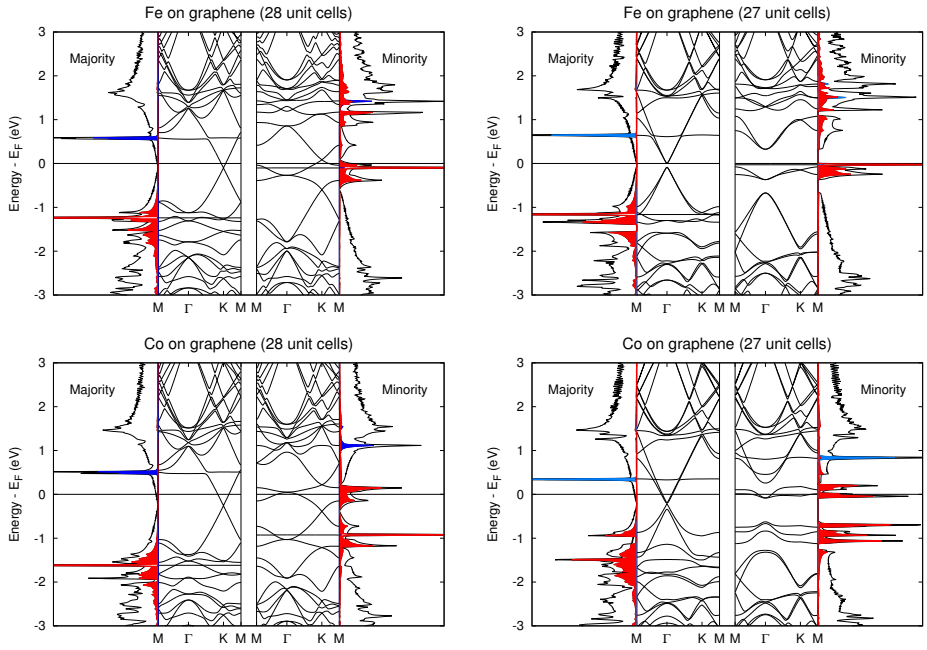

Figure 2.11: Spin-resolved band structure and DOS for the 28 and 27 supercells of Fe and Co adsorbed on graphene. The projected densities of states of the 3*d* and 4*s* orbitals are highlighted in red and blue, respectively.

The gaps that characterize the 27 supercells are now observable in the minority spin component. Here the hybridization of the carbon states with the 3*d* electrons perturbs the graphene bands making the Dirac cone hardly recognizable. Furthermore, just around E_{F} a band gap is observable which separate localized states entirely due to the metal atoms. Also in the majority component a small gap is present, at Fermi level or just below it in the case of Fe and Co, respectively. As for Ti and V, we expect the electronic properties to be influenced by the presence of these gaps. It must be noted that Fe is the only system among those studied herein that presents a semiconductor behavior in both spin components. This fact suggests it could represent an interesting material for electronics applications.

2.3.5 Ni

The ten valence electrons of Ni totally fill the $3d$ orbitals making the system non magnetic (see Fig. 2.12). In both coverages some $3d$ metal states lie just below the Fermi level and hybridize with graphene inducing in the 27 supercell a band gap opening at E_{F}. The band structure above E_{F} is similar to that of unperturbed graphene, while below the Fermi level the linear behavior is hardly recognizable.

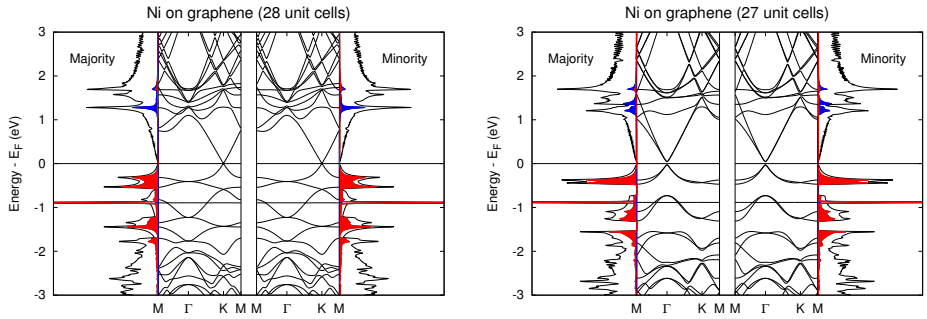

Figure 2.12: Spin-resolved band structure and DOS for the 28 and 27 supercells of Ni adsorbed on graphene. The projected densities of states of the $3d$ and $4s$ orbitals are highlighted in red and blue, respectively.

Even if the adsorption of each transition metal induces specific behaviors some common features can be pointed out. The first evidence that emerges is a rearrangement of the adatom electronic states. As expected, the degeneracy of the $3d$ states is now resolved. Furthermore, we observe a reducing of the $4s$ orbitals binding energies which gives rise to the emptying of the minority components and to the depletion of the majority ones, with the exception of Sc and Mn which retain their $4s$ electron. The $4s$ and d_{z^2} states maintain a strong localized atomic character and do not mix with the graphene bands, while for the other orbitals a significant hybridization with the graphene π bands occurs.

A further notable effect is the formation of gaps in the band structures. A first kind of gap appears at the Dirac point when it folds to Γ, while a different kind of gap causes the spectral confinement of the adatom $3d$ orbitals.

Another common feature is that the Dirac cone is always visible at least in one spin component: from Sc to Mn in the minority one, for Mn to Co in the majority one. In every case (except for Ni) the cone is downshifted with respect to the Fermi level, suggesting a charge transfer from the adatom to graphene.

2.4 Charge transfer

The analysis of the electronic structure of TM@graphene, and more precisely of the charge transfer between the metal and the carbon atoms, has been performed by several research groups [32, 42, 46, 45, 52, 29, 53, 43], adopting a variety of theoretical approaches and criteria. The absolute numbers extracted from the analysis of the wavefunctions differ significantly, most likely due to the different methods of analysis and to the ambiguity of the partitioning schemes, as pointed out by Chan *et al.* [29]. However, several conclusions concur to trace a consistent picture of these systems, as briefly reported below. In 1998 Duffy *et al.* [53] performed a spin-polarized electronic structure calculation of $3d$ transition metals deposited on graphite. The population analysis based on the scheme proposed by Löwdin indicates a small charge transfer from the adatom to the substrate, and a small induced magnetic moment. More recently, an orbital analysis performed by Liu *et al.* [42] has suggested that a significant electron transfer from the TM to the nearest-neighbor carbon atoms takes place, along with the formation of covalent bonding between them. Analogous results have been obtained by Sargolzaei *et al.* [43], which studied the $3d$ transition metals absorbed on graphene and on benzene. These authors concluded that TM behave like cations while graphene and benzene show anionic characters, suggesting that the TM−C interaction has a partial ionic character. The (partial) covalent character of the metal−carbon interactions has been confirmed also by Chan *et al.* [29], based on the energy integration of the DOS of TM@graphene systems and on the analysis of the charge density rearrangement with respect to the isolated metal and graphene subsystems. The electron density analysis of TM@graphene based on the Quantum Theory of Atoms in Molecules (QTAIM) [36] has recently been carried out by Manadé *et al.* [32], and the amount of electron population transferred from the metal atom to car-

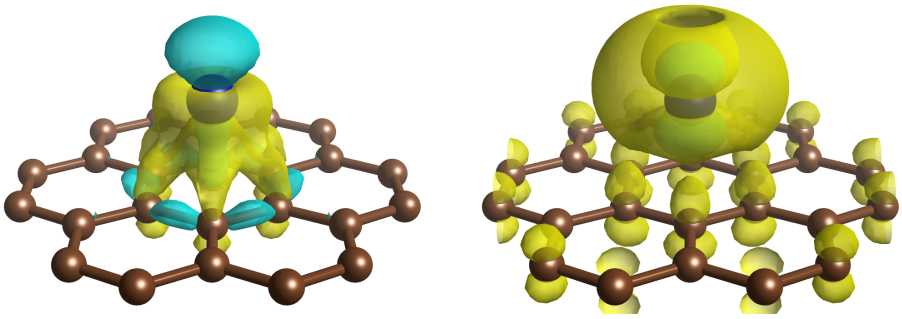

Figure 2.13: Left panel: induced charge density upon Sc adsorption. Right panel: induced spin density upon Sc adsorption. The isosurfaces correspond to $+0.02\ e/\text{Å}^3$ (yellow) and $-0.02\ e/\text{Å}^3$ (light blue).

bons has been rationalized in terms of Pauling electronegativity of the metal atoms.

Overall, most studies agree on saying that $3d$ transition metal atoms transfer electron density to graphene, and that this excess electron population is mainly localized onto the first neighboring carbon atoms. The net electron transfer decreases from Sc to Mn, rises in Fe and then decreases again up to Ni. Furthermore, even if relevant metal to carbon charge transfer occurs, the bonding between TM and C has a significant shared (i.e. covalent) character, with the exception of Cr and Mn which are just physisorbed. Third, the role of the $3d$ orbitals of the metal atom is crucial in determining the bonding properties, since these states may hybridize with the delocalized π structure of graphene.

We perform a charge transfer analysis for the complete series of magnetic $3d$ transition metals from Sc to Ni adsorbed on a 3×3 graphene supercell. To evaluate the effect of the finite size of the supercell adopted, we also perform test computations for a 4×4 graphene supercell in the case of Ti. All the features discussed are confirmed, the largest difference being represented by the overall charge transfer from the metal atom to graphene, which varies by less than 0.05 e.

Differently from Sec. 2.3, for the charge transfer analysis we group the $3d$ elements in three classes: lighter elements Sc, Ti, and V, the intermediate Cr and Mn, and heavier elements Fe, Co, and Ni. The main features common to all systems are that the metal atom transfers charge to graphene, and that the excess electron population of the first shell of neighboring carbon atoms (C_{1st}) nearly counterbalances the overall charge transfer. A residual negative charge is found also onto the second shell of neighbours (C_{2nd}) but in Cr and Mn@graphene, where C_{2nd} is slightly positively charged.

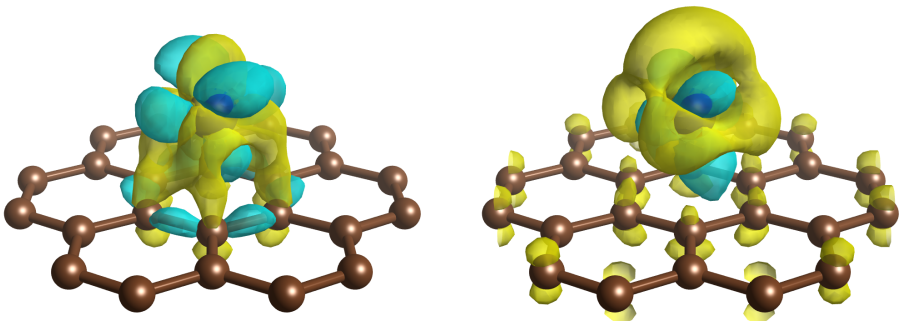

Figure 2.14: Left panel: induced charge density upon Ti adsorption. Right panel: induced spin density upon Ti adsorption. The isosurfaces correspond to $+0.02\ e/\text{Å}^3$ (yellow) and $-0.02\ e/\text{Å}^3$ (light blue).

Table 2.2: Electronic properties of TM@graphene as derived from the QTAIM analysis. [a] In the case of the metal atoms we report the absolute spin up and spin down electron populations, while in the case of graphene (and carbon) we report the excess (positive values) or defect (negative values) population with respect to pristine graphene (6 up and 6 down electrons on each carbon atom). [b] Properties refer to the contribution given by the entire shell of 6 neighbors for C_{1st} and C_{2nd}.

System	charge (e)	mag. mom. (μ_B)	up pop. (e)[a]	down pop. (e)[a]
Sc	1.00	1.56	1.78	0.22
graphene	-1.00	0.85	0.92	0.08
C_{1st}[b]	-0.97	0.55	0.76	0.21
C_{2nd}[b]	-0.02	0.08	0.05	-0.03
Ti	0.93	2.52	2.79	0.27
graphene	-0.93	0.71	0.82	0.11
C_{1st}	-0.91	0.49	0.70	0.21
C_{2nd}	-0.01	0.05	0.03	-0.02
V	0.79	3.72	3.97	0.24
graphene	-0.79	0.69	0.74	0.05
C_{1st}	-0.77	0.34	0.56	0.21
C_{2nd}	-0.01	0.18	0.10	-0.08
Cr	0.44	5.23	5.39	0.17
graphene	-0.44	0.38	0.41	0.03
C_{1st}	-0.50	0.18	0.34	0.16
C_{2nd}	0.03	0.11	0.04	-0.07
Mn	0.59	5.38	5.90	0.51
graphene	-0.59	0.02	0.30	0.29
C_{1st}	-0.60	0.06	0.33	0.27
C_{2nd}	0.01	0.00	-0.01	0.00
Fe	0.79	2.27	4.74	2.47
graphene	-0.79	-0.27	0.26	0.53
C_{1st}	-0.71	-0.23	0.24	0.47
C_{2nd}	-0.03	0.04	0.03	0.00
Co	0.66	1.19	4.77	3.58
graphene	-0.66	-0.14	0.26	0.40
C_{1st}	-0.61	-0.08	0.27	0.35
C_{2nd}	-0.02	-0.04	-0.01	0.03
Ni	0.52	0.00	4.74	4.74
graphene	-0.52	0.00	0.26	0.26
C_{1st}	-0.51	0.00	0.25	0.25
C_{2nd}	0.00	0.00	0.00	0.00

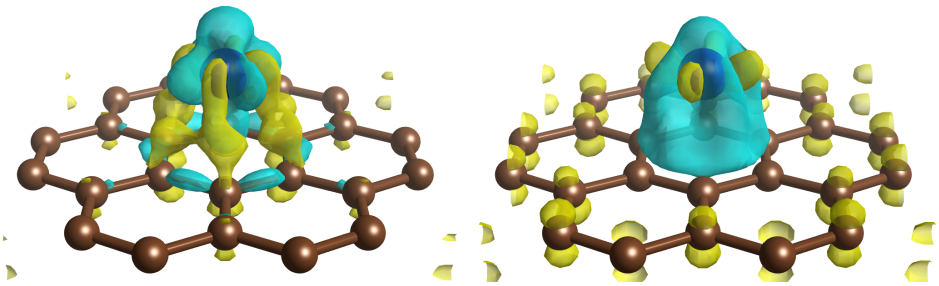

Figure 2.15: Left panel: induced charge density upon V adsorption. Right panel: induced spin density upon V adsorption. The isosurfaces correspond to $+0.02\ e/\text{Å}^3$ (yellow) and $-0.02\ e/\text{Å}^3$ (light blue).

As discussed in Sec. 2.3, the majority states of the lighter TMs hybridize with the states of carbon, while the minority ones are empty and well above the Fermi level. The occupied bands of the minority component are graphene-like but for a downshift of the Dirac cone. The overall charge transfer from the metal atom to graphene slightly decreases with increasing atomic number, from 1.00 e in Sc to 0.79 e in V. Quite interestingly, even if the metals give no orbital contribution to the occupied states of the minority component, their atomic basins contain about 0.2 e of spin down population. The net result is that the electron population of the majority component onto the metal atoms increases more than linearly along the series, from 1.78 e in Sc to 3.97 e in V and, accordingly, the local magnetic moment onto the metal increases from 1.56 μ_B in Sc to 3.72 μ_B in V. In C_{1st} and C_{2nd} the majority spin component is markedly more populated than the minority one, and both exceed the reference values of pristine graphene. In

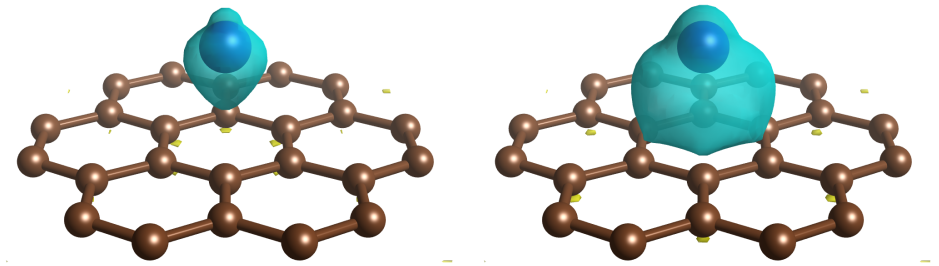

Figure 2.16: Left panel: induced charge density upon Cr adsorption. Right panel: induced spin density upon Cr adsorption. The isosurfaces correspond to $+0.02\ e/\text{Å}^3$ (yellow) and $-0.02\ e/\text{Å}^3$ (light blue).

graphene the small excess of spin down population with respect to neutrality, remains nearly constant along the series of the lighter metals (from 0.05 to 0.11 e depending on the element considered). Accordingly, most of the charge transfer from the metal atoms populates the spin up component of graphene, whose excess with respect to neutrality decreases along the Sc–V series (from 0.92 e in Sc to 0.74 e in V). The net result of this charge redistribution is that the magnetic moment of graphene is non negligible and mostly due to the excess of spin up population of C_{1st}. Its value decreases from 0.85 μ_B in Sc to 0.69 μ_B in V, primarily because of the decrease of the spin up population of C_{1st}. In conclusion, upon adsorption of the lighter metals, graphene enhances the magnetic moment of the adsorbate.

Cr and Mn present peculiar features due to the fact in these systems the $3d$ majority spin states are completely filled, while the minority ones are empty. This occupation gives raise to a close shell configuration. The metal to carbon distances are significantly larger and the binding energies much smaller than in the other systems considered. Consistently with the weakening of the metal–carbon interaction, the charge transfer from these adsorbates to graphene is smaller than discussed above (0.44 e in Cr and 0.59 e in Mn). In Cr the electron population transferred to carbon atoms mainly populates the majority spin component, and hence the total magnetic moment is larger than the one of the metal, as happens for the lighter elements. In the case of Mn, the $3d$ states of the spin down component start to be populated. Because of the downshift of the graphene bands, part of the minority spin electron is transferred to carbon atoms (0.30 e and 0.29 e for up and down component, respectively). Hence the substrate gives no relevant contribution to the total magnetic moment, which measures 5.40 μ_B and is thus equal to the one of the metal (5.38 μ_B). With respect to lighter elements, the spin up population is decreased while the spin down population is significantly increased. This suggests that the charge transfer

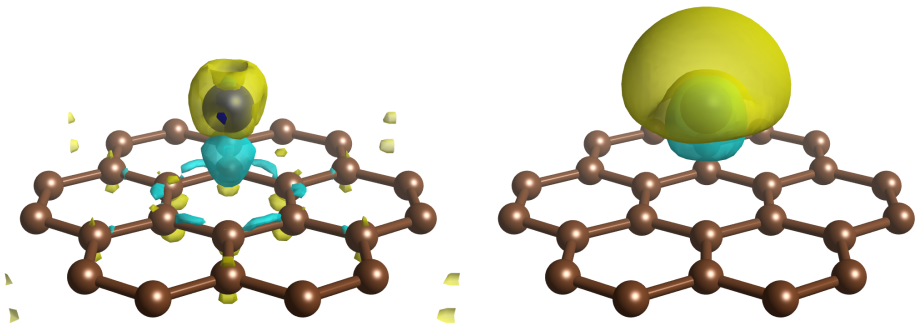

Figure 2.17: Left panel: induced charge density upon Mn adsorption. Right panel: induced spin density upon Mn adsorption. The isosurfaces correspond to $+0.02\ e/\text{Å}^3$ (yellow) and $-0.02\ e/\text{Å}^3$ (light blue).

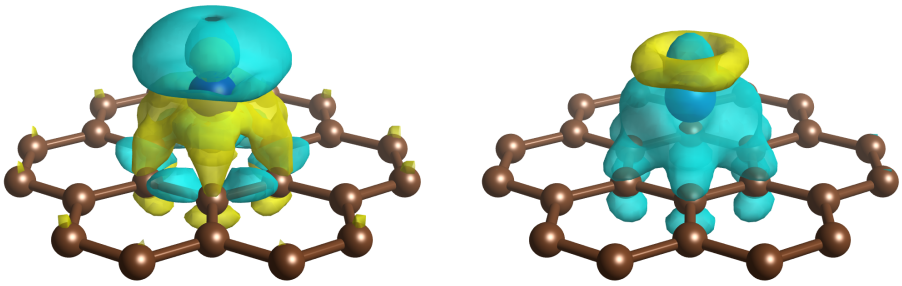

Figure 2.18: Left panel: induced charge density upon Fe adsorption. Right panel: induced spin density upon Fe adsorption. The isosurfaces correspond to $+0.02\ e/\text{Å}^3$ (jellow) and $-0.02\ e/\text{Å}^3$ (light blue).

occurs in the spin component involved in the formation of the bond, that is the component with the partially filled shell. Starting from iron, the $3d$ majority spin shell of the metal atom resides below the Fermi level, while the $3d$ minority spin states lie across the Fermi level and shift downwards up to Ni, where they are entirely occupied. In the heavier elements (Fe, Co, and Ni) the $4s$ orbitals are empty, having transferred their electrons to the $3d$ shell. The spin up population of the metal atoms remains nearly constant at about 4.75 e, while the spin down population increases from 2.47 e in Fe to 4.74 e in Ni. The overall charge transferred from the metal to graphene decreases from 0.79 e in Fe to 0.52 e in Ni. The excess spin up population of graphene does not change significantly along the Fe–Ni series, and measures about 0.25 e. The hybridization between the spin down states of the metal and of graphene results in a relevant excess of spin down population onto carbon atoms, residing mainly onto C_{1st}, but for Ni which is non magnetic.

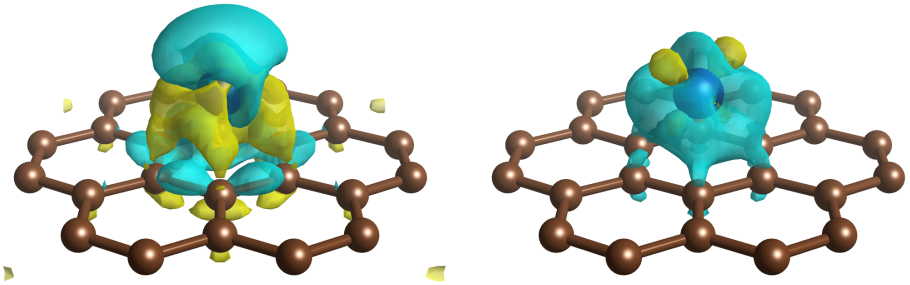

Figure 2.19: Left panel: induced charge density upon Co adsorption. Right panel: induced spin density upon Co adsorption. The isosurfaces correspond to $+0.02\ e/\text{Å}^3$ (yellow) and $-0.02\ e/\text{Å}^3$ (light blue).

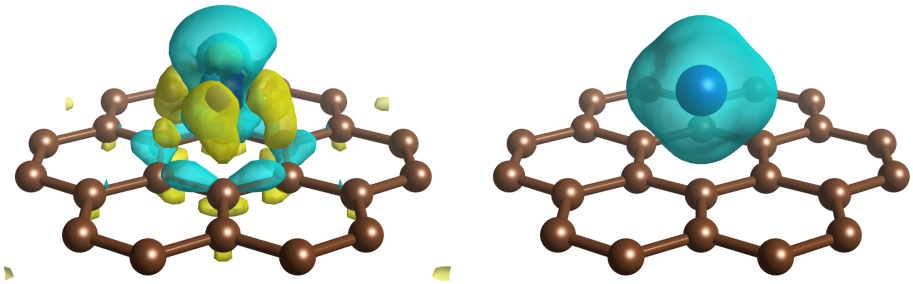

Figure 2.20: Left panel: induced charge density upon Ni adsorption. Right panel: induced spin density upon Ni adsorption. The isosurfaces correspond to $+0.02\ e/\text{Å}^3$ (yellow) and $-0.02\ e/\text{Å}^3$ (light blue).

In Fe and Co the population of the minority component on graphene is larger than the majority one, and therefore the magnetic moment of the substrate is opposed to that of the metal atom, and in absolute value much smaller than for the lighter metal atoms ($-0.27\ \mu_B$ in Fe@graphene and $-0.14\ \mu_B$ in Co@graphene).

We can rationalize the charge transfer in these systems considering separately two different phenomena. The first and the only chemically relevant one is the charge transfer which takes place in the spin component involved in the bond formation: the hybridization between partially filled orbitals of the metal atoms and the bands of graphene, that involves the majority/minority spin states of lighter/heavier TMs, is strictly related to the chemistry of these systems and is responsible for bond formation and for most of the charge transfer.

The second type of charge transfer can be caught considering the downshift of the graphene bands and the consequential filling of the π^* band. For the minority spin component of the lighter adatoms this charge is found partially on the TM atom in contradiction with a band structure view of these systems. In fact these additional occupied states are entirely built by carbon states unperturbed with respect to pristine graphene. This is likely due to the partitioning of the space in QTAIM basins, which are derived considering just the total charge density of the entire system.

2.5 Closing remarks

In this chapter we investigated the structural, magnetic and electronic properties of magnetic $3d$ transition metals adsorbed on graphene at different coverages. Furthermore we analyzed the charge transfer between the metal and the carbon atoms on a 3×3 graphene supercell. Our results show that

the structural and magnetic properties rapidly converge as the coverage decreases, and starting from $N = 9$ elementary cells they undergo minor variations. This means that the lateral adatom−adatom interactions are relevant only for high coverages, while for more diluted configurations the distance between adsorbates becomes large enough so that the main features of the system are essentially those of an isolated transition metal atom on graphene. As concerns the spectral properties, adsorption on graphene induces a rearrangement of the TM electronic states with the removal of the degeneration of the $3d$ atomic orbital and the reduction of the $4s$ one. Furthermore, only for specific coverages the formation of non negligible gaps is observed, some of which comprise the Fermi level and can influence the low excitation properties. Interestingly, Fe@graphene is the only system that presents a semiconducting behavior in both spin components. The charge transfer analysis shows that the partial filling of states belonging to the metal atoms and to graphene leads to largely varying spin populations in both the adsorbates and the substrate. It worth noting that graphene does not act just a sponge of electrons coming from the metal atom: in Sc, Ti, V, and Cr the overall magnetic moment of carbon atoms enhances that of the adsorbate, while in Fe and Co it partially counterbalances the one of the metals. Mn represents the transition between these two behaviors. The Ni@graphene system looses its magnetism due to the electron transfer from the s states to the d states of Ni resulting in a filling of the $3d$ shell.

Chapter 3

Electronic transport in TM@graphene

3.1 Introduction

The results obtained in the previous chapter show that the adsorption of $3d$ transition metals induces spin-dependent properties in pure graphene. In particular, we observed the opening of gaps with different widths and energies in the two spin components. Furthermore, the fact that some of these gaps lie around the Fermi level allows to think that the electron transport through these systems should display spin-dependent behavior. Theoretical investigations of spin-polarized currents in decorated carbon nanostructures have been tackled only in the recent years. Furst *et al.* [54] studied the transport in armchair graphene nanoribbon decorated with Fe and V. They found that the scattering of the electrons of mainly one spin component is due to the coupling of two armchair states with the TM $3d$ orbitals with matching symmetry. In the analysis of spin-polarized transport in pristine and defective graphene doped with noble and transition metals Lima *et al.* [55] showed that an essential condition to create a current polarization is the presence of spin-split localized states around the Fermi level that can hybridize with the graphene bands.

All these works are based on the analysis of the system conductance in equilibrium regime, i.e. with no voltage applied. In this chapter we present the transport properties of $3d$ transition metals adsorbed on graphene calculated in non equilibrium condition, due to an external applied bias. We consider three magnetic adsorbates, namely Ti, Fe, and Co. In fact we verified that Sc and V display overall transport behavior to Ti. The cases of Cr and Mn are of minor interest because of their very weak interaction with graphene which makes it difficult to conceive the possibility of engineering these systems. Furthermore the transport properties will be dominated by the pure graphene behavior. Ni does not induce magnetic properties in

graphene and is thus not worth studying in search of spin-dependent properties.

Except when differently specified, along this chapter we will make use of the atomic units ($e = m_e = \hbar = 1$).

3.2 Theoretical approach

In this section we describe the Non Equilibrium Green's Function (NEGF) approach, which is a powerful tool to calculate current and charge densities in nanoscale conductors under bias. We follow the derivation described in Ref. [56].

Consider the discrete Schrödinger equation:

$$H|n\rangle = E|n\rangle. \tag{3.1}$$

We divide the Hamiltonian and the wavefunction of the system into contact ($H_{1,2}$, $|\psi_{1,2}\rangle$) and device (H_d, $|\psi_d\rangle$) subspaces:

$$\begin{pmatrix} H_1 & \tau_1 & 0 \\ \tau_1^\dagger & H_d & \tau_2^\dagger \\ 0 & \tau_2 & H_2 \end{pmatrix} \begin{pmatrix} |\psi_1\rangle \\ |\psi_d\rangle \\ |\psi_2\rangle \end{pmatrix} = E \begin{pmatrix} |\psi_1\rangle \\ |\psi_d\rangle \\ |\psi_2\rangle \end{pmatrix}, \tag{3.2}$$

where $\tau_{1,2}$ describes the interaction between device and contacts. In general there are N contacts ($H_{1,\cdots,N}$) connecting ($\tau_{1,\cdots,N}$) the device H_d to the reservoirs. We made the assumption that they are independent, i.e. there are no cross terms (τ) between the different contacts.

We define the Green's function:

$$(E - H)\, G(E) = I, \tag{3.3}$$

where E is a complex energy. $G(E)$ gives the response of a system to a perturbing source $|v\rangle$ in the Schrödinger equation:

$$H|\psi\rangle = E|\psi\rangle + |v\rangle. \tag{3.4}$$

The response to this perturbation is:

$$(E - H)\,|\psi\rangle = -|v\rangle \tag{3.5}$$

$$|\psi\rangle = -G(E)|v\rangle. \tag{3.6}$$

For infinite non-periodic systems it is usually easier to calculate the Green's function than to solve the whole eigenvalue problem and most properties of the system can be calculated from the Green's function. For instance, the wavefunction of the contact ($|\psi_2\rangle$) can be obtained, provided that

we know the wavefunction of the device $|\psi_d\rangle$. From third row of eq. (3.2):

$$\begin{aligned} H_2|\psi_2\rangle + \tau_2|\psi_d\rangle &= E|\psi_2\rangle & (3.7)\\ (E - H_2)\,|\psi_2\rangle &= \tau_2|\psi_d\rangle & (3.8)\\ |\psi_2\rangle &= g_2(E)\tau_2|\psi_d\rangle, & (3.9) \end{aligned}$$

where g_2 is the surface Green's function of the isolated contact 2 ($(E - H_2)g_2 = I$).

It is important to note that, since we have an infinite system, we obtain two types of solutions for the Green's function corresponding to outgoing or incoming waves in the contacts, defined as the retarded and the advanced Green's function, respectively. If the limit $\Im m\{E\} \to 0^+$ is taken the retarded solution is found, on the contrary, $\Im m\{E\} \to 0^-$ gives the advanced.

Note that by using the retarded Green's function of the isolated contact (g_2) in eq. (3.9) we obtain the solution corresponding to an outgoing wave in the contact. The use of the advanced Green's function ($g_2^\dagger$) would give the solution corresponding to an incoming wave.

3.2.1 Self-Energy

The reason for calculating the Green's function is that it is easier than solving the Schrödinger equation. Also, the Green's function of the device (G_d) can be calculated separately without calculating the whole Green's function (G).

From the definition of the Green's function we obtain:

$$\begin{pmatrix} E - H_1 & -\tau_1 & 0 \\ -\tau_1^\dagger & E - H_d & -\tau_2^\dagger \\ 0 & -\tau_2 & E - H_2 \end{pmatrix} \begin{pmatrix} G_1 & G_{1d} & G_{12} \\ G_{d1} & G_d & G_{d2} \\ G_{21} & G_{2d} & G_2 \end{pmatrix} = \begin{pmatrix} I & 0 & 0 \\ 0 & I & 0 \\ 0 & 0 & I \end{pmatrix}. \tag{3.10}$$

Selecting the three equations in the second column:

$$\begin{aligned} (E - H_1)\,G_{1d} - \tau_1 G_d &= 0 & (3.11)\\ -\tau_1^\dagger G_{1d} + (E - H_d)\,G_d - \tau_2^\dagger G_{2d} &= I & (3.12)\\ (E - H_2)\,G_{2d} - \tau_2 G_d &= 0. & (3.13) \end{aligned}$$

We can solve eqs. (3.11) and (3.13) for G_{1d} and G_{2d}:

$$\begin{aligned} G_{1d} &= g_1\tau_1 G_d & (3.14)\\ G_{2d} &= g_2\tau_2 G_d. & (3.15) \end{aligned}$$

The substitution into eq. (3.12) gives:

$$-\tau_1^\dagger g_1\tau_1 G_d + (E - H_d)\,G_d - \tau_2^\dagger g_2\tau_2 G_d = I, \tag{3.16}$$

from which G_d is simple to find:

$$G_d = (E - H_d - \Sigma_1 - \Sigma_2)^{-1}, \tag{3.17}$$

where $\Sigma_1 = \tau_1^\dagger g_1 \tau_1$ and $\Sigma_2 = \tau_2^\dagger g_2 \tau_2$ are the so called self-energies.

The surface Green's functions g_1 and g_2 used to calculate the self-energies are usually obtained exploiting the periodicity of the contacts.

3.2.2 The spectral function

Another important use of the Green's function is the spectral function:

$$A = i\left(G - G^\dagger\right), \tag{3.18}$$

which gives the density of states (DOS) and *all* the solutions to the Schrödinger equation. In order to observe it it is necessary to expand the Green's function on the eigenbasis in order to observe it:

$$G = \frac{1}{E + i\delta - H} = \sum_k \frac{|k\rangle\langle k|}{E + i\delta - \varepsilon_k}, \tag{3.19}$$

where δ is the small imaginary part of E, $|k\rangle$ represent all the eigenvectors of H with the corresponding eigenvalues ε_k. Expanding the spectral function on the basis we obtain:

$$\begin{aligned} A &= i\left(\frac{1}{E + i\delta - H} - \frac{1}{E - i\delta - H}\right) && (3.20)\\ &= i\sum_k |k\rangle\langle k| \left(\frac{1}{E + i\delta - \varepsilon_k} - \frac{1}{E - i\delta - \varepsilon_k}\right) && (3.21)\\ &= \sum_k |k\rangle\langle k| \frac{2\delta}{(E - \varepsilon_k)^2 + \delta^2}. && (3.22) \end{aligned}$$

Letting δ go to zero gives:

$$A = 2\pi \sum_k \delta(E - \varepsilon_k)\,|k\rangle\langle k|, \tag{3.23}$$

which is zero everywhere except for $E = \varepsilon_k$. Eq. (3.23) shows, therefore, that the spectral function gives us all solutions to the Schrödinger equation.

3.2.3 Response to an incoming wave

In the non equilibrium case, reservoirs with different chemical potentials will inject electrons and occupy the states corresponding to incoming waves in

the contacts. Therefore, we have to find the solutions corresponding to these incoming waves.

Consider contact 1: at a certain energy we have solutions corresponding to an incoming wave that is totally reflected at the end of the contact. We will denote these solutions with $|\psi_{1,n}\rangle$ where 1 is the contact number and n is a quantum number. We can find all these solutions from the spectral function a_1 of the isolated contact. Once we connect the contacts to the device, we can calculate the wavefunction in the whole system generated by the incoming wave in contact 1. We suppose that a wavefunction should be of the form $|\psi_{1,n}\rangle+|\psi^R\rangle$ where $|\psi_{1,n}\rangle$ is the totally reflected wave and $|\psi^R\rangle$ is the retarded response of the whole system. Putting the ansatz $|\psi_{1,n}\rangle+|\psi^R\rangle$ into the Schrödinger equation gives:

$$\begin{aligned}
\begin{pmatrix} H_1+\tau_1+ \\ H_d+\tau_1^\dagger+\tau_2^\dagger+ \\ H_2+\tau_2 \end{pmatrix}\left(|\psi_{1,n}\rangle+|\psi^R\rangle\right) &= E\left(|\psi_{1,n}\rangle+|\psi^R\rangle\right) \\
\begin{pmatrix} E|\psi_{1,n}\rangle+ \\ \tau_1^\dagger|\psi_{1,n}\rangle+ \\ 0 \end{pmatrix}+\begin{pmatrix} H_1+\tau_1+ \\ H_d+\tau_1^\dagger+\tau_2^\dagger+ \\ H_2+\tau_2 \end{pmatrix}|\psi^R\rangle &= E\left(|\psi_{1,n}\rangle+|\psi^R\rangle\right) \\
H|\psi^R\rangle &= E|\psi^R\rangle-\tau_1^\dagger|\psi_{1,n}\rangle
\end{aligned} \tag{3.24}$$

and we see that $|\psi^R\rangle$ is nothing else but the response of the whole system to the perturbation $-\tau_1^\dagger|\psi_{1,n}\rangle$. We thus obtain:

$$|\psi^R\rangle = G\tau_1^\dagger|\psi_{1,n}\rangle. \tag{3.25}$$

It is important to observe that the scattering states, generated from eq. (3.25) using all possible incoming waves from each contact, form a complete set of solutions to the full Schrödinger equation.

The device wavefunction $|\psi_d\rangle$ is given by:

$$|\psi_d\rangle = G_d\tau_1^\dagger|\psi_{1,n}\rangle \tag{3.26}$$

and from eq. (3.9) we obtain:

$$|\psi_2\rangle = g_2\tau_2|\psi_d\rangle = g_2\tau_2 G_d\tau_1^\dagger|\psi_{1,n}\rangle. \tag{3.27}$$

3.2.4 Charge density matrix

In the non equilibrium case we are often interested in two quantities: the current and the charge density matrix. Here we consider the charge density:

$$\rho = \sum_k f(k,\mu)|\psi_k\rangle\langle\psi_k|, \tag{3.28}$$

where the sum runs over all states with the occupation number $f(E_k, \mu)$. The occupation number is determined by the reservoirs filling the incoming waves in the contacts such that:

$$f(E_k, \mu_1) = \frac{1}{1 + e^{(E_k - \mu_1)/k_B T}} \tag{3.29}$$

is the Fermi-Dirac function with the chemical potential μ_1 and temperature T of the reservoir responsible for injecting the electrons into the contacts.

The wavefunction of the device, given by an incoming wave in contact 1 (see eq. (3.26)), is:

$$|\psi_{d,k}\rangle = G_d \tau_1^\dagger |\psi_{1,k}\rangle. \tag{3.30}$$

Adding up all states from contact 1 gives:

$$\begin{aligned}
\rho_{d,1} &= \int_{E=-\infty}^{\infty} \mathrm{d}E \sum_k f(E, \mu_1) \delta(E - E_k) |\psi_{d,k}\rangle\langle\psi_{d,k}| \\
&= \int_{E=-\infty}^{\infty} \mathrm{d}E \, f(E, \mu_1) \sum_k \delta(E - E_k) G_d \tau_1^\dagger |\psi_{1,k}\rangle\langle\psi_{1,k}| \tau_1 G_d^\dagger \\
&= \int_{E=-\infty}^{\infty} \mathrm{d}E \, f(E, \mu_1) G_d \tau_1^\dagger \left(\sum_k \delta(E - E_k) |\psi_{1,k}\rangle\langle\psi_{1,k}| \right) \tau_1 G_d^\dagger \\
&= \text{[eq. (3.23)]} = \int_{E=-\infty}^{\infty} \mathrm{d}E \, f(E, \mu_1) G_d \tau_1^\dagger \frac{a_1}{2\pi} \tau_1 G_d^\dagger.
\end{aligned} \tag{3.31}$$

If we introduce the quantity $\Gamma_1 = \tau_1^\dagger a_1 \tau_1 = i\left(\Sigma_1 - \Sigma_1^\dagger\right)$ we obtain the simple formula:

$$\rho[\text{from contact 1}] = \frac{1}{2\pi} \int_{E=-\infty}^{\infty} \mathrm{d}E \, f(E, \mu_1) G_d \Gamma_1 G_d^\dagger. \tag{3.32}$$

The total charge density, thus, becomes a sum over all contacts:

$$\rho = \frac{2 \text{ (for spin)}}{2\pi} \int_{E=-\infty}^{\infty} \mathrm{d}E \sum_i f(E, \mu_i) G_d \Gamma_i G_d^\dagger. \tag{3.33}$$

In the case of equilibrium conditions, i.e. with no applied bias, this formula takes the form of the standard expression.

3.3 Structure and methods

The system in which we are interested is represented by nanojunction constituted by two metal graphene electrodes and a scattering region with finite extension along the transport direction z, able to differently filter the two spin components. The results obtained in the previous chapter suggest to consider the presence of TM atoms as source of spin dependent scattering. Transition metals are adsorbed at the center region of the junction extending for about 18 Å along z in a periodic array so as to locally reproduce the coverage of a 3×3 supercell (see Fig. 3.1).

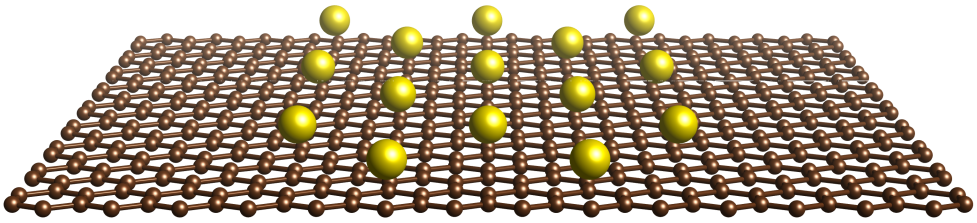

Figure 3.1: Scattering region connected with pure graphene electrodes.

The model graphene nanojunction in the yz plane is made of 168 carbon atoms and 5 TM adatoms. Following the prescription described in the previous section we divide the system in three parts: the scattering region (S), composed of 120 carbon atom and 5 TM adatoms, and the left (L) and right (R) electrodes, composed of 24 carbon atoms each. The region S consists of a central part containing 96 C atoms where the transition metals are adsorbed. The active central portion of S is separated from the electrodes by means of two contact regions that have to be sufficiently large in order to ensure a complete decay of the perturbations induced by the metal adatoms. The structure is periodically repeated along the y direction and a fictitious periodicity along x is also imposed giving facing nanojunctions separated by 24.74 Å of vacuum, to avoid any sheet-sheet interaction.

We perform geometrical optimization with the SIESTA code using the same set of computational parameters employed for the analysis of the periodic structures. We relax all the atoms except those belonging to the electrodes plus an additional row of carbon atoms contiguous to them. The residual forces are below the tolerance required in the periodic calculations except those on the border atoms connecting relaxed and unrelaxed regions. The structural and magnetic properties (height, bond length, binding energy and magnetic moment) are robust with respect to the change from periodic to open system, i.e. with respect to the addition of two semi-infinite regions of pristine graphene to the central active structure.

The electron transport is studied with the TranSIESTA code [57], which

is based on DFT as implemented in SIESTA and that takes into account the effect of the finite bias using the non equilibrium Green's function approach. For transport calculation an optimized single-ζ basis set is employed for carbon atom. This choice proved to be extremely efficient with no loss of accuracy. In fact the graphene band structure around the Fermi level is well described also by this basis set.

3.4 Electrodes

Charge transport is a matter of electron states propagating from one contact to the other through the scattering region. In this sense, the knowledge of the electronic properties of the leads represents a starting point for the comprehension of the charge flow through the device.

Following the geometry of the structure, we consider as elementary cell a rectangular cell containing four carbon atoms (see left panel of Fig. 3.2). The cell vectors are:

$$\mathbf{a}_1 = a(1,0), \qquad \mathbf{a}_2 = a(0,\sqrt{3}), \tag{3.34}$$

where a is the lattice constant. Also the Brillouin zone (see right panel of Fig. 3.2) is a rectangle with reciprocal basis vectors:

$$\mathbf{b}_1 = \frac{\pi}{a}(2,0), \qquad \mathbf{b}_2 = \frac{\pi}{a}\left(0,\frac{2}{\sqrt{3}}\right). \tag{3.35}$$

In view of the loss of periodicity along the z direction upon the contacting

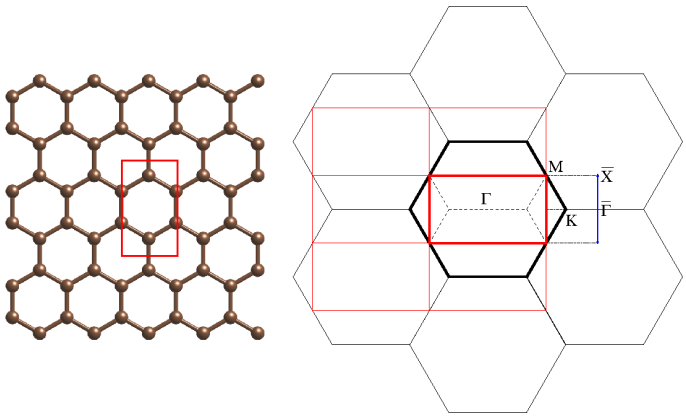

Figure 3.2: Left: Rectangular cell containing four carbon atoms. Right: Brillouin zone of the primitive graphene cell (thick black line) and of the rectangular cell (thick red line). The vertical blue line represents the 1D BZ.

with the scattering region, the 2D Brillouin zone is projected along the transport direction. The evaluation of some quantities will be performed integrating in the new 1D BZ (blue line in Fig. 3.2). Being the electrode composed of three unit cells along the transverse (y) direction, its band structure can be easily obtained from the 1D projected band structure of the unit cell with an appropriate folding (see Fig. 3.3). The main electronic feature, i.e. the presence of a gap but at the $\overline{\Gamma}$-point, is still present. The

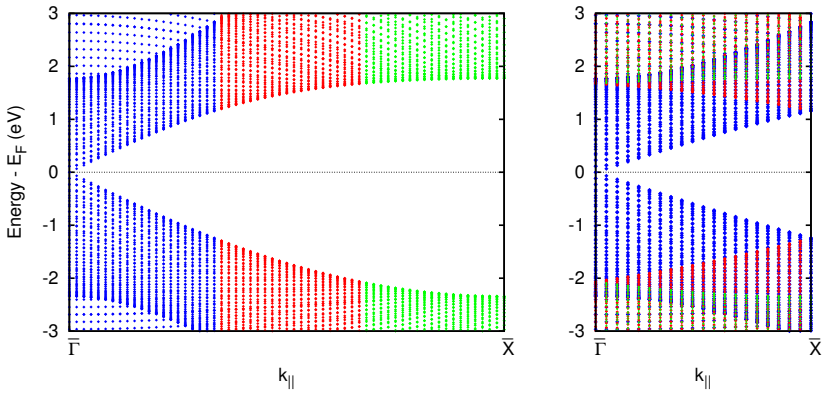

Figure 3.3: Left panel: projected band structure of the elementary graphene rectangular unit cell. Right panel: projected band structure of the electrode obtained with a folding from the rectangular one.

absence of available electronic states in the electrode means that for those specific energies and momenta no propagation through the central region can take place.

3.5 Scattering region

The transport properties have been investigated for three different scattering regions depending on the transition metal adsorbed, all contacted with the pristine graphene electrode described above. As a representative case, in the following we present the results obtained in the case of Fe adatoms.

3.5.1 Periodic structure

A first insight of the electronic properties can be obtained considering only the central region, i.e. neglecting the electrodes, and treating it as a periodic structure. In fact in the scattering region the atoms are adsorbed in a regular array suitable for periodic calculations.

With this approximation we obtain the spin resolved DOS and band structure of the Fe adsorbed on the 3×3 supercell, reported in Fig. 3.4,

along with data of pristine graphene.

For a better readability of the band structures we emphasize the Fe-character of the bands using a weighted red line. In the case of the spin majority component (up), the bands in the region around the Fermi level assume the typical features of the pristine substrate, but for a small down-shift of the Dirac point. The five Fe $3d$ bands lie well below the Fermi level, while the $4s$ one is now empty lying at about 0.5 eV above E_{F}. Focusing on Γ, the five-fold degenerate atomic d orbital splits in three states. The two-fold more bounded one has the e_2 symmetry ($d_{x^2-y^2}$, d_{xy}), while the a_1 state (d_{z^2}) and the two fold e_1 states (d_{xz}, d_{yz}) are nearly degenerate, in agreement with literature results [46]. The $4s$ and d_{z^2} states maintain a strong localized atomic character and do not mix with the graphene bands. The remaining d bands significantly hybridize with graphene. As concerns the transport properties, the important feature is the opening of a band gap of about 0.28 eV in the Dirac cone, which is now located at Γ. In fact, in these superlattices the folding of the Brillouin zone brings K and K$'$ in Γ and the perturbation due to the adsorbate allows the hybridization of the graphene states. The presence of this gap, which comprises the Fermi level, gives a semiconductor character to this spin population.

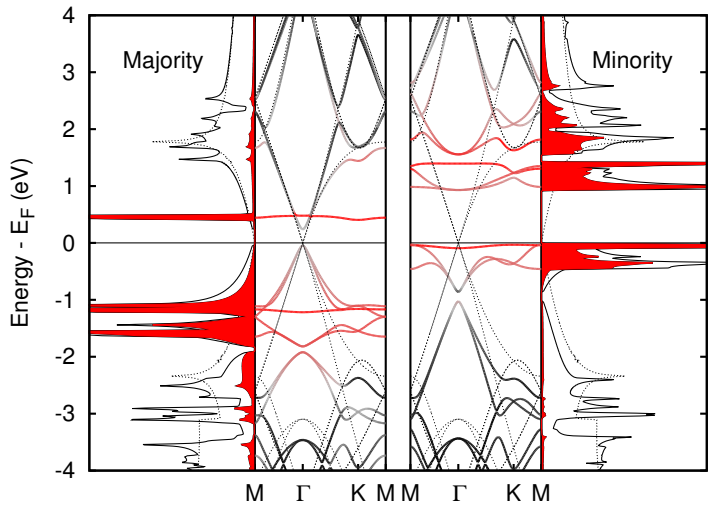

Figure 3.4: Spin-resolved DOS and band structure of the periodic structure with the same coverage of the scattering region. In red are reported the Fe features.

In the case of minority spin component (down), the metal atom exhibits three occupied d states just below the Fermi level: the a_1 state shows an atomic-like character, while the e_2 ones strongly hybridize with carbon. The states with e_1 symmetry are empty and lie about 1 eV above E_{F}, close to

the 4*s* level. Both spin-up and spin-down 4*s* orbitals of the adatom are now unoccupied and the electrons are transferred to the minority spin *d* orbitals. Analogously to the majority component, a gap opening (0.17 eV) in the graphene bands takes place also in the minority spin component, but it is located below the Fermi level because of the downshift of the Dirac cone. A striking feature of the minority component is the opening of an additional wide gap of 0.95 eV between the e_2 and e_1 bands, which includes E_F. Interestingly, there are no graphene states in this region, and the highest occupied and the lowest unoccupied states are localized and entirely due to the metal atom. This scenario implies that Fe@graphene in 3×3 arrangements is strongly spin-asymmetric: the majority spin electrons behave as in a small-gap semiconductor, while the minority ones show a clear insulating character.

3.5.2 Adatom-adatom interaction

Among the different coverages we choose the 3×3 structure essentially because of two reasons: a) this cell is the smallest one showing a negligible direct adatom-adatom interaction (see Chap. 2), b) its arrangement on graphene geometry is compatible with the scattering geometry. It is indeed known that the Fe atoms tend to aggregate in some conditions [58], forming islands. In order to verify the possibility of obtaining metastable regular arrays of Fe adatoms we consider the lateral interaction between two iron atoms adsorbed at different distances and in the ferromagnetic configuration. The lateral interaction can be defined as the difference between the adsorption energy of a Fe dimer and those of two isolated Fe adatoms (i.e. $2E_B = 1.80$ eV). Using a very large unit cell, i.e. the 7×7 one, we find that the most favorable arrangement corresponds to iron atoms sitting in first neighboring sites. However, as can be seen in Fig. 3.5, the energy of the system does not decrease monotonically as the Fe−Fe distance decreases. Actually there exists a metastable regime with a minimum at $d_{\mathrm{Fe-Fe}} = 7.42$ Å, which corresponds to the adsorbate−adsorbate distance in the 3×3 supercell. Henceforth, based on our computations we can affirm that Fe@graphene structures at low coverages might be feasible. This can be also rationalized considering the repulsive barrier at short distances amounting to 50 meV, due to dipole-dipole interaction between adsorbates [59], which could prevent the cluster formation starting from a diluted overlayer. In addition to this overall energy barrier, one has also to consider the diffusion barrier between hollow positions which amount to 0.59 eV (see Ref. [32]).

A further interaction which decays more slowly is the Lau-Kohn one [60] due to substrate-mediated interaction between adsorbates. This contribution decays as the inverse of the square of the distance thanks to the low dimensionality of the substrate (2D) and hence is still active at larger distances. The intriguing aspect is its sinusoidal dependence with *d* and the

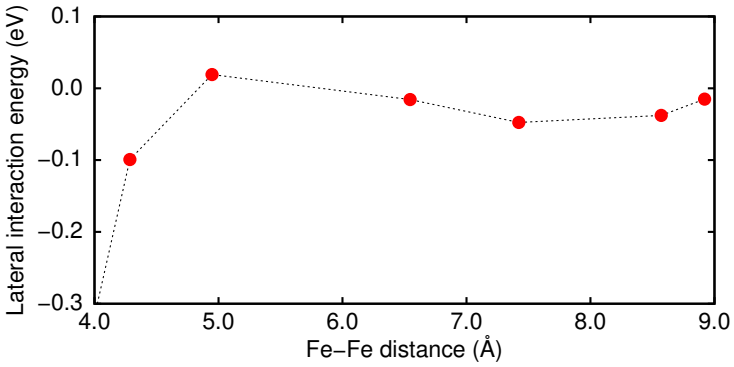

Figure 3.5: Lateral interaction energy as a function of Fe−Fe distance.

consequent stabilization of some superstructures with respect to others. In particular, its oscillation has a periodicity equal to two times the Fermi vector k_{F}:

$$E_{\mathrm{LK}} \propto \frac{\sin(2k_{\mathrm{F}}d + \delta)}{d^2}. \tag{3.36}$$

In pristine graphene this value corresponds to $\lambda = 2a/3$, where a is the lattice constant. In the hypothesis of small perturbations this means that the 3×3 supercell is the smallest one in which all the adsorbates are in phase. Considering the phase shift δ commonly used in literature, i.e. $-\pi/2$ [61], the 3×3 arrangement results the most favored. Looking at the Fig. 3.5 we can note that for larger Fe−Fe distances the binding energy starts to decrease.

Another type of interaction, involving the magnetic coupling of adsorbates and less energetic that the Lau-Kohn one, is the RKKY type [62, 63, 64]. This interaction is purely magnetic and its spatial dependence in 2D systems is the same as in the Lau-Kohn one. This contribution can stabilize some magnetic configurations with respect to others. We numerically verified the effects of different magnetic arrangements. First of all we studied the stability of the ferromagnetic coupling between two Fe atoms with respect to the antiferromagnetic configuration placing two Fe adatoms in a large 7×7 supercell. For all considered distances the ferromagnetic configuration is always more stable for not less than 40 meV. Furthermore, we considered a 6×6 supercell with four Fe adsorbates in a non-ferromagnetic configuration (there exist only one possible arrangement). Also in this case the ferromagnetic configuration results preferred for about 80 meV per atom.

3.5.3 Extended system

For the extended system no band structure can be calculated and the analysis of the spectral properties is based on the densities of states (possibly the $k_{\parallel}$-resolved DOS).

In Fig. 3.6 are reported the DOS of the contact region together with the projection on the Fe atoms. The five $3d$ majority states lie well below the Fermi level while the $4s$ orbital is unoccupied. In the minority component a non-negligible gap comprising E_{F} separates the e_2 and e_1 occupied states from the a_1 and $4s$ orbitals.

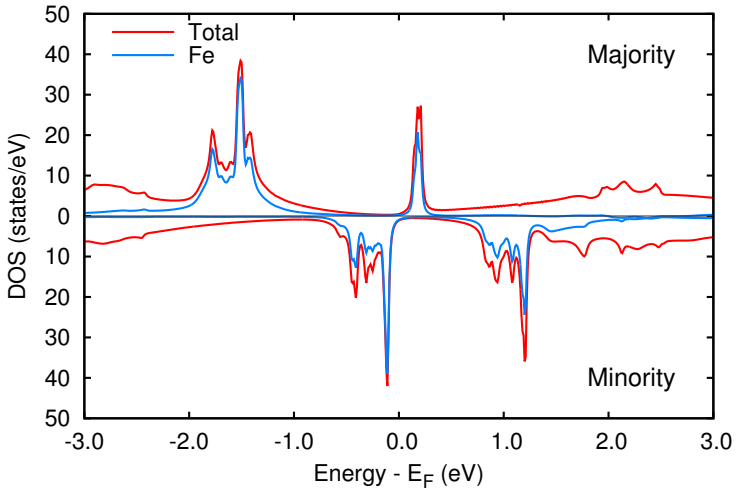

Figure 3.6: Spin-resolved density of states of the central region. The projected DOS on the Fe atoms is reported in blue.

To analyze the contribution of the different Fe atoms we focus our attention on the $4s$ majority orbital which is the only one showing an atomic-like character. We calculate the density of states at the $\overline{\Gamma}$-point in a small energy range around the Fermi level reducing the imaginary part of the energy, i.e. increasing the resolution of the calculation (see Fig. 3.7). As expected, the peaks corresponding to the occupied minority states show contributions from all the iron atoms, while the four $4s$ majority peaks can be unambiguously attributed to different atoms. The two "external" atoms (1 and 5) are degenerate and give rise to a peak of double intensity with respect to the others. At lower energy there are two peaks due to the two "internal" atoms (2 and 4) which are near enough to interact and split. The last peak corresponds to the "central" atom (3). Fitting the peaks with a lorentzian function we obtain a width equal to the imaginary part of the energy. This means that all these states are sharp and do not hybridize with the substrate.

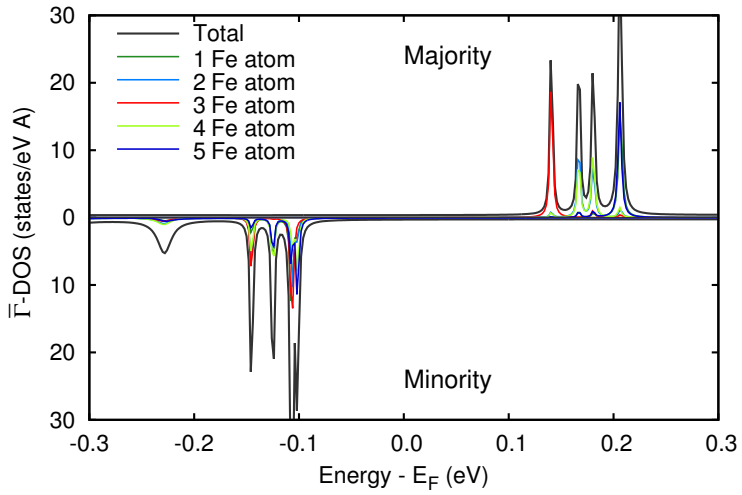

Figure 3.7: Spin-resolved density of states at the $\overline{\Gamma}$-point for the different Fe atoms. The numbers are attributed starting from the atom nearest to the left electrode and proceeding along the transport direction.

To appreciate the dispersion of the other states we analyze the k-resolved density of states shown in Fig. 3.8. Comparing the DOS with that of the pristine system (shown in the middle panel) one can easily identify the effects induced by the adatoms. In the majority component the $3d$ filled states hybridize with the substrate displaying a little dispersion while the $4s$ state located in the graphene gap exhibit an atomic character. Above E_{F}, just below a graphene band edge, an interface state is well recognizable. As concerns the minority component, the features below E_{F} typical of graphene are almost completely quenched, the states pertaining to the adatom show a negligible dispersion and the unoccupied graphene band edge state is no more easily detectable.

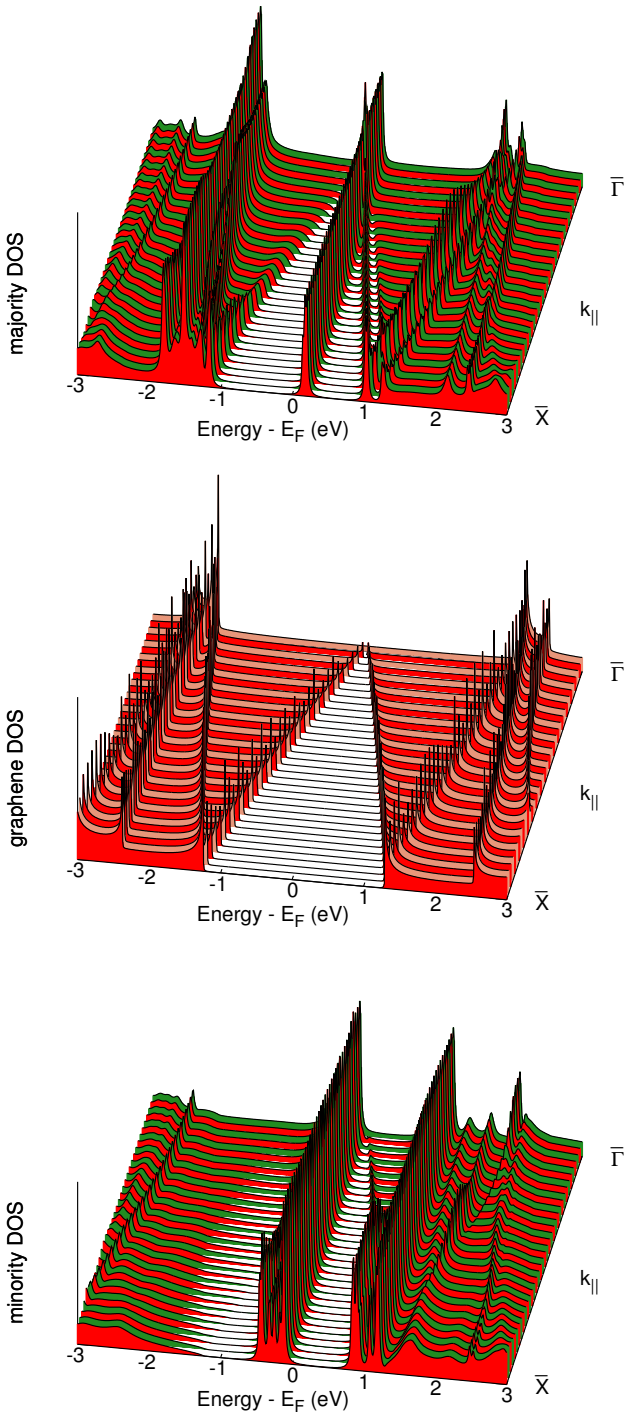

Figure 3.8: k-resolved density of states of the extended region. For comparison in the middle panel the k-resolved DOS of the unperturbed system is shown.

3.6 Transmission

The investigation of the electron transport in molecular junctions necessitate an approach different from that suitable for macroscopic devices. The reduced dimensions require in fact an atomic-level description, where quantum mechanical effects are adequately taken into account. A widely accepted atomic approach is due to Landauer [65] whose main principle is the assumption that the system under analysis is coupled to large reservoirs where all inelastic processes take place. As long as only elastic carriers collisions are considered the electron transport can be treated as a scattering problem. The basic idea is to relate key transport quantities such as the electrical conductance with the transmission and reflection probabilities for carriers to cross the system. This approach relies on specific physical assumptions that may or may not be satisfied in experimental realizations of transport in nanoscale systems.

1. *Open quantum system.* The nanojunction is assumed to be connected to the leads which in turn are coupled adiabatically to semi-infinite reservoirs. Adiabatic coupling means that any state that travels from the reservoirs enters into the leads without any reflection. Since the reservoirs may represent a battery, the energy required to extract an electron from one reservoir and bring it into the system can be different from the energy required to bring it into the second reservoir. The electrochemical potentials associated to the two reservoirs differ by the bias: $V = \mu_L - \mu_R$. As a consequence, the transport through the systems can be formulated as a quantum mechanical scattering problem. Hence one can reduce the non equilibrium transport problem to a quantum mechanical one.

2. *Ideal steady state.* It is possible to wait long enough so that the system reach a steady state, that is its density operator does not depend on time.

3. *Openness vs. boundary conditions.* Since we are in a steady state, the role of the reservoirs is just to continuously supply electrons to be injected into the junction. Thus the open system can be mapped to a finite one with suitable boundary conditions. Electrons are prepared in the distant past and far away from the junction into wave-packets. These wave-packets move towards the junction from the leads, scatter on the junction potential, and move away propagating in the opposite lead.

4. *Mean-field approximation.* Let us assume that the Hamiltonian of the scattering region $\hat{H}_S$ can be separated into at least two components:

$$\hat{H}_S = \hat{H}_{mf} + \hat{V},$$

where $\hat{H}_{mf}$ is the Hamiltonian describing independent electrons in the presence of the ions. $\hat{V}$ is the localized perturbing potential due to the presence of scattering centers - beyond mean-field - in the nanojunction. To practical purpose, we adopt mean-field approximation and we consider a DFT

Hamiltonian $\hat{H}_S$ to describe the full lead-nanojunction-lead system.

5. *Independent channels.* After the previous assumptions, we are left with a static and deterministic single-particle problem, that is easier to solve than the true non equilibrium statistical one. We assume that the initial electronic state can be expanded into different channels, that are a set of quantum numbers describing the scattering solution. We also assume that electrons are injected from the left (right) reservoir (i.e. right (left) moving electrons) with a local distribution function appropriate to the corresponding chemical potential:

$$f_{L(R)}(E) = \frac{1}{1 + e^{(E-\mu_{L(R)})/k_B T}},$$

where T is the temperature.

With these hypotheses, the basic idea of the scattering approach is to relate the transport properties such as conductances with the transmission and reflection probabilities for carriers incident on the sample. Phase-coherence is assumed to be preserved on the entire sample and inelastic scattering is restricted to the electron reservoirs only. Instead of dealing with complex processes taking place inside the reservoirs they enter into the description as a set of boundary conditions. In this approach, even the bias represented by the chemical potential difference is not used as a perturbation to some Hamiltonian. Instead, it represents an additional boundary condition on the system, where wave-packets with given momenta carry the current across the nanojunction. Due to the scattering of those wave-packets with the potential $\hat{V}$ of the junction, each electron has a finite probability to be transmitted in any given direction, and consequently a probability to be reflected.

3.6.1 Landauer theory

In the Landauer approach a central device is connected with semi-infinite leads that feed it with electrons from an electron reservoir (see Fig. 3.9). The Landauer formula gives a relationship between the currents flowing through the leads and the chemical potentials of the reservoirs:

$$I_i = \frac{e}{h} \sum_j \int \mathrm{d}E \; T_{ij}(E) \left[f_i(E) - f_j(E) \right]$$

where i, j label the different leads, $f_i(E)$ is the Fermi-Dirac distribution for reservoir i (assumed to be in thermal equilibrium), and T_{ij} are the transmission coefficients for electrons to go from lead i to lead j.

For small biases between the reservoirs, this relationship can be linearized

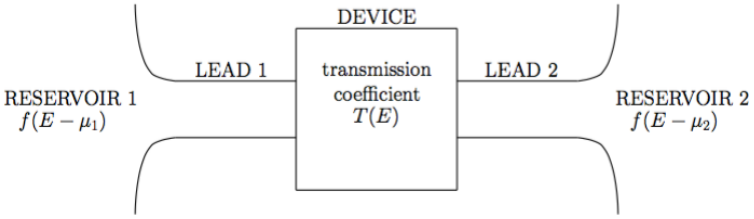

Figure 3.9: Schematic representation of a nanojunction where a device is connected with two leads.

to obtain (we will also assume temperature $T = 0$ from now on):

$$I_i = \sum_j T_{ij}(E_\mathrm{F})(\mu_i - \mu_j)$$

where $\mu_{i,j}$ are the chemical potentials of reservoir i, j and E_F is the Fermi energy of the system. As such, the current-voltage characteristics of the device can be fully determined by calculating the transmission coefficients T_{ij} between all leads. These transmission coefficients can be written as sums of transmission probabilities:

$$T_{ij} = \sum_{m,n} \left| t^{ij}_{mn} \right|^2$$

where t^{ij}_{mn} is the electron flux amplitude for an electron leaving the device through channel m in lead i when the incoming flux amplitude in channel n in lead j is set to 1. In order to define such incoming and outgoing wave amplitudes, one needs the leads to be translationally invariant in the longitudinal direction.

3.6.2 Single barrier

The simplest example of a nanoscale junction is represented by a molecule coupled with two leads. This is a 3-dimensional system, but the underlying physics can be understood also considering the one-dimensional case, as long as the effects of the two semi-infinite leads and of the junction are correctly simulated. A general one-dimensional problem is depicted in the left panel of Fig. 3.10. In the left (L) and right (R) regions the potential is a constant while in the middle region the potential $V(x)$ can have any shape. An incoming wave $Ae^{ik_L x}$ is partially reflected with a probability amplitude B and partially transmitted with a probability $T = |F|^2$.

As an example, we calculate the transmission probability in the case of

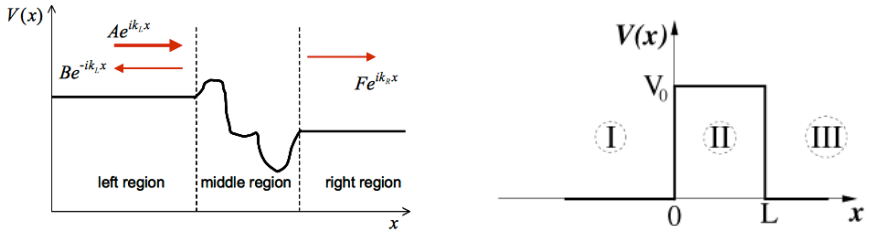

Figure 3.10: Left: a general one-dimensional scattering problem where the incoming wave is partially reflected and partially transmitted. Right: single potential barrier of height V_0 and length L. Outside the barrier the potential is set to zero.

a single potential barrier. Here the barrier simulates the central part of the junction where the electrons are elastically scattered. The analysis of this simplified model allows to grasp the main features of electronic transport across interfaces.

Our aim is to calculate the probability to cross the potential barrier as a function of the energy E of the incoming electron. We calculate the solutions of the Schrödinger equations in the three different regions (see Fig. 3.10, right panel). We then match the wavefunctions and their first spatial derivatives at the boundaries $x = 0$ and $x = L$. With the hypothesis $E < V_0$ we obtain (up to a multiplicative constant):

$$\psi_I = e^{ik_1 x} + re^{-ik_1 x}, \quad \psi_{II} = a_2 e^{k_2 x} + b_2 e^{-k_2 x}, \quad \psi_{III} = te^{ik_1 x},$$

where:

$$k_1 = \sqrt{E} \quad \text{and} \quad k_2 = \sqrt{V_0 - E}.$$

Note that ψ_{III} has only one component because we are considering an electron impinging in the barrier from the left.

Imposing the boundary conditions we get the following relationships:

$$\begin{aligned} &1 + r = a_2 + b_2 \\ &ik_1 - ik_1 r = k_2 a_2 - k_2 b_2 \\ &a_2 e^{k_2 L} + b_2 e^{-k_2 L} = te^{ik_1 L} \\ &k_2 a_2 e^{k_2 L} - k_2 b_2 e^{-k_2 L} = ik_1 te^{ik_1 L}. \end{aligned}$$

Solving these equations we obtain the expression of the transmission probability:

$$T = |t|^2 = \frac{4E(V_0 - E)}{4E(V_0 - E) + V_0^2 \sinh^2(k_2 L)}.$$

For more realistic systems other calculations can be performed. The main transmission formula can be derived either using the Green's function [66]

or with the Fisher-Lee relation [67]. In the first case the transmission is given by:

$$T(E) = \mathrm{Tr}\left(\Gamma_L G^R \Gamma_R G^A\right), \tag{3.37}$$

where $G^{R/A}$ are the retarded/advanced Green's functions of the central region while $\Gamma_{L/R}$ represent the coupling between the leads (given by the leads self-energies).

The electronic current in SI units is then:

$$I = \frac{2e}{h} \int_{E=-\infty}^{\infty} \mathrm{d}E \left(f(E,\mu_L) - f(E,\mu_R)\right) T(E) \tag{3.38}$$

where the factor 2 comes from spin degeneracy and $\mu_{L/R}$ are the chemical potentials of the two electrodes.

3.7 Equilibrium regime

When the two electrochemical potentials μ_L and μ_R of the electrodes are equal no bias is applied and consequently no current can flow through the device. Nevertheless, the analysis of the equilibrium regime can highlight some interesting features useful for the comprehension of the non equilibrium case.

3.7.1 Transmission function

The electronic transmission and the current across a nanojunction depend on the amount of incoming states from the lead that are allowed or prevented for propagation in the scattering region. This can be essentially related to the presence/absence in the SR of delocalized states with the appropriate symmetry able to form a constructive combination with states of the leads. Differently, localized states or orbitals that give rise to destructive quantum interference would produce fading transmission and Fano antiresonances [68, 69].

In Sect. 3.6 we saw that the transmission function can be obtained as the sum of the eigenvalues of the scattering matrix. We calculate the transmission coefficients T_{ij}, where ij label the eigenstates in the leads, and we observe that the transmission function is given by the sum of only the first two values, the other channels giving essentially no contribution. In fact there exist only two states in the lead for the considered energies. The result obtained at the $\overline{\Gamma}$-point is reported in Fig. 3.11. In the same plot a red line represents the density of states of the Fe atoms. Reminding that a perfect transmission implies a transmission coefficient equal to 1, we observe substantial deviations in correspondence of the adatoms states. At -1.5 eV the hybridized $3d$ states strongly perturb the transmission of the majority

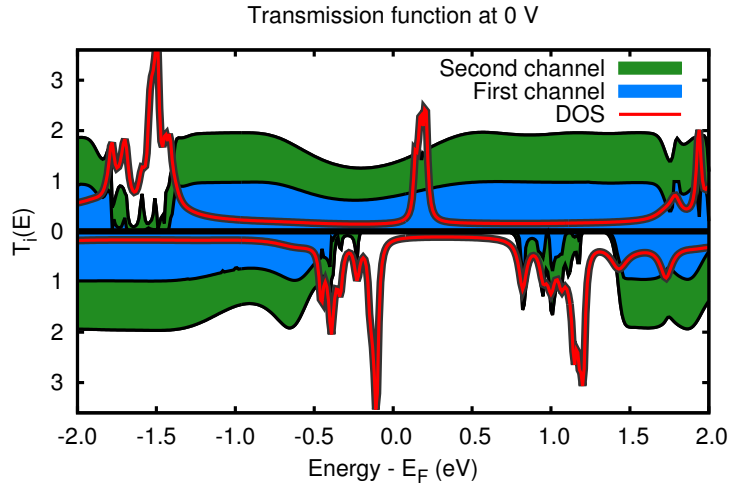

Figure 3.11: Transmission coefficients calculated at the $\overline{\Gamma}$-point. The red line represents the density of states of the Fe atoms.

component. The localized $4s$ state at 0.2 eV has instead a minor effect giving rise only to a small dip in the $T(E)$. Hybridized states also perturb the transmission of the minority component just below E_{F} and at ~ 1.0 eV. Since these states belong to a large energy gap ranging from ~ -0.1 eV to $\sim 1.5\ eV$ their effect is expected to be negligible. For this spin component the transmission is likely to be dominated by the absence of available states in a significant energy range around the Fermi level.

In Fig. 3.12 are shown the k-resolved $T(E)$ for the two spin components together with that of the graphene electrodes. In the case of pristine graphene (central panel) the absence of scattering centers yields a transmission function equal to the number of transmitting channels or to 0, depending on the existence/inexistence of electronic states at a given energy available for the transport. As a consequence, the plot of the transmission function strongly reminds that of the density of states (see the central panel of Fig. 4.6). In the scattering region the propagation is governed by the same mechanisms, in the sense that the transmission can occur only for electronic available states in the leads. This means that the propagation of electronic states falling in the electrode's gap is prevented. This is clearly visible looking at the upper panel, where the majority $T(E)$ is depicted. Besides this general feature, the transmission functions of both spin components display the same deviations with respect to the unperturbed case pointed out in the analysis of the transmission coefficients at $\overline{\Gamma}$ (see Fig. 3.11). In the k-resolved plot the large gap in the minority transmission function is even more evident.

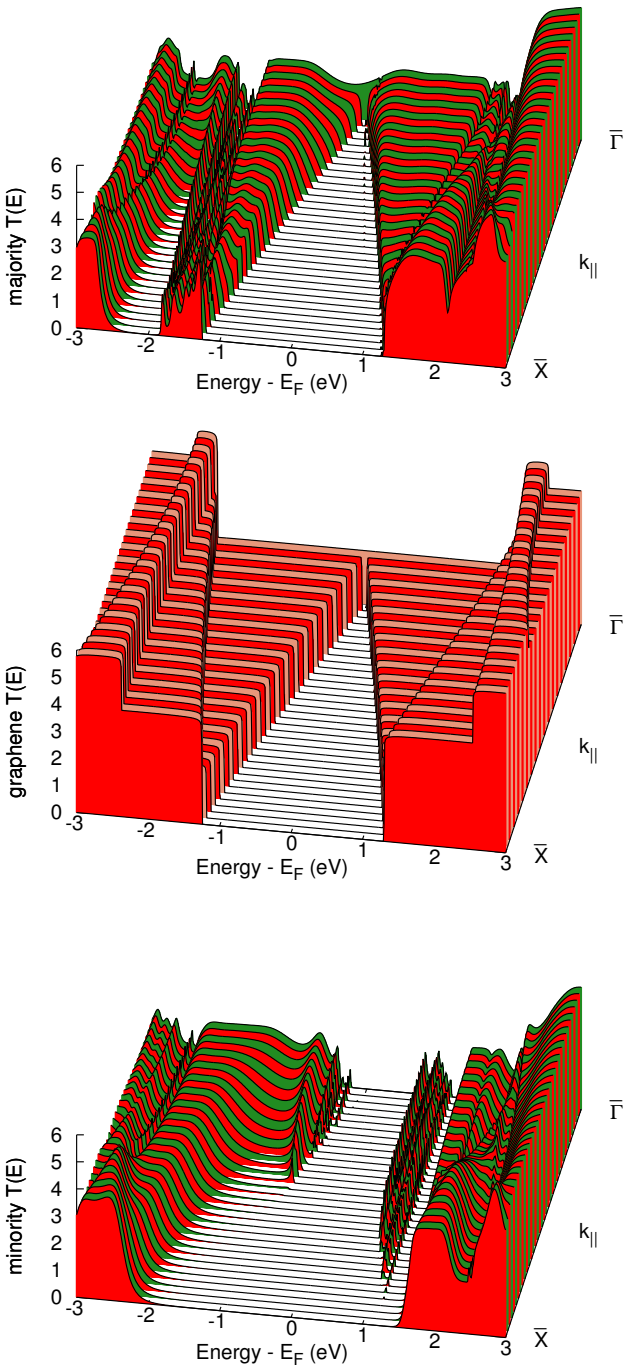

Figure 3.12: k-resolved transmission function. For comparison in the middle panel the k-resolved $T(E)$ of the unperturbed system is shown.

The integration over the k-points yields the transmission function depicted in Fig. 3.13. In the same plot is also reported the integrated $T(E)$ function of the pristine graphene. As concerns the majority component, in a wide energy range around the Fermi level the two curves do not differ significantly. The strong decrease around -1.5 eV is due to the hybridization of the $3d$ states with the substrate, already pointed out. In the minority component, beside the wide gap comprising E_{F}, we observe that the $T(E)$ differs, in some cases being significantly smaller, from the transmission function of pure graphene.

This analysis, despite being performed only for the equilibrium regime, reveals substantial differences between the two spin components that can possibly lead to polarized currents.

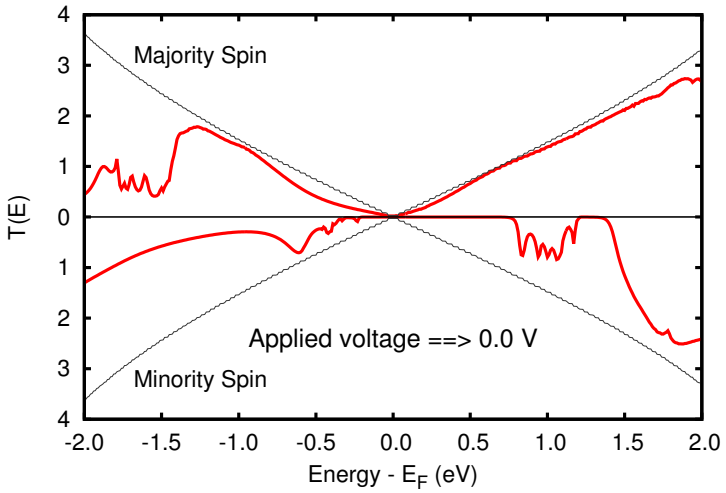

Figure 3.13: Integrated transmission function. For comparison also the transmission function of the electrodes is shown.

3.8 Non equilibrium regime

In macroscopic devices the electron transport is ruled by the Ohm's law, which states that the current in a material is proportional to the applied voltage. The constant of proportionality is the conductance G that is inversely proportional to the transverse area of the sample and that linearly depends on its length L and on its conductivity σ, the latter being a characteristic of the material. However, when the dimensions of the system scale down to the atomic level quantum effects start to be more and more relevant. The quantum contributions come from electrons which scatter only

elastically along their way through the device. Clearly this is strictly connected with the length of the mean free path l_e with respect to the device size L. The mean free path l_e ie the average distance an electron can travel before colliding with impurities and defects in the sample losing memory of its initial energy/momentum. If $l_e \ll L$ the transport is called diffusive while for $l_e > L$ we have the so called ballistic regime. In the first case electrons scattering is the dominant process governing the transmission, with the consequent energy loss and Joule effect, while in the second no inelastic scattering takes place (Fig. 3.14). The conductance in this ballistic regime

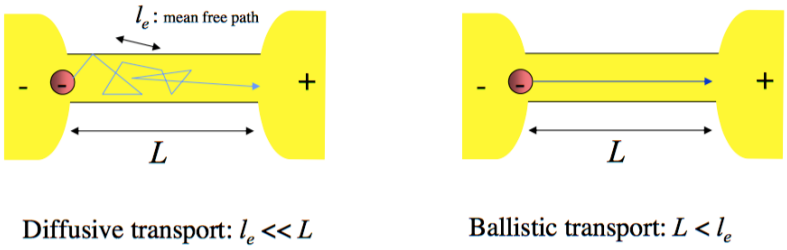

Figure 3.14: Schematic illustration of diffusive and ballistic regimes.

becomes quantized [70] and no evident relation exists between I and V.

3.8.1 Transmission function

A widely used approximation to calculate the current in quantum regime consists in considering the the transmission function $T(E,V)$ as independent from the applied voltage V, i.e. $T(E,V) = T(E,V=0)$. In some cases, essentially for very small biases, this approach can give reasonable results but it does not exist an *a priori* justification for such a choice. Obviously the calculation of the dependence from V of $T(E,V)$ requires to consider the Fermi levels of the leads shifted one respect to the other by a quantity $V = \mu_L - \mu_R$. The system is no more in equilibrium and a charge rearrangement takes place. Taking into account this non equilibrium charge via Eq. (3.33), we calculate $T(E,V)$ for different biases up to 1.0 V. The curves obtained are reported in Fig. 3.15 for the two spin components. The two black lines starting at 0 eV and reaching -0.5 and 0.5 eV border the bias window where the $T(E)$ is integrated to calculate the current, while the black curve at 0 bias points out the transmission function already shown in Fig. 3.13. As expected, as the bias increases the shape of the curves changes because of the different charge distribution in the scattering region. A first difference observable between the two plots is that all the transmissions functions of the minority component result lower than that the correspondent curves of the majority component. Furthermore, the minority $T(E)$ functions are

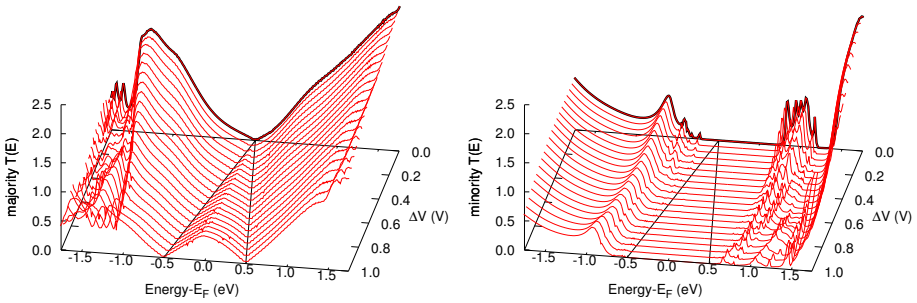

Figure 3.15: Transmission functions $T(E)$ for both spin components of the Fe@graphene nanojunction for the applied biases.

zero in a wide energy range well beyond the integration range. As already observed, these differences will reflect in different transmission behaviors.

A further detailed analysis can be performed considering the transmission function as the sum of the transmission coefficient at an intermediate bias. In Fig. 3.16 we report as a representative case the $T(E)$ function at 0.6 V. The main features are similar to those already analyzed in Fig. 3.11. Again, there are only two available states, i.e. two transmission channels, for each spin component. Also in this case the hybridization of the adatoms states with the graphene band induces deviations from perfect transmission.

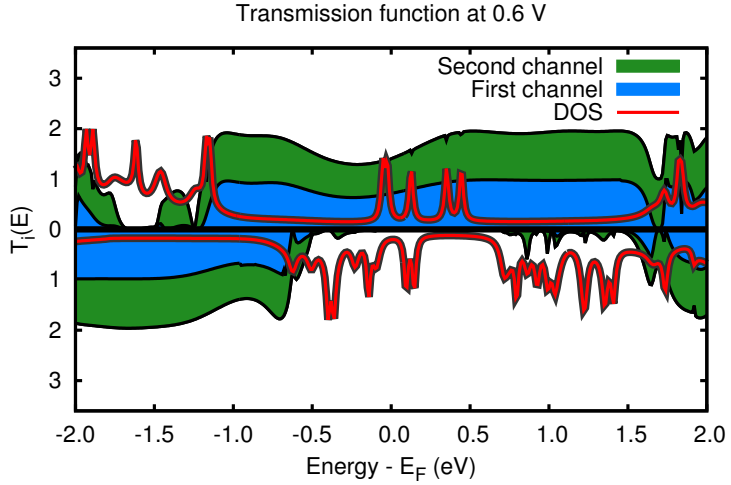

Figure 3.16: Transmission coefficients at 0.6 eV calculated at the Γ-point. The red line represents the density of states of the Fe atoms.

The main difference with respect to the equilibrium case is that the five Fe atoms are now subject to different potentials because of their positions within the scattering region. As a consequence, electronic states that where degenerate in the equilibrium case are now at different energies. This effect is particularly evident in the case of the $4s$ majority states that were practically indistinguishable at zero bias and now span an energy range of about 0.5 eV just above E_{F}.

3.8.2 Electronic current

In Fig. 3.17 we report the spin polarized current for our Fe@graphene nanojunction together with its spin polarization defined as

$$CP = \frac{|I_{\mathrm{Maj}} - I_{\mathrm{Min}}|}{|I_{\mathrm{Maj}} + I_{\mathrm{Min}}|}. \tag{3.39}$$

A strong polarization is observed: while the majority spin current displays a graphene-like behavior, the minority one is orders of magnitude lower than the majority for all the applied biases giving rise to a polarization of 100%. Since only electrons with a defined spin can flow through the scattering region, this junction can be considered a perfect spin filter.

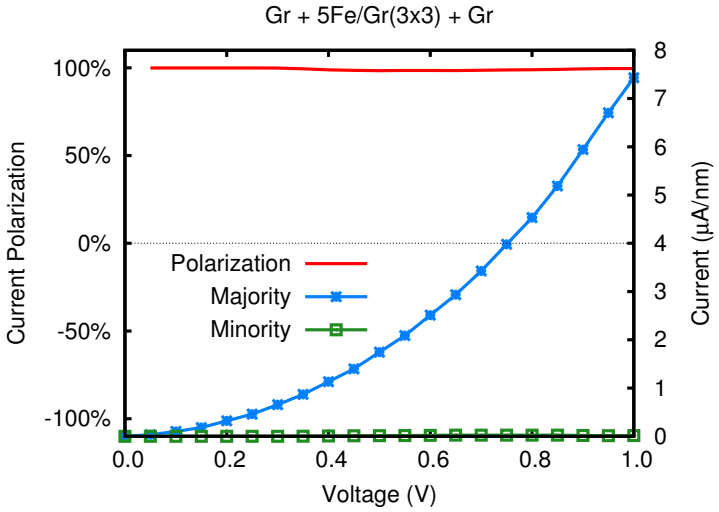

Figure 3.17: Spin-dependent electronic current and current polarization of Fe@graphene.

To evaluate the extent of the spin filter efficiency we performed further calculations restricting the scattering region. Keeping fixed both the number of carbon atoms and the total extension of the system we diminished the

number of Fe adsorbed atoms, passing from five to three and eventually to one. The resulting currents are reported in Fig. 3.18. We observe that the system with three iron atoms still displays a very high polarization for all biases. In the case of a single adatom the effect is undoubtedly less strong but in any case still present yielding a polarization always greater than 50%.

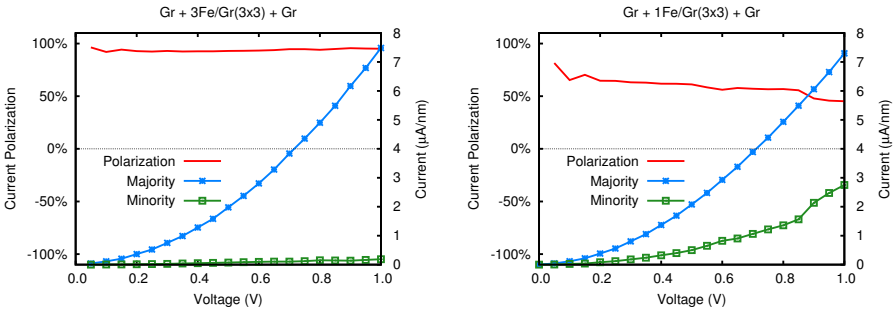

Figure 3.18: Spin-dependent electronic current and current polarization of Fe@graphene for different extension of the Fe adsorbed region.

3.9 Other Transition Metals

So far we have analyzed the transport properties of a graphene nanojunction with Fe adatoms. The choice was motivated by the peculiar spectral properties of Fe@graphene system pointed out in the investigation of the periodic systems. Fe@graphene electronic structure is in fact strongly spin-asymmetric: the majority spin electrons behave as in a small-gap semiconductor, while the minority ones show a clear insulating character. We verified that this behavior is still present in the open system and has significant effects on current transport.

Two others transition metals that display interesting electronic properties are Ti an Co. In fact, when adsorbed on graphene they both induce a half-metallic character in the substrate. In Ti@graphene the $3d$ shell is partially filled in the majority (up) component and empty in the minority (down) one. Conversely, in Co@graphene the $3d$ shell is more than half filled and the majority component is fully occupied, while the minority one is only partially filled (see Fig. 2.9 and 2.11). Therefore, under the assumption that all TM magnetic moments point towards the *up* direction, the strong reorganization of the electronic states in Ti@graphene (Co@graphene) takes place for the majority (minority) spin component, i.e. it mainly involves electrons of only one magnetic orientation. This asymmetry may possibly have appreciable consequences on the electron transport.

3.9.1 Transmission function and electronic current

The transmission function at zero bias of the two systems is reported in Fig. 3.19 together with the DOS in each nanojunction. The most striking feature is the presence of a wide energy gap in the $T(E)$ for one spin component only, namely the majority for Ti and the minority for Co. Such gaps in the $T(E)$ can be related to the ones observed in the band structure of the periodic system, which are delimited by graphene bands.

The transmission gaps extend from -0.2 to 1.0 eV in Ti and from -1.0 to 0.3 eV in Co, with respect to the Fermi level. The zero value of $T(E)$ appears at odds with the presence of electronic states within the same energy region.

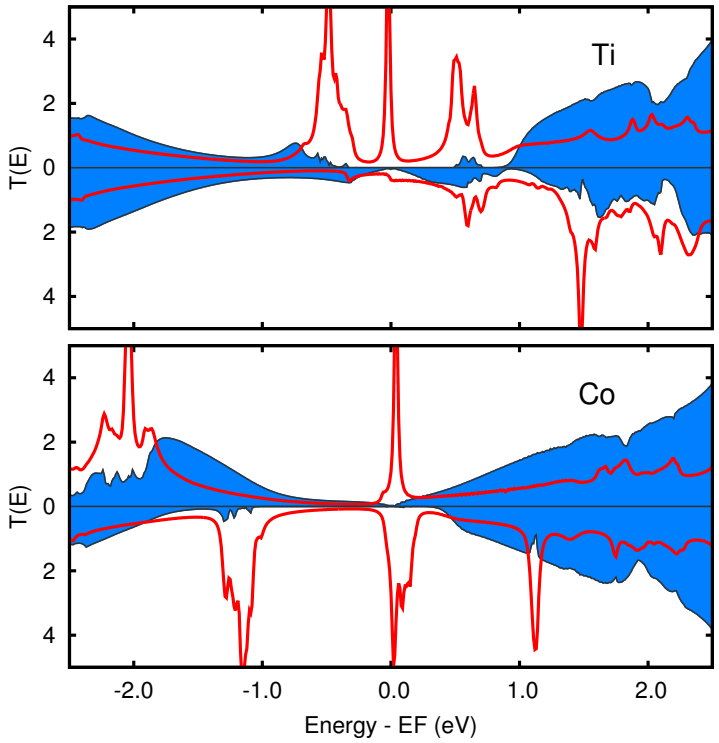

Figure 3.19: Transmission function of Ti (upper panel) and Co (lower panel) nanojunctions in comparison with the DOS in the whole nanojunction.

The 4*s* majority states of Ti and Co, despite being close to the Fermi level, yield negligible contribution to the metallic character of the system and behave as localized states not participating in the electronic transport. Also the 3*d* states lying in the gap (at $\sim$ 0.8 eV for majority spin of Ti and $\sim$ 0.2 eV for minority spin of Co) give very small contributions to the transmission, because of their poor hybridization with graphene.

It is worth noting that localized states lying in correspondence of conducting graphene bands act as scatterers for the incoming transmitted electrons, giving rise to Fano resonances and dips in the transmission (see for example the peaks at about 1.5 eV in the Ti minority spin component and at 1.1 eV in the Co minority spin component in Fig. 3.19).

In Fig. 3.20 we report the spin polarized current for Ti and Co together with the spin polarization. Since we apply a bias up to 1 V, only the integral of the $T(E)$ between -0.5 and 0.5 eV is relevant for the current. We find that in Ti@graphene only the minority spin carriers flow in the nanojunction, while the majority current is exactly zero up to a bias of 0.8 V. Starting from this value, the majority spin $3d$ states (at about -0.4 and 0.4 eV) enter in the bias window giving a small contribution to the transport. Consequently the spin polarization of the current is almost 100% in the whole bias range considered.

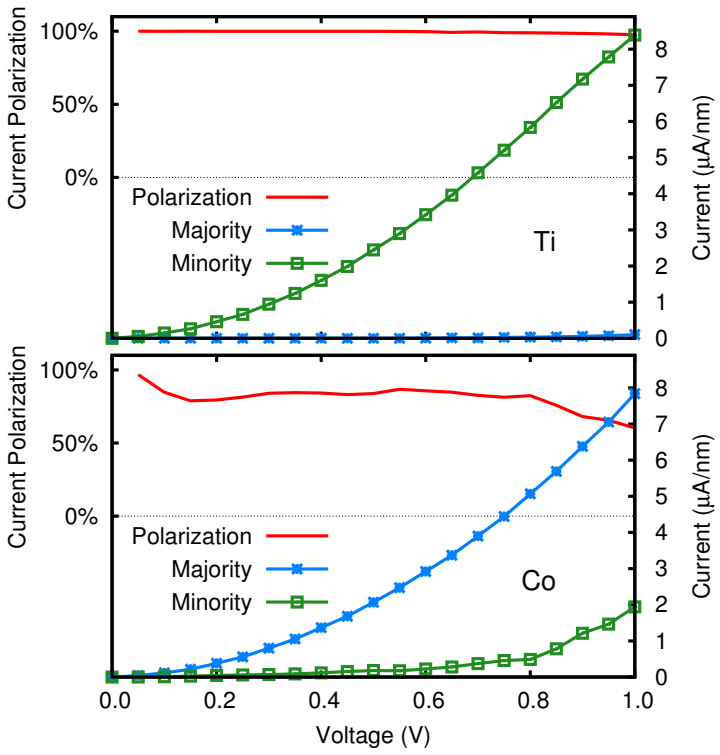

Figure 3.20: Spin-dependent electronic current and current polarization of Ti@graphene (upper panel) and Co@graphene (lower panel).

For Co@graphene the spin polarization is slightly smaller, although it reaches sizable values ranging from 65 to 90%. It is worth noting that in this case the spin polarization is opposite with respect to Ti, as already

observed for the transmission function. The reason of the lower spin-filtering efficiency of Co@graphene is dual: on one hand the majority spin current is smaller than that of the minority one of Ti because of the smaller DOS at the Fermi level. On the other hand the minority current is not exactly zero, but it slightly increases starting from 0.2 V. This is due to the small contribution of the $3d$ states around the Fermi level and of the graphene bands at 0.4 eV which contribute to the conduction at higher biases.

3.9.2 Electron density distribution

The electron density distribution (ED) of the systems under investigation has been analyzed within the framework of the Quantum Theory of Atoms in Molecules [36]. The total non-equilibrium electron density, as well as its majority and minority spin components, has been extracted from fully converged Green's function obtained with TranSIESTA [57], and its topological analysis has been performed with Critic2 [71].

A detailed topological analysis of the ED rearrangements of graphene upon adsorption of TM atoms has already been extensively discussed in Chapter 2. Here we focus on the major trends of the ED in the two systems investigated, presenting a comparison between the infinite periodic system and the open ones at 0 V bias. In the second part of this section, a detailed description of the effects of an applied bias and of the flowing of electrical current onto the electron density distribution in open systems is reported.

Table 3.1 includes the analysis of the periodic (closed) systems: as expected, Ti and Co transfer electron population to graphene. The overall electron transfer significantly decreases moving from Ti to Co, in agreement with the increasing electronegativity of the metal. The net charge on the TM is slightly smaller than the total negative charge of its nearest neighboring carbon atoms. The second nearest neighboring carbons are almost neutral, and bear a very small positive charge. In Ti@graphene, carbon atoms have an excess electron population in the majority spin component, and hence graphene enhances the magnetic moment of the metal. On the contrary, in Co@graphene the magnetic moment of carbon atoms is very small and opposed to that of the metal. The above features are confirmed also in the open systems, with negligible differences. The only discrepancy concerns the magnetic moment of Co, which is largely enhanced in the open system with respect to the periodic structure. This effect is due to the energy location of the $4s$ state of the metal with respect to the Fermi level in the majority spin band structure. Indeed, in the periodic system it lies just above E_{F}, and consequently is completely empty, while in the open system it crosses the Fermi level, thus retaining a relevant electron population (see Fig. 2.9 and 2.11). This induces a very small decrease of the electron transfer from Co to graphene, but has a great impact on the relative amounts of spin up and spin down populations of the metal.

Table 3.1: Charge and spin density analysis of TM@graphene 3×3 periodic and open systems at 0 V bias. C_{1st} refers to the entire shell of carbon atoms neighboring a single metal atom.

System/Atom	net charge	mag. moment
Ti@gr 3×3 periodic		
Ti	0.94	2.52
C_{1st}	−1.05	0.49
Ti@gr open system		
Ti	0.94	2.58
C_{1st}	−0.96	0.48
Co@gr 3×3 periodic		
Co	0.67	1.19
C_{1st}	−0.72	−0.08
Co@gr open system		
Co	0.59	1.93
C_{1st}	−0.68	−0.04

When an external bias is applied to TM@graphene open systems and an electrical current flows through the device, subtle but regular rearrangements in the ED take place. We report in Fig. 3.21 and 3.22 the magnetic moments for each of the TM atoms, labeled from 1 (left) to 5 (right). The electric current flows from left to right. Carbon atoms are grouped in three classes, on the basis of the region to which they belong: *i*) atoms belonging to the left contact region LC; *ii*) atoms belonging to the right contact region RC; *iii*) atoms belonging to the scattering region SR.

In the case of Ti@graphene, when an external bias is applied to the device the metal atoms clearly differentiate to one another. The atoms close to the LC region, Ti_1 and Ti_2, slightly increase their net magnetic moment, while the "central" atom (Ti_3) and the atoms close to the RC region (Ti_4 and Ti_5) behave at the opposite. The charge transfer from Ti to graphene increases as the bias increases, and at 1 V it reaches the value of 4.85 e, to be compared with 4.72 e at zero bias. Nevertheless, this difference does not explain the variation of the magnetic moment. As discussed previously, the current flowing through the device belongs nearly entirely to the spin down component. As a response, in left Ti atoms the imbalance between the majority and minority populations increases up to 0.40 V, where it reaches a plateau and, starting from 0.85 V, starts to decrease. An opposite trend is observed in the right Ti atoms: as the bias increases their spin down population increases while the spin up population decreases, following a quite regular trend and resulting in a decreasing magnetic moment.

As concerns carbon atoms in Ti@graphene, Fig. 3.21 clearly shows that

the LC and RC regions differentiate As concerns carbon atoms in Ti@graphene,

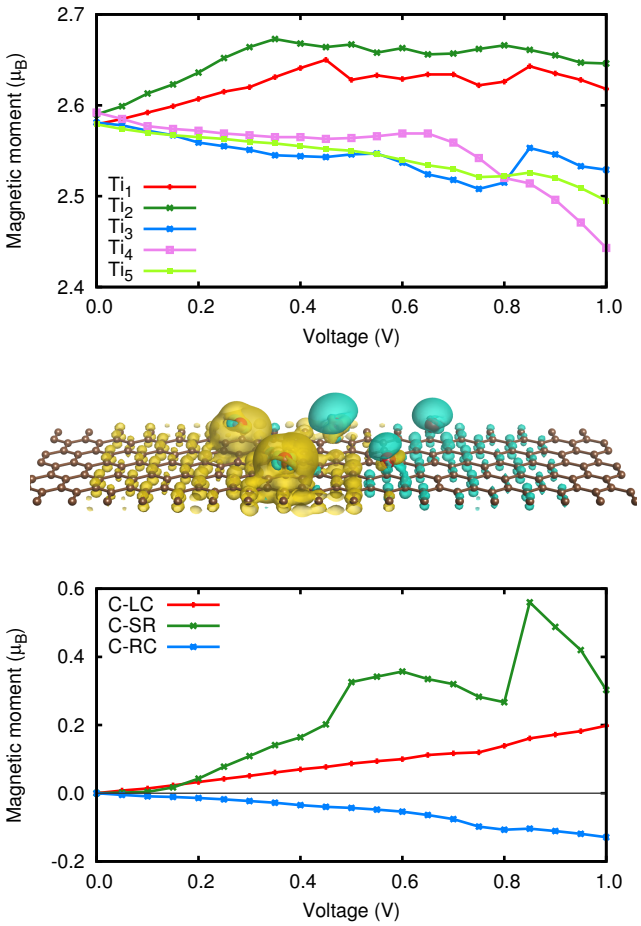

Figure 3.21: Magnetic moment (top panel) and variations of the magnetic moment (bottom panel) in Ti@graphene open systems as a function of the applied external bias. In the middle panel is reported the variation of the spin density upon the application of 0.6 V bias. The isosurface corresponds to a spin density equal to 10^{-4} electrons/Bohr^3 (yellow: spin up prevalence, cyan: spin down prevalence).

Fig. 3.21 clearly shows that the LC and RC regions differentiate from one another as the bias increases. Both regions bear a very small negative charge, about -0.05 e, which remains nearly constant when an external electrical field is applied and an electrical current flows through the device. However, the magnetic moments behave at the opposite: while carbons belonging to the LC region increase the spin up population (the component not transmitted by the device) and decrease the spin down population of an equivalent

extent, a reversed trend is observed in the carbons of the RC region (where only spin down current is flowing). The magnetic moment of C atoms belonging to the SR, which measures 5.80 μ_B at zero bias, increases significantly as the bias increases, reaching the maximum of 6.36 μ_B at 0.85 V, and then decreasing down to 6.10 μ_B at 1.00 V voltage. Overall, the increasing electron transfer from Ti to carbon remains located in the scattering region, and populates the spin up component of C atoms. At the same time, the electron population of the SR undergoes a further rearrangement, and electrons belonging to the spin down component populate spin up states.

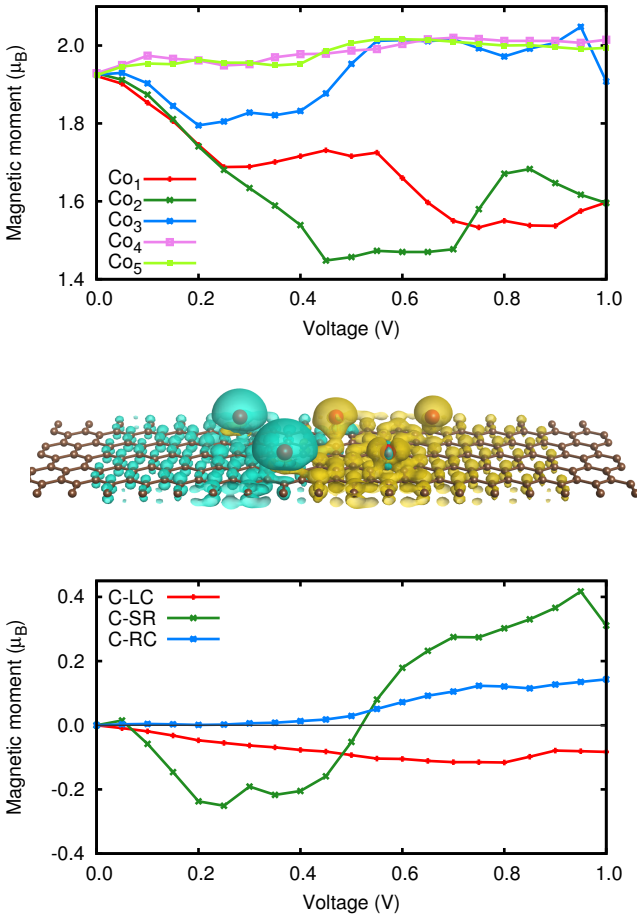

Figure 3.22: Magnetic moment (top panel) and variations of the magnetic moment (bottom panel) in Co@graphene open systems as a function of the applied external bias. In the middle panel is reported the variation of the spin density upon the application of 0.6 V bias. The isosurface corresponds to a spin density equal to 10^{-4} electrons/Bohr^3 (yellow: spin up prevalence, cyan: spin down prevalence).

Similarly, in the Co@graphene nanojunction, the electron transfer from the metal to the carbon atoms slightly increases as an external bias is imposed ($\sim 0.05\ e$ at 1.00 V bias), the excess population being located in the SR. However, in Co@graphene the current transmitted consists mainly of spin majority states, and the trends encountered in Ti@graphene are reversed.

As can be seen in Fig. 3.22, while the bias increases, the magnetic moment of the Co_1, Co_2 and Co_3 atoms on the left decreases, the feature being essentially due to an internal rearrangement between decreasing spin up population and increasing spin down one. This effect reaches saturation at 0.20 V bias in Co_3 and at 0.70 V in Co_2 and above these threshold values the trend is reversed. The atoms on the right, Co_4 and Co_5, present a very small but opposite trend, i.e. a slight and regular increase of spin up population at the expense of the spin down one.

The spin polarization of the electrical current induces a corresponding rearrangement in the relative up and down population of carbon atoms. The reflected current is made essentially of minority spin states: consistently, the spin down population becomes larger than the spin up one in LC, even if their overall charge is unchanged upon application of an external bias. Conversely, the transmitted charge in Co@graphene is made mainly of majority spin states. As expected, at increasing bias the spin up population of RC increases and the spin down population decreases by the same amount. Carbon atoms belonging to the SR present two distinct trends: at low bias (i.e. lower than 0.20 V) the spin down population increases while the other component decreases, at variance with the Ti@graphene system. Starting from a bias of 0.40 V and up to 1.00 V, the trend is reversed, with the spin up population increasing by 0.28 e, and the spin down one decreasing by 0.24 e. We note that also in Ti@graphene the rearrangement between spin up and spin down populations in SR reverses its trend at high voltages, more precisely at 0.85 V.

Under a finite applied bias, the component of the current backscattered by TM@graphene states, i.e. the majority spin one in the case of Ti and the minority spin one in the case of Co, induces a corresponding accumulation of spin up (Ti) or spin down (Co) in the left region of the device: LC, SR, and the "left" metal atoms (Ti_1 and Ti_2, or Co_1, Co_2 and Co_3). Conversely, the other component of the current, i.e. the one transmitted from the left to the right electrode, induces the accumulation of spin down (Ti) or spin up (Co) electrons in the right part of the device, i.e. RC and the "right" metal atoms (Ti_3, Ti_4 and Ti_5 or Co_4 and Co_5). As the applied voltage increases, the trends in magnetic moments are quite regular but for the portion of graphene belonging to the scattering region. Indeed, the overall behavior of SR results from the combination of different contributions: atoms neighboring the "left" metal atoms behave like LC, while the properties of those close to the "right" metal atoms are similar to RC ones.

3.10 Closing remarks

In this chapter we investigated the transport properties of a nanojunction composed by a magnetic central region, realized with a regular array of TM atoms adsorbed on graphene, contacted with two semi-infinite graphene electrodes. We started with the description of the Non Equilibrium Green's Function formalism, a rigorous theoretical framework for a quantitative and predictive analysis of carrier transport in nanostructures. Then we studied the spin-dependent electron transmission through a scattering region with Fe atoms adsorbed, first in equilibrium regime and then with an applied voltage. We found that the interaction between graphene and the adatom yields hybridized states in both spin components that significantly perturb the transmission function, while localized states act as scatterers for the incoming electrons giving rise to Fano resonances and dips in the $T(E)$. The most striking feature is the large gap comprising the Fermi level in the transmission function of the minority component only. As a consequence, the calculated currents for the two spin components are dramatically different displaying a 100% polarization for all the applied biases. The polarization effect is preserved even for smaller covered regions, even if to a minor extent. For the last part of our analysis we selected two other transition metal atoms, Ti and Co, which both have a partially filled $3d$ shell. We found that charge carriers flowing through the nanojunction in Ti@graphene belong almost entirely to the minority spin component, while the opposite is found in Co@graphene, where the charge carriers belonging to the majority spin component are dominant. The analysis of the non equilibrium electron density distribution indicates that a spin separation between the left and the right portions of the device occurs.

Chapter 4

Electronic transport in Porphyrin junctions

4.1 Introduction

In 1974 Aviram and Ratner proposed for the first time the use of an organic molecule contacting two electrodes as a current rectifier [1]. Since then, the idea of using single molecules as the functional units of electronic devices has been widely developed. The term molecular electronics is generally applied to systems involving a single molecule or a single layer of molecules bonded to two conductors, with the critical dimension between contacts in the range of one to a few tens of nm. Molecular devices can be operated by controlling their electronic state through electric and magnetic fields [72, 73]. Furthermore, in recent years a variety of interesting phenomena involving molecules in electronic circuits have been reported, including tunneling electron transport, conductance switching, photo-induced conductance changes and high density molecular memory [74, 75, 76].

A relatively new field of investigation is molecular spintronics, in which magnetic molecular junctions are used as spin transport channels [77]. Recently a number of experiments and theoretical works suggest that organic materials can offer similar and perhaps superior performances in making spin-devices than the more conventional inorganic metals and semiconductors [78, 79, 80]. Among organic materials, porphyrins are considered promising candidates because they offer a variety of desirable features such as highly conjugated structure, rigid planar geometry and good chemical stability [81]. High spin filter efficiency has been theoretically demonstrated for FeN_4 complexes contacted to graphene nanoribbons or single-walled carbon nanotubes [82, 83, 84]. Since electronic currents can be controlled by chemical doping of the molecule in the junction, iron porphyrin (FeP) junctions have also been investigated as possible components in gas sensing devices [85, 86, 87, 88].

Contacting single molecules in molecular electronics devices is a complicated task because it requires adaptable and robust atomic-size electrodes energetically aligned with the molecular orbitals [89]. A variety of fabrication approaches have been developed, including mechanical [90] and electromigrated [91] break-junctions and scanning probe techniques [92]. Single-molecule rectifiers [93], transistors [94] and switches [95] have been experimentally demonstrated, and the read-out and manipulation of a single-molecule nuclear spin has been achieved [96]. As to fabrication of molecular devices, it has been reported that a phthalocyanine molecule can be located between gold wires by manipulating single gold atoms with a STM tip [97].

In this context we study the structural, electronic and spin dependent transport properties of a molecular junction composed of a Fe porphyrin molecule contacted with two graphene electrodes. In order to investigate its possible exploitation in gas sensor devices we also analyze the interaction of our system with two gas molecules, CO and O_2.

4.2 Structure

The system under study consists of a Fe porphyrin molecule bonded to two semi-infinite graphene layers (see Fig. 4.1). The carbon dangling bonds are saturated with hydrogen atoms. The width of the nanojunction, 3 carbon-pair lines in the transverse direction, is the smallest one in which the FeP molecule can be embedded. With this geometric arrangement we want to stress the 1-dimensional character of the junction: the current should flow only through the molecule.

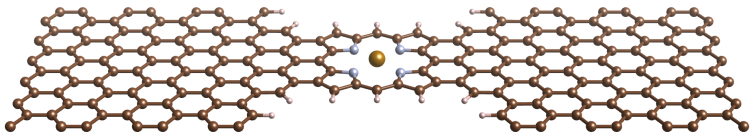

Figure 4.1: Fe porphyrin molecule contacted to graphene electrodes.

In previous studies FeP molecules are contacted with gold, which is the classic electrode material for metal-molecule junctions [85, 86, 87, 88]. In all cases the molecule is bonded to the lead *via* a thiol anchor group, forcing the current to flow through a single atom. Besides this arrangement, also carbon-based electrodes such as graphene nanoribbons or carbon nanotubes have been proposed for contacting molecules [82, 83, 84, 98, 99]. Graphene in fact displays low atomic mobility at room temperature, resulting in atomically stable electrodes [100]. In particular, the synthesis of a Fe-porphyrin-like carbon nanotube has been demonstrated where a seamless incorporation

of the FeP molecule in graphene results in excellent contacts between the active site and the conducting wires [101]. Given this background, we simulate a system in which the current is indeed forced to flow through the magnetic region but where the 2D nature of graphene is fruitfully exploited in the contacts. In our junction the single bonding atom is now replaced by a more extended contact with pure graphene leads.

Before performing geometric relaxation we determine the optimal size of the structure minimizing its total energy. The calculation is done considering only the the central region and neglecting the outer 48 carbon atoms on each side, 24 belonging to the electrodes and 24 belonging to the buffer region where the perturbation effects induced in the scattering region should decay. The relaxation of the molecule contacted with graphene should in fact be influenced only by the first neighbors and not by the presence of additional external C atoms. In Fig. 4.2 is shown the plot of the total energy of the central region as a function of the dimension.

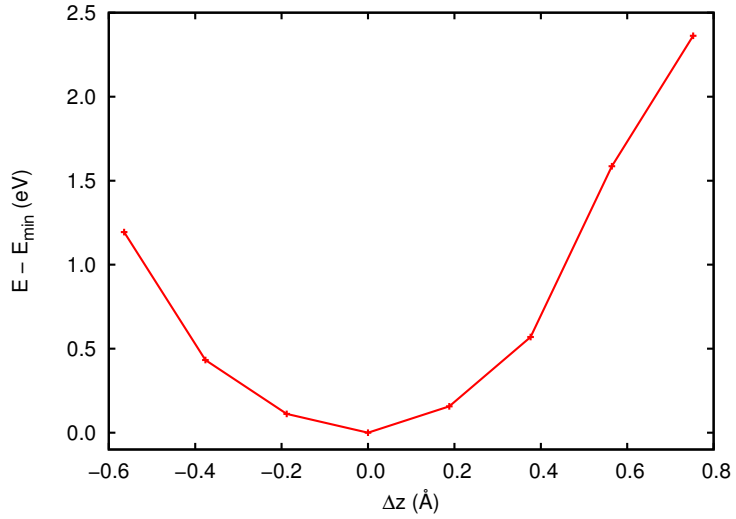

Figure 4.2: Total energy of the junction as a function of the dimension of the cell. Both quantities are referred to the equilibrium value.

The geometric optimization is performed considering the complete junction and relaxing all the atoms but the two electrodes plus an additional transverse line of C atoms. The embedding of an iron porphyrin in a graphene junction has small effects on the structural properties of the molecule. The N−N distance in the direction parallel to the junction remains unchanged, while in the perpendicular direction the two N atoms approach by 0.03 Å. As a result, Fe−N measures 1.98 Å to be compared with 1.99 Å in the isolated FeP.

4.3 Spectral properties

The magnetic moment of the isolated FeP molecule measures 2.0 μ_B and is localized on the Fe atom. In agreement with literature results [102] the occupancy of the $3d$ shell is $(d_{z^2})^2(d_{x^2-y^2})^2(d_{xz})^1$ $(d_{yz})^1$ (see Fig. 4.3), the last two orbitals being degenerate as a consequence of the molecular symmetry.

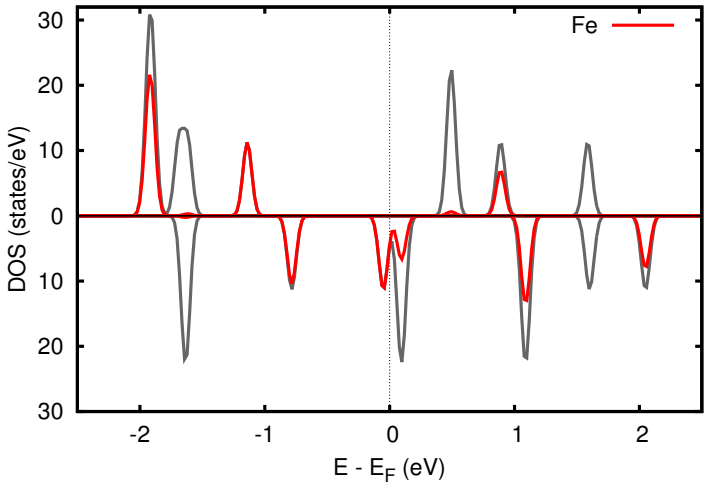

Figure 4.3: Spin-resolved DOS of the isolated FeP molecule. The red line represents the projection on the Fe orbitals.

The highest occupied molecular orbital (HOMO) of both spin components is a d_{z^2} Fe state. The lowest unoccupied molecular orbital (LUMO) has a d_π character in the minority spin component, while in the majority one is a delocalized state.

As concerns the nanojunction, the inclusion of a magnetic molecule in a graphene network is expected to produce a noticeable spin imbalance. The calculated magnetic moment results in fact equal to 2.0 μ_B. To evaluate the polarization effects we calculate the density of states of the nanojunction, reported in Fig. 4.4 together with the projection on the central Fe atom.

In the total DOS the characteristic shape of pristine graphene DOS is clearly recognizable. Of course other features, strictly related to the specific system, are present. The orbital occupancy rearrangement of the FeP molecule results in four occupied majority states and two minority ones. The former are the d_{z^2} and $d_{x^2-y^2}$ orbitals which display a localized character, along with two d_π states that hybridize with graphene. In the minority component only two sharp peaks $d_{x^2-y^2}$ and d_{xz} are visible below the Fermi level. The unoccupied states are a localized d_{xy} majority one and a more

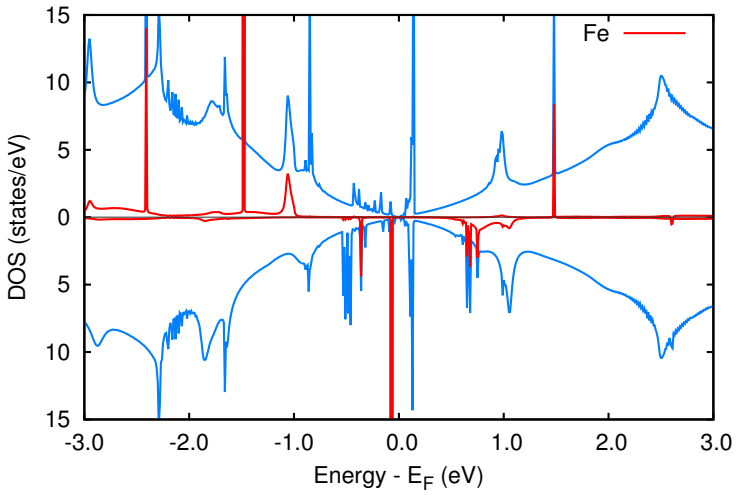

Figure 4.4: Spin-resolved DOS of the FeP junction. The red line represents the projection on the Fe orbitals.

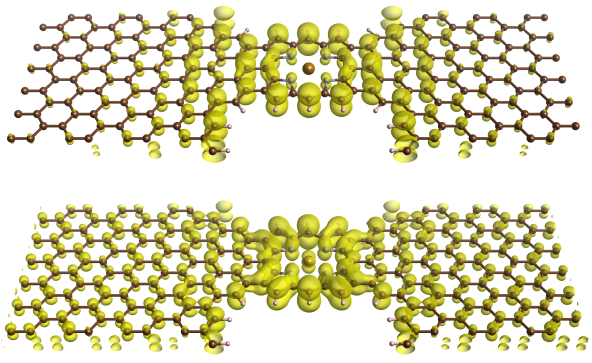

Figure 4.5: Local DOS of the molecular orbital at 0.20 eV (upper panel) and of the molecular hybridized states (lower panel).

delocalized minority d_{yz}. The embedding of the FeP molecule in the nano-junction implies the reduction of the molecular symmetry. The longitudinal and transverse directions are in fact no more equivalent. As a consequence the two LUMO orbitals, degenerate in the isolated molecule, split in energy. The sharp non magnetic state visible just above E_{F} is in fact the unoccupied molecular orbital of lower energy (see Fig. 4.5, upper panel). The slightly magnetic broad peaks situated at $\sim$ 1 eV are molecular states hybridized with graphene (see Fig. 4.5, lower panel).

The dispersion of the different states can be analyzed considering the density of states for each $k_{\parallel}$ reported in Fig. 4.6. The projected energy gap of the graphene electrodes already observed in Fig. 3.8 is visible in both spin components. As concerns the majority component, the hybridized states at ~ -1.0 and ~ 1.0 eV display a negligible dispersion. A similar behavior is found for the strictly localized state at ~ 1.5 eV. The dispersing state below the Fermi level and belonging to the projected gap is prevented to propagate into the bulk substrate. This edge state displays a 1D character. In fact, in the region where the FeP molecule is connected with the electrodes the junction has a zig-zag edge of carbon atoms saturated with hydrogen where these states are localized [103]. The tiny dispersion shown by the molecular state just above E_{F} tells us that the interaction between the molecule replicas along the y direction is negligible and that the transverse dimension of the junction is appropriately selected. In the minority component similar features can be pointed out, the main difference being an unoccupied edge state that enters in the gap in correspondence of the the mid-point of the $\overline{\Gamma} - \overline{\mathrm{X}}$ path.

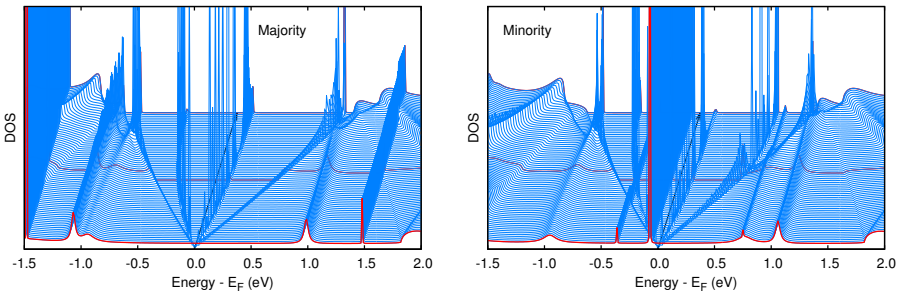

Figure 4.6: k-resolved DOS for the two spin components. The red lines at $\overline{\Gamma}$, $\overline{\mathrm{X}}$ and at the mid-point of the $\overline{\Gamma} - \overline{\mathrm{X}}$ path are highlighted for a better reading of the plot ($\overline{\Gamma}$ being in the foreground and $\overline{\mathrm{X}}$ in the background). The black arrow represents the Fermi level.

4.4 Transmission properties

The transmission function of the nanojunction with no applied bias is reported in the upper panel of Fig. 4.7. In the same plot a green line represents the density of states. Around the Fermi level the transmission function has a smooth shape that nicely reminds that of pristine graphene. Due to their localized character the sharp Fe states of the minority component discussed in the previous section do not produce relevant effects in the transmission. As can be observed in the lower panels of Fig. 4.7 this behavior does not change even upon bias application.

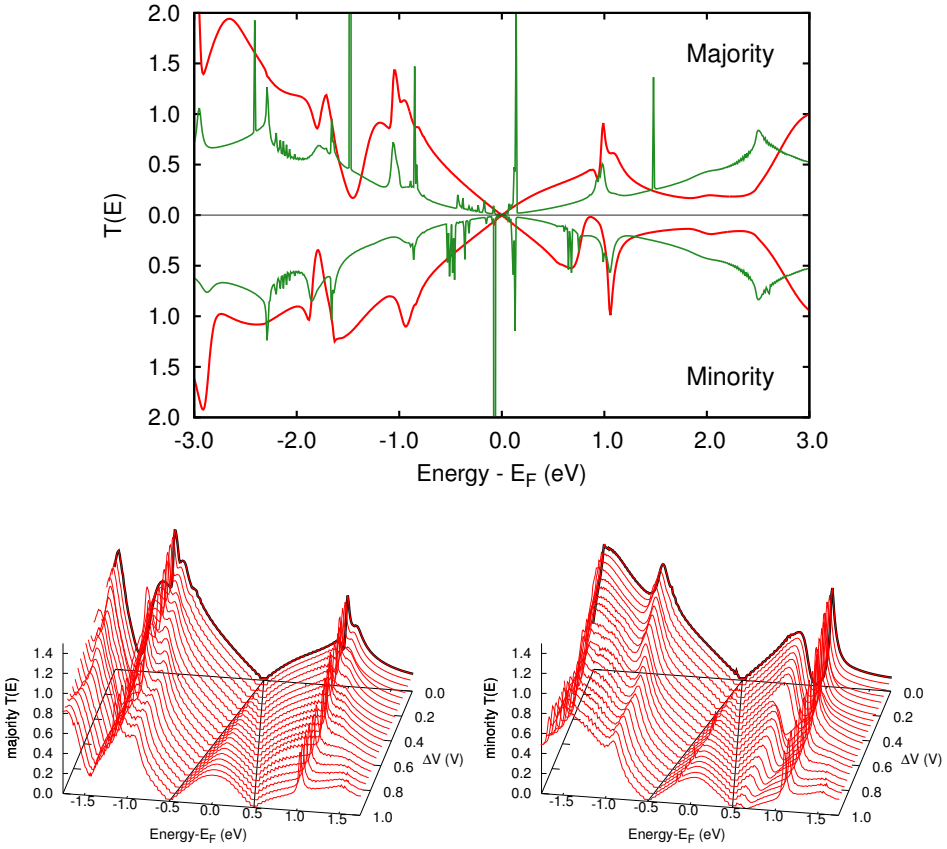

Figure 4.7: Upper panel: transmission function at zero bias of the nanojunction. The green line represents the density of states. Lower panels: transmission functions for all the applied biases.

The resulting current is reported in Fig. 4.8. The two spin components are indistinguishable at low biases, start differentiating around 0.5 V but the resulting polarization is nevertheless negligible. So far we can conclude that despite the magnetic character of the junction no relevant spin dependent

behaviors can be pointed out.

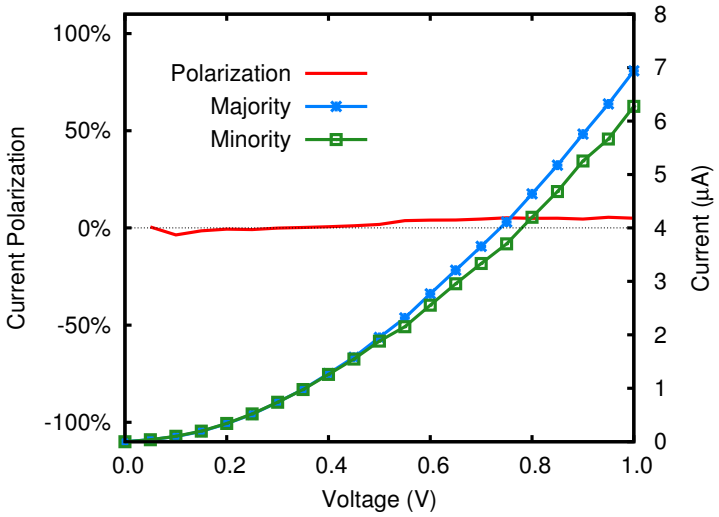

Figure 4.8: $I(V)$ curve in the FeP nanojunction.

4.5 Doped electrodes

The absence of polarization effects observed in the current flowing through the FeP nanojunction can be ascribed to the graphene vanishing density of states at the Fermi level that causes a a poor interaction between the magnetic atom and the carbon network. Chemical doping represents a natural way of increasing charge carriers density in graphene while preserving its remarkable transport properties [104, 105]. When dopants are introduced the Fermi level is shifted with respect to the Dirac point and the DOS around E_{F} is no more negligible. Doping of graphene with elements adjacent to carbon in the periodic table, i.e. boron and nitrogen, has been experimentally demonstrated [104, 106]. The group III element boron introduces a hole, i.e. it acts as a p-type dopant, while the group V element nitrogen donates an electron and thus acts as an n-type dopant.

In this context, we consider three different systems analogous to the one discussed above but for the doping of the carbon electrodes. In one case they are both doped with boron, in another with nitrogen while in the last one the left electrode contains a boron atom and the right a nitrogen atom. In all cases the electrodes are made of 48 atoms to obtain a diluted dopant concentration ($\sim$ 2%). To evaluate the effect on the electronic properties produced by the impurities, in Fig. 4.9 we compare the density of states of the differently doped electrodes with that of pure graphene. As expected,

with boron doping the downshift of the Fermi level of about 0.75 eV gives rise to a p-doping, while in the case of nitrogen an upshift of the same amount takes place producing a n-doping.

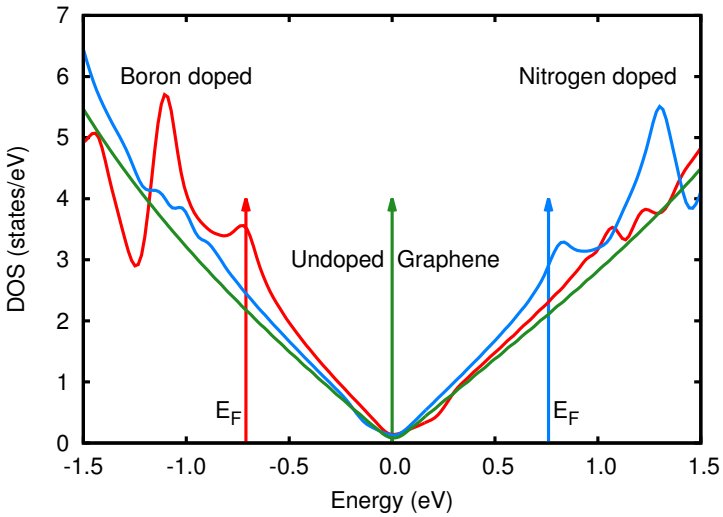

Figure 4.9: DOS of the doped electrodes (red for boron and blue for nitrogen) compared with that of pristine graphene (green).

To verify whether the effects produced by the substitutional atoms are confined in the leads or involve the whole system we calculate the spin-resolved DOS of the scattering region, shown in Fig. 4.10 together with the DOS of the pristine system. The Fermi level shift observed in the electrodes is still clearly visible in both cases. This proves that even with a poor concentration the presence of a dopant can significantly perturb the spectral properties of the system.

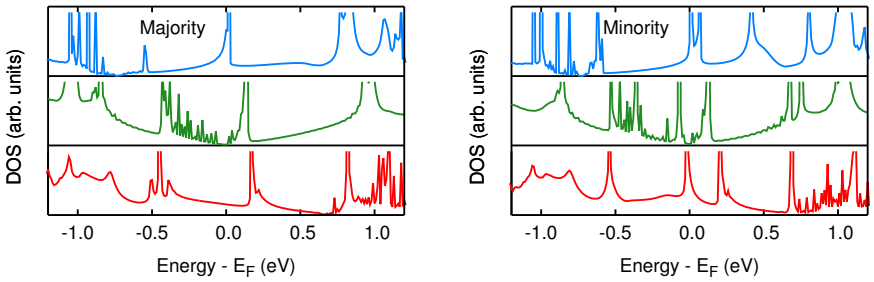

Figure 4.10: DOS of the nanojunction with undoped (green) and doped (B in red and N in blue) electrodes.

In the previous section we observed that Fe atoms states around E_F do not produce effects on the transmission because of their localized character. In this case, with a non negligible density of states around the Fermi level hybridization between iron and carbon states can indeed take place. To determine which Fe states are possibly involved we calculate the density of states projected on the Fe atoms in presence of the two dopants, to be compared with the same plot for pure electrodes (see Fig. 4.11). In the majority component no states are visible in a wide energy region comprising the Fermi level, thus no differences with respect to the undoped system are expected. Differently, in the minority component many Fe states are present. In particular, in the B-doped case a state at -0.2 eV displays a hybridized character, and a similar feature is visible in the N-doped system at ~ 0.5 eV. Similarly to what takes place in the undoped case, other sharp states are not expected to produce relevant effects.

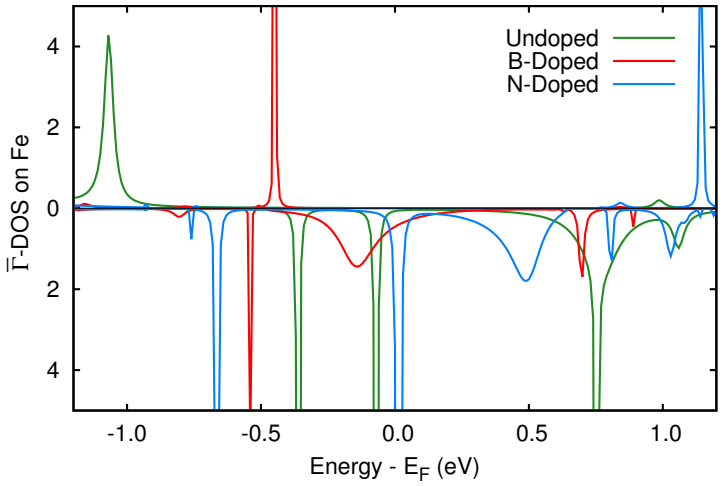

Figure 4.11: $\overline{\Gamma}$-density of states projected on the Fe atom for the undoped (green) and doped (B in red and N in blue) systems.

4.5.1 B-doped system

In Fig. 4.12 is reported the current of the boron-doped system. Differently from the undoped case, at low biases the relation between I and V is linear. This is due to the significant presence of electronic states at the Fermi level.

At 0.15 V the two spin components start to separate giving rise to a polarization. While the majority keeps on growing linearly, the minority remains approximately constant for a small bias range and then starts in-

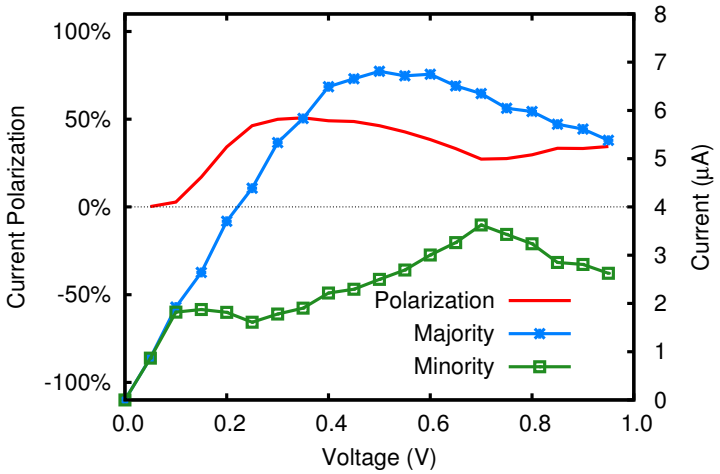

Figure 4.12: $I(V)$ curve in the FeP nanojunction with B-doped electrodes.

creasing again, even if with a smaller slope. At high voltages both currents start decreasing but remain well separated resulting in an average polarization of $\sim 40\%$.

The transmission function at zero bias is shown in Fig. 4.13. As expected, the curve is shifted with respect to the undoped case. The zero of the $T(E)$ curve is now located at ~ 0.75 eV above E_{F}, according to the nil density of states of the electrode at the same energy (see Fig. 4.9). The majority component displays a regular trend, while in the minority one a dip is visible at -0.2 eV. This feature is due to the presence of the Fe state discussed above that hybridizes with the graphene states causing a scattering in the propagating electrons with the consequent decrease in the transmission. Accordingly, the system displays a non negligible polarization.

Considering the $T(E)$ reported in the lower panels of Fig. 4.13 we observe that the dip responsible for the decrease in the minority component falls within the bias window for all the applied biases. As a consequence, the transmission of the minority component is lower than the majority one resulting in a lower current.

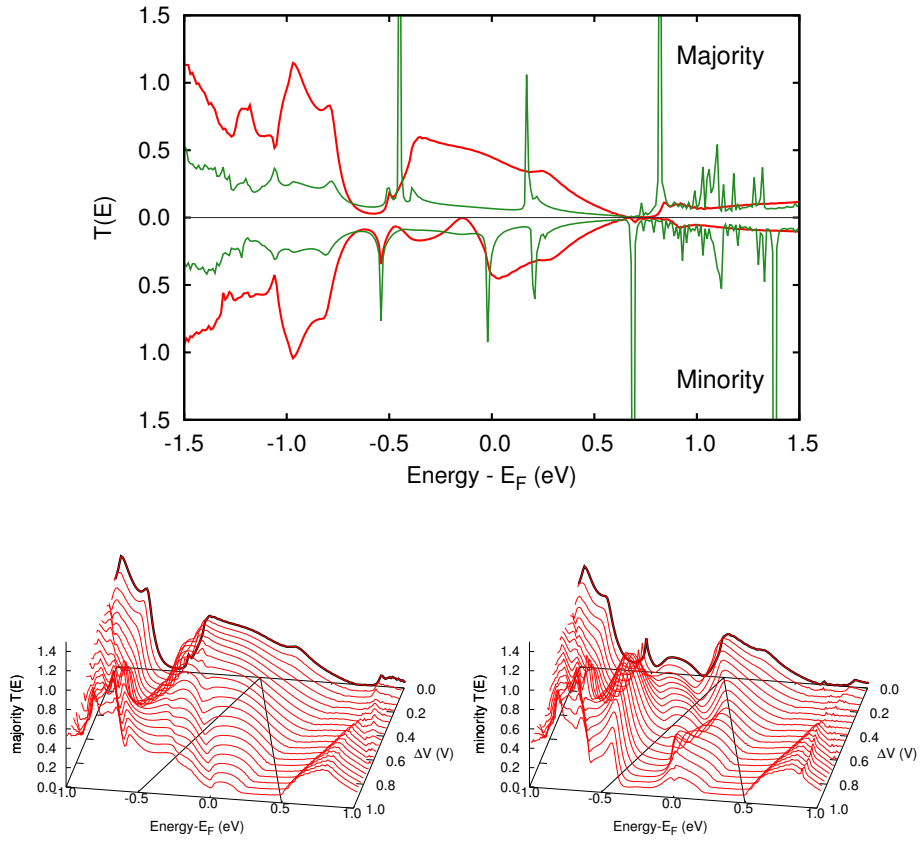

Figure 4.13: Upper panel: transmission function at zero bias of the FeP nanojunction with B-doped electrodes. The green line represents the density of states. Lower panels: transmission functions for all the applied biases.

4.5.2 N-doped system

When the graphene electrode is doped with a nitrogen atom the Fermi level is shifted 0.75 eV above the Dirac point (see Fig. 4.9). The current flowing through the junction is shown in Fig. 4.14. The linear behavior at low biases already found in the case of B doping is still present and persists up to 0.40 V in both spin components. Starting from that voltage the majority current remains approximately constant while the minority one preserves its linear trend, giving rise to a minor polarization. At 0.55 V both currents start decreasing showing a Negative Differential Resistance (NDR) behavior. As a consequence of the different slopes of the two decreasing currents, at 0.65 V the minority becomes smaller than the majority yielding an inversion in the polarization, which attains a constant value of ∼20%. At 0.80 V the NDR effect ceases and both currents start growing again as the the bias increases.

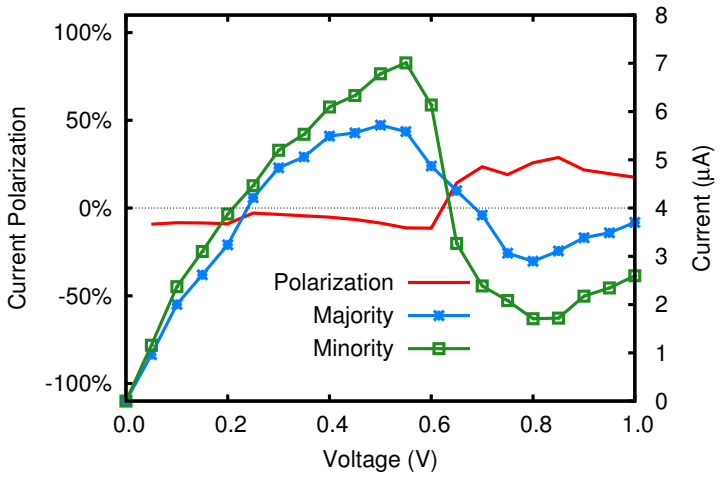

Figure 4.14: $I(V)$ curve in the FeP nanojunction with N-doped electrodes.

To investigate the causes of the NDR behavior we consider the transmission functions for different applied biases, reported in Fig. 4.15. The zero in the $T(E)$ function with no bias applied visible at ~ -0.75 eV reflects the gap in the density of states of the doped electrode (see Fig. 4.9). As the voltage increases the electrodes DOS are shifted one with respect to the other and two points of vanishing $T(E)$ are visible at a distance corresponding to the applied bias (see, for example, the zero points at ~ -0.50 eV and at ~ -0.90 eV in the T(E) at 0.40 V). Since the current is obtained from the integration of the transmission function in the bias window, when one of these points enters the bias window the absence of states produces a decrease of the current in both spin components.

A similar phenomenon can be invoked to rationalize the strong reduction of the minority current around 0.60 V responsible of the polarization inversion. Looking at the $T(E)$ plot at zero bias a significant gap at 0.5 eV is visible in the minority component due to the hybridization of a Fe state with graphene. At 0.60 V this gap enters the bias window resulting in a decrease of the minority component only.

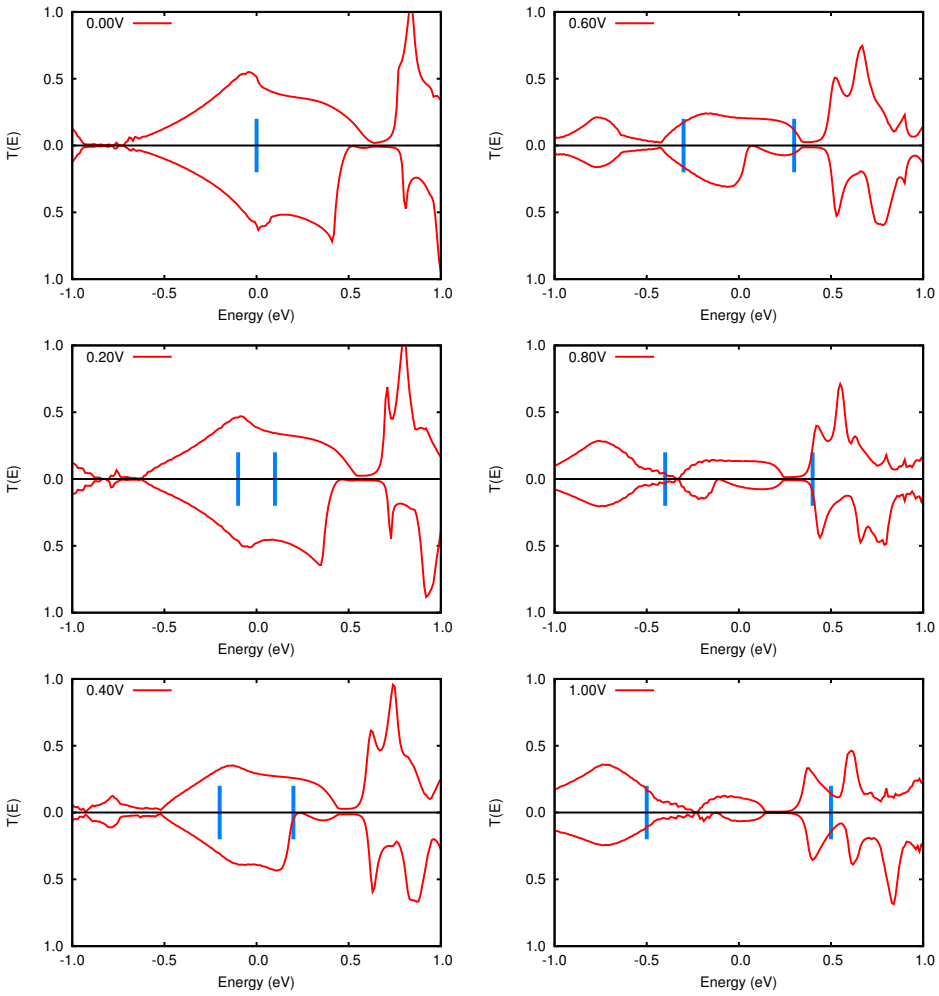

Figure 4.15: Transmission functions for the different applied biases in the N-doped FeP junction. The blue lines represent the bias window for the integration.

4.5.3 BN-doped system

In the last system analyzed the two electrodes are differently doped, one with a B atom and the other with a N atom.

Because of the different dopants, the system looses the left/right symmetry and the resulting current has different values for negative or positive applied biases (see Fig. 4.16). In fact, the positive current flowing from the B-doped electrode to the N-doped one (from left to right) reaches at 0.5 V a value of about 10 μA, while for the opposite bias the current is equal to 6 μA. Thus this system displays a partial rectification behavior. Similarly

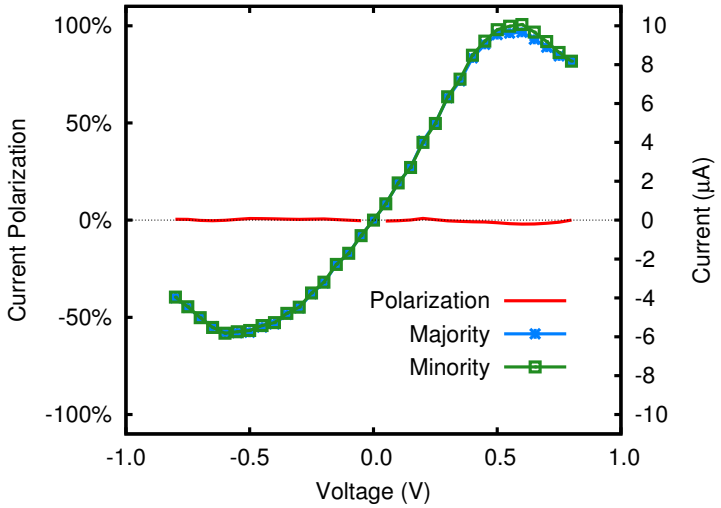

Figure 4.16: $I(V)$ curve in the FeP nanojunction with B/N-doped electrodes.

to what already observed in the case of a single dopant, for low biases the relation between I and V is almost linear. Then, around ± 0.5 V a NDR behavior is observed. Interestingly, the spin polarization disappears for all biases.

4.6 Gas molecules adsorption

Sensing gas molecules is critical to environmental monitoring, control of chemical processes, agricultural and medical applications. Due to this huge application range the need of cheap, small, low power consuming and reliable solid state gas sensors has grown over the years. The most frequently reported sensors are metal oxide semiconductors, which work on the principle of change in conductivity upon interaction with gas molecules. Although these metal oxide gas sensors have considerable applications, some problems related to stability sensitivity, and selectivity must be overcome. In order to get over these issues, a huge research is under way directed to explore sensors which are stable, selective, highly sensitive and with a quick response mechanism. In this regard, an increasing number of theoretical and experimental studies have demonstrated that nanoengineered devices and materials are the key to solve the problems of poor sensitivity and selectivity.

Thanks to their unique functions of molecular recognition and chemical selectivity organic molecules are considered interesting candidates for gas sensing devices. In particular, cyclic conjugated molecules are attracting great attention because their electronic properties can be tuned by changing

the size of the rings or incorporating functional coordination groups [107]. Extensive theoretical and experimental investigations have proved that in Fe porphyrin molecules the current through the coordination ion can be modulated with the adsorption of a target molecules [108, 109, 110]. Thus, nanoscale sensors utilizing porphyrin molecules have great potential to exhibit high sensitivity and chemical selectivity.

In this context, we investigate the changes in the spin-polarized currents of the FeP junction owing to the adsorption of CO and O_2 gas molecules, in either case of undoped and doped electrodes.

4.6.1 Geometric structures

The first step of our analysis consists in determining the optimized adsorption geometries of the two gas molecules on the FeP junction.

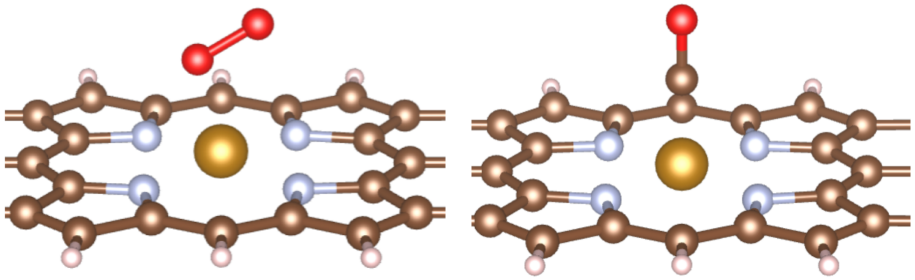

Figure 4.17: FeP junction with the adsorbed O_2 (left panel) and CO (right panel) molecules.

After optimization the CO molecule is adsorbed perpendicular to the junction with the C atom bonded to Fe and a slightly elongated bond length, 1.17 Å with respect to 1.13 Å in the gas phase (see Fig.4.17). For FeP$-O_2$, the oxygen molecule connects to Fe atom in an *end-on* geometry through the interaction between Fe d_{z^2} and O_2 π^* orbitals, leading to a bent structure with an angle $\angle\ \mathrm{Fe}-\mathrm{O}-\mathrm{O} = 107°$. Also in this case the interatomic O$-$O distance increases from 1.21 Å in the free molecule to 1.29 Å. The adsorption energies are 2.00 eV and 1.10 eV for CO and O_2, respectively. Upon O_2 adsorption the magnetic character of the junction is preserved while the interaction with the CO molecule totally quenches the magnetic moment. These results well compare with theoretical and experimental previous studies [111, 112].

4.6.2 Transmission function and electronic current

The transmission functions and the current of the FeP junction with the O_2 adsorbed molecule are reported in Fig. 4.18.

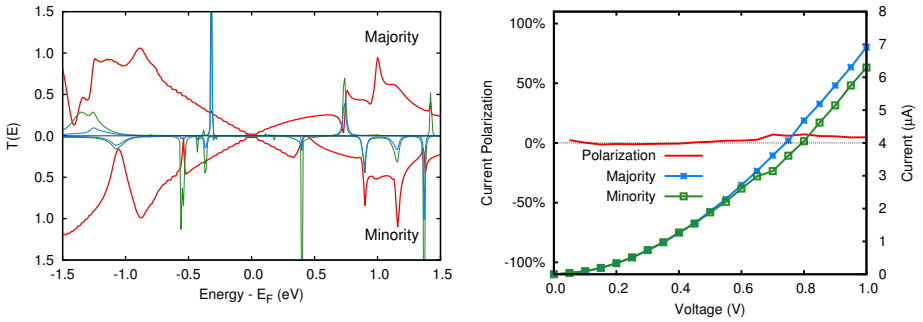

Figure 4.18: Left panel: spin-resolved transmission function at zero bias for the O_2 adsorbed FeP junction. The green line represents the density of states projected on the both the O_2 molecule and iron atom, while the blue one only on the latter. Right panel: spin-resolved electronic current and current polarization for the O_2 adsorbed junction.

As already observed in the case of TM@graphene, we can see that the presence of the iron states can produce different effects on the transmission function. Focusing on the majority component, we observe a largely hybridized state around -1.3 eV that causes a noticeable decrease in the $T(E)$. The sharp state at -0.3 eV does not influence the smooth trend of the plot in that energy region and the two states above the Fermi level give rise to Fano resonances. Similar effects can be pointed out in the minority component. An interesting feature is visible at at ~ 0.45 eV which is responsible of the significant dip in the transmission function. Looking at the current we can see that for low biases the two spin components are indistinguishable, but at 0.70 eV the minority component undergoes a slight decrease caused by the perturbing state mentioned above that enters the bias window marginally preventing the transmission. The resulting minimal polarization is comparable to that observed in the pristine Fe porphyrin junction (see Fig. 4.8).

As previously observed, in the case of CO the system looses its magnetic character. The transmission function shown in Fig. 4.19 displays an unperturbed shape, at least in the energy region relevant for transport. Accordingly, the current is indistinguishable from that of the majority component of the pristine case (see Fig. 4.8).

These results show that this junction is not suitable as a possible active site of a gas sensor since no perceptible variations in the polarization or in the intensity of the current are observed upon adsorption of O_2 or CO gas molecules. We thus verified whether the use of doped electrodes could produce detectable effects. The calculated currents are reported in Fig. 4.20,

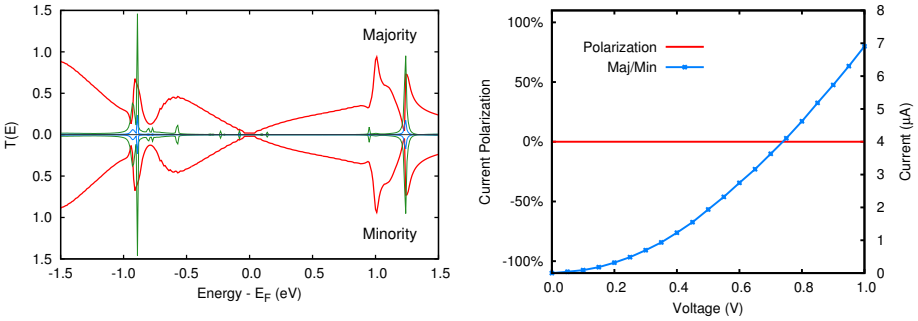

Figure 4.19: Left panel: spin-resolved transmission function at zero bias for the CO adsorbed FeP junction. The green line represents the density of states projected on the both the CO molecule and iron atom, while the blue one only on the latter. Even if in this case the system is non magnetic two spin components are shown for a better comparison with other results. Right panel: spin-resolved electronic current and current polarization for the CO adsorbed junction.

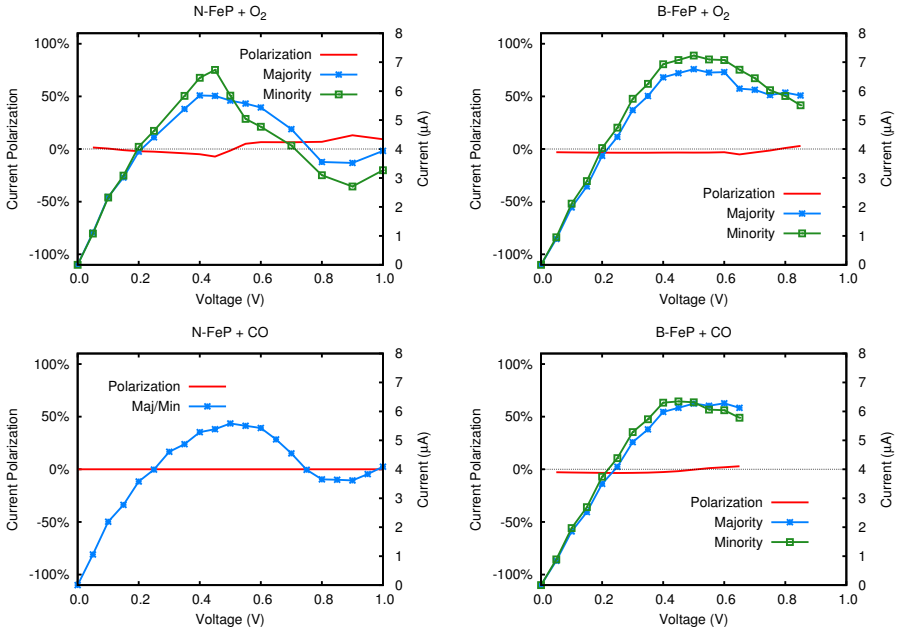

Figure 4.20: $I(V)$ curves for the B- and N-doped nanojunctions with O_2 and CO adsorbed molecules.

to be compared with the $I(V)$ plots shown in Fig. 4.12 and Fig. 4.14. As concerns the N-doped structure, the overall trend is confirmed, with a linear behavior at small biases and a decrease starting from $0.5-0.6$ V. Thus, no remarkable differences can be ascribed to the presence of the adsorbed gas molecules. Conversely, with B-doped electrodes a noticeable difference can be pointed out with respect to the unperturbed system. In fact in this case the adsorption of both gases removes the current polarization that in the pristine junction was never lower than 25%. In this sense a device based on such a system could not distinguish between the two gases but could in principle detect their presence by measuring a variation in the current polarization.

4.7 Closing remarks

A Fe porphyrin junction contacted with pure graphene leads has been investigated in order to characterize its transport properties. We started with the optimization of the size of the structure, then we studied the electronic properties of the junction together with their influence on the charge transport. We found that the localized Fe states do not produce relevant effects on the current which in fact displays only a slight polarization. We carried on our investigation considering the same FeP molecule contacted with doped graphene electrodes. In the B-doped system a non negligible current polarization is observed, while in the N-doped case a Negative Differential Resistance effect can be pointed out. Since the electronic properties of the metal atom can be modulated by the adsorption of a gas molecule, we devoted the last part of our study to the investigation of the possible employment of the FeP junction as a gas sensor device. We found that upon adsorption of O_2 and CO molecules only minor effects can be detected but a quenching of the current polarization in the B-doped system.

Conclusions

It has been extensively stated that graphene's unique properties make it a promising material for electronic applications. However, to usefully integrate graphene-based structures in systems capable of providing new desired functionalities significant challenges need to be overcome. Among them, the possibility of modulating its electronic and transport properties, for example with the opening of band gaps, represents a key topic without which no electronic exploitation of graphene can be envisaged. Furthermore, the tuning of its spin dependent properties allows its utilization in spintronics, the science of processing and controlling electron spins.

Aim of this thesis is the theoretical investigation of these aspects. We start addressing the band gap opening in graphene upon adsorption of transition metal atoms. Depending on the TM considered, we observe the opening of gaps with different widths and energies in the two spin components. Furthermore, the fact that some of these gaps comprise the Fermi level allows to speculate that the electron transport through these systems should display spin-dependent behavior. We then tackle the more complex topic of electron transport with particular attention to the spin dependent properties. In this case we have to deal with open, non periodic systems whose electronic properties cannot be easily obtained with standard methods. For the calculation of the charge transport we make use of the Non Equilibrium Green's Function approach, that provides a rigorous description of quantum transport allowing the self-consistent calculation of the charge density under a bias voltage. Within this framework, we investigate two different types of graphene junctions. The first type is made by a graphene sheet with transition metal atoms adsorbed in a regular array on a finite region. Our results show that with Fe adatoms the currents of the two spin components are dramatically different displaying a 100% polarization for all the biases considered because of a complete quenching of the minority current. Also for Ti we find a similar behavior but with an opposite polarization: in this case in fact we observe a damping of the majority current. Co adsorption induces a polarization analogous to that of Fe but less intense. The second system analyzed is a molecular magnetic junction where a Fe porphyrin molecule is connected with graphene electrodes. While in the pristine case no relevant effects can be pointed out, when the electrodes are doped with

boron atoms a non negligible current polarization is observed. The doping with nitrogen atoms gives instead rise to a different effect, namely Negative Differential Resistance, with a reduction of the current for increasing voltages. Finally, we address the problem of the possible employment of this molecular junction in a gas sensor device investigating the changes induced in the charge transport by the adsorption of two gas molecules, O_2 and CO. The only relevant effect observed is the quenching of the polarization in the B-doped system.

Our modeling of the junctions might look quite simple, yet it provides useful insights into the mechanism of spin filtering in this kind of systems. Some further investigations are nevertheless advisable. Without claiming to model a realistic device, the first topic that should be addressed is the analysis of the possible effects induced by a supporting insulating substrate on the electronic and transport properties. Another aspect that can play a key role in the modeling of nanodevices is the contact with metal electrodes which represent a further source of scattering and can thus influence the overall behavior. Last but not least, experimental results must be considered. Perfect junctions, comparable with those we analyzed, have not yet been realized and spin dependent transport data are available only for more "dirty" systems. Since at present direct comparisons between theoretical and experimental results are prevented, theoretical investigations can lay down the guidelines for the experimental research in a continuous and productive interplay.

Bibliography

[1] A. Aviram and M. A. Ratner. Molecular rectifiers. *Chem. Phys. Lett.*, 29:277, 1974.

[2] M. A. Reed, C. Zhou, C. J. Muller, T. P. Burgin, and J. M. J. M. Tour. Conductance of a molecular junction. *Science*, 278:252, 1997.

[3] M. N. Baibich, J. M. Broto, A. Fert, F. Nguyen Van Dau, F. Petroff, P. Eitenne, G. Creuzet, A. Friederich, and J. Chazelas. Giant magnetoresistance of (001)Fe/(001)Cr magnetic superlattices. *Phys. Rev. Lett.*, 61:2472, 1988.

[4] G. Binasch, P. Griinberg, F. Saurenbach, and W. Zinn. Enhanced magnetoresistance in layered magnetic structures with antiferromagnetic interlayer exchange. *Phys. Rev. B*, 39:4828, 1989.

[5] K. S. Novoselov, A. K. Geim, S. V. Morozov, D. Jiang, M. I. Katsnelson, I. V. Grigorieva, S. V. Dubonos, and A. A. Firsov. Two-dimensional gas of massless Dirac fermions in graphene. *Nature*, 438:197, 2005.

[6] J. M. Soler, E. Artacho, J. D. Gale, A. García, J. Junquera, P. Ordejón, and D. Sánchez-Portal. The SIESTA method for ab initio order-N materials simulations. *J. Phys.: Condens. Matter*, 14:2745, 2002.

[7] E. Artacho, E. Anglada, O. Diéguez, J. D. Gale, A. García, J. Junquera, R. M. Martin, P. Ordejón, J. M. Pruneda, D. Sánchez-Portal, and J. M. Soler. The SIESTA method; developments and applicability. *J. Phys.: Condens. Matter*, 20:064208, 2008.

[8] H. J. Monkhorst and J. D. Pack. Special points for Brillouin-zone integrations. *Phys. Rev. B*, 13:5188, 1976.

[9] N. Troullier and J. L. Martins. Efficient pseudopotentials for plane-wave calculations. *Phys. Rev. B*, 43:1993, 1991.

[10] J. P. Perdew, K. Burke, and M. Ernzerhof. Generalized gradient approximation made simple. *Phys. Rev. Lett.*, 77:3865, 1996.

[11] P. Janthon, S. M. Kozlov, F. Viñes, J. Limtrakul, and F. Illas. Establishing the accuracy of broadly used density functionals in describing bulk properties of transition metals. *J. Chem. Theory Comput.*, 9:1631, 2013.

[12] F. D. Murnaghan. The compressibility of media under extreme pressures. *Proc. Nat. Acad. Sci.*, 30:244, 1944.

[13] F. Birch. Finite elastic strain of cubic crystals. *Phys. Rev.*, 71:809, 1947.

[14] V. V. Ivanovskaya, A. Zobelli, D. Teillet-Billy, N. Rougeau, V. Sidis, and P. R. Briddon. Hydrogen adsorption on graphene: a first principles study. *Eur. Phys. J. B*, 76:481, 2010.

[15] P. Koskinen, S. Malola, and H. Häkkinen. Self-passivating edge reconstructions of graphene. *Phys. Rev. Lett.*, 101:115502, 2008.

[16] D. C. Elias, R. R. Nair, T. M. G. Mohiuddin, S. V. Morozov, P. Blake, M. P. Halsall, A. C. Ferrari, D. W. Boukhvalov, M. I. Katsnelson, A. K. Geim, and K. S. Novoselov. Control of graphene's properties by reversible hydrogenation: Evidence for graphane. *Science*, 323:610, 2009.

[17] Zhou. S. Y., G.-H. Gweon, A. V. Fedorov, P. N. First, W. A. de Heer, D.-H. Lee, F. Guinea, A. H. Castro Neto, and A. Lanzara. Substrate-induced bandgap opening in epitaxial graphene. *Nature Mater.*, 6:770, 2007.

[18] F. Guinea, M. I. Katsnelson, and A. K. Geim. Energy gaps and a zero-field quantum Hall effect in graphene by strain engineering. *Nature Phys.*, 6:30, 2010.

[19] Y. Zhang, T.-T. Tang, C. Girit, Z. Hao, M. C. Martin, A. Zettl, M. F. Crommie, Y. R. Shen, and F. Wang. Direct observation of a widely tunable bandgap in bilayer graphene. *Nature*, 459:820, 2009.

[20] D. Soriano, N. Leconte, P. Ordejón, J.-C. Charlier, J.-J. Palacios, and S. Roche. Magnetoresistance and magnetic ordering fingerprints in hydrogenated graphene. *Phys. Rev. Lett.*, 107:016602, 2011.

[21] B. Uchoa, C.-Y. Lin, and A. H. Castro Neto. Tailoring graphene with metals on top. *Phys. Rev. B*, 77:035420, 2008.

[22] R. R. Nair, M. Sepioni, I.-L. Tsai, O. Lehtinen, J. Keinonen, A. V. Krasheninnikov, T. Thomson, A. K. Geim, and I. V. Grigorieva. Spin-half paramagnetism in graphene induced by point defects. *Nature Phys.*, 8:199, 2012.

[23] M. M. Ugeda, I. Brihuega, F. Guinea, and J. M. Gómez-Ródriguez. Missing atom as a source of carbon magnetism. *Phys. Rev. Lett.*, 104:096804, 2010.

[24] L. Pisani, J. A. Chan, B. Montanari, and N. M. Harrison. Electronic structure and magnetic properties of graphitic ribbons. *Phys. Rev. B*, 75:064418, 2007.

[25] M. Casartelli, S. Casolo, G. F. Tantardini, and R. Martinazzo. Spin coupling around a carbon atom vacancy in graphene. *Phys. Rev. B*, 88:195424, 2013.

[26] K. Pi, K. M. McCreary, W. Bao, W. Han, Y. F. Chiang, Y. Li, S.-W. Tsai, C. N. Lau, and R. K. Kawakami. Electronic doping and scattering by transition metals on graphene. *Phys. Rev. B*, 80:075406, 2009.

[27] I. Gierz, C. Riedl, U. Starke, C. R. Ast, and K. Kern. Atomic hole doping of graphene. *Nano Lett.*, 8:4603, 2009.

[28] T. Eelbo, M. Waśniowska, P. Thakur, M. Gyamfi, B. Sachs, T. O. Wehling, S. Forti, U. Starke, C. Tieg, A. I. Lichtenstein, and R. Wiesendanger. Adatoms and clusters of $3d$ transition metals on graphene: Electronic and magnetic configurations. *Phys. Rev. Lett.*, 110:136804, 2013.

[29] K. T. Chan, J. B. Neaton, and M. L. Cohen. First-principles study of metal adatom adsorption on graphene. *Phys. Rev. B*, 77:235430, 2008.

[30] C. Cao, M. Wu, J. Jiang, and H.-P. Cheng. Transition metal adatom and dimer adsorbed on graphene: Induced magnetization and electronic structures. *Phys. Rev. B*, 81:205424, 2010.

[31] J. Ding, Z. Qiao, W. Feng, Y. Yao, and Q. Niu. Engineering quantum anomalous/valley Hall states in graphene via metal-atom adsorption: An ab initio study. *Phys. Rev. B*, 84:195444, 2011.

[32] M. Manadé, F. Viñes, and F. Illas. Transition metal adatoms on graphene: A systematic density functional study. *Carbon*, 95:525, 2015.

[33] E. J. G. Santos, A. Ayuela, and D. Sánchez Portal. First-principles study of substitutional metal impurities in graphene: structural, electronic and magnetic properties. *New Journal of Physics*, 12:053012, 2009.

[34] B. Liu and A. D. McLean. Accurate calculation of the attractive interaction of two ground state helium atoms. *J. Chem. Phys.*, 59:4557, 1973.

[35] F. B. van Duijneveldt, J. G. C. M. van Duijneveldt-van de Rijdt, and J. H. van Lenthe. State of the art in counterpoise theory. *Chem. Rev.*, 94:1873, 1994.

[36] R. F. W. Bader. *Atoms in Molecules: Quantum Theory*, volume 22. Oxford Science Publication, 1990.

[37] Y. Mao, J. Yuan, and J. Zhong. Density functional calculation of transition metal adatom adsorption on graphene. *J. Phys.: Condens. Matter*, 20:115209, 2008.

[38] I. Zanella, S. B. Fagan, R. Mota, and A. Fazzio. Electronic and magnetic properties of Ti and Fe on graphene. *J. Phys. Chem. C*, 112:9163, 2008.

[39] H. Sevin cli, M. Topsakal, E. Durgun, and S. Ciraci. Electronic and magnetic properties of 3*d* transition-metal atom adsorbed graphene and graphene nanoribbons. *Phys. Rev. B*, 77:195434, 2008.

[40] H. Johll, H. Cl Kang, and E. S. Tok. Density functional theory study of fe, co, and ni adatoms and dimers adsorbed on graphene. *Phys. Rev. B*, 79:245416, 2009.

[41] L. Hu, X. Hu, X. Wu, C. Du, Y. Dai, and J. Deng. Density functional calculation of transition metal adatom adsorption on graphene. *Physica B*, 405:3337, 2010.

[42] X. Liu, C. W. Wang, Y. X. Yao, W. C. Lu, M. Hupalo, M. C. Tringides, and K. M. Ho. Bonding and charge transfer by metal adatom adsorption on graphene. *Phys. Rev. B*, 83:235411, 2011.

[43] M. Sargolzaei and F. Gudarzi. Magnetic properties of single 3*d* transition metals on graphene and benzene: A density functional theory study. *J. Appl. Phys.*, 110:064303, 2011.

[44] T. O. Wehling, A. I. Lichtenstein, and M. I. Katsnelson. Transition metal adatom and dimer adsorbed on graphene: Induced magnetization and electronic structures. *Phys. Rev. B*, 84:235110, 2011.

[45] X. Liu, C. Z. Wang, M. Hupalo, W. C. Lu, M. C. Tringides, Y. X. Yao, and K. M. Ho. Metals on graphene: correlation between adatom adsorption behavior and growth morphology. *Phys. Chem. Chem. Phys.*, 12:9157, 2012.

[46] H. Valencia, A. Gil, and G. Frapper. Trends in the adsorption of 3d transition metal atoms onto graphene and nanotube surfaces: a DFT and molecular orbital analysis. *J. Phys. Chem. C*, 114:14141, 2010.

[47] B. Cordero, V. Gómez, A. E. Platero-Prats, M. Revés, J. Echeverría, E. Cremades, F. Barragán, and S. Alvarez. *Covalent radii revisited.* Dalton Trans., 2008.

[48] G. Yu, M. Zhu, and Y. Zheng. First-principles study of 3d transition metal atom adsorption onto graphene: the role of the extended line defect. *J. Mater. Chem. C*, 2:9767, 2014.

[49] T. O. Wehling, K. S. Novoselov, S. V. Morozov, E. E. Vdovin, M. I. Katsnelson, A. K. Geim, and A. I. Lichtenstein. Molecular doping of graphene. *Nano Lett.*, 8:173, 2008.

[50] R. Martinazzo, S. Casolo, and G. F. Tantardini. Symmetry-induced band-gap opening in graphene superlattices. *Phys. Rev. B*, 81:245420, 2010.

[51] S. Casolo, R. Martinazzo, and G. F. Tantardini. Band engineering in graphene with superlattices of substitutional defects. *J. Phys. Chem. C*, 115:3250, 2011.

[52] K. Nakada and A. Ishii. First-principles investigation of charge density analysis of various adatom adsorptions on graphene. *AIP Conf. Proc.*, 1399:793, 2011.

[53] D. M. Duffy and J. A. Blackman. Magnetism of 3d transition-metal adatoms and dimers on graphite. *Phys. Rev. B*, 58:7443, 1998.

[54] J. A. Furst, M. Brandbyge, A. Jauho, and K. Stokbro. Ab initio study of spin-dependent transport in carbon nanotubes with iron and vanadium adatoms. *Phys. Rev. B*, 78:195405, 2008.

[55] M. P. Lima, A. J. R. da Silva, and A. Fazzio. Adatoms in graphene as a source of current polarization: Role of the local magnetic moment. *Phys. Rev. B*, 84:245411, 2011.

[56] M. Paulsson. Non Equilibrium Green's Functions for dummies: Introduction to the one particle NEGF equations. *arXiv:cond-mat/0210519*, 2008.

[57] M. Brandbyge, J.-L. Mozos, P. Ordejón, J. Taylor, and K. Stokbro. Density-functional method for nonequilibrium electron transport. *Phys. Rev. B*, 65:165401, 2002.

[58] C. D. Porter and D. Stroud. Clustering and magnetic anisotropy of Fe adatoms on graphene. *Phys. Rev. B*, 85:235452, 2012.

[59] W. Kohn and K.-H. Lau. Adatom dipole moments on metals and their interactions. *Solid State Comm.*, 18:553, 1976.

[60] K.-H. Lau and W. Kohn. Indirect long-range oscillatory interaction between adsorbed atoms. *Surf. Sci.*, 18:69, 1978.

[61] E. Wahlström, I. Ekvall, H. Olin, and L. Walldén. Long-range interaction between adatoms at the Cu(111) surface imaged by scanning tunneling microscopy. *Appl. Phys. A*, 66:S1107, 1998.

[62] M. A. Ruderman and C. Kittel. Indirect exchange coupling of nuclear magnetic moments by conduction electrons. *Phys. Rev.*, 96:99, 1954.

[63] T. Kasuya. A theory of metallic ferro- and antiferromagnetism on Zener's model. *Prog. Theor. Phys.*, 16:45, 1956.

[64] K. Yosida. Magnetic properties of Cu-Mn alloys. *Phys. Rev.*, 106:893, 1957.

[65] R. Landauer. Spatial variation of currents and fields due to localized scatterers in metallic conduction. *IBM J. Res. Dev.*, 1:233, 1957.

[66] C. Caroli, R. Combescot, P. P. Nozieres, and D. Saint-James. Direct calculation of the tunneling current. *J. Phys. C: Solid State Phys.*, 4:916, 1970.

[67] D. S. Fisher and P. A. Lee. Relation between conductivity and transmission matrix. *Phys. Rev. B*, 23:6851, 1981.

[68] U. Fano. Effects of configuration interaction on intensities and phase shifts. *Phys. Rev.*, 124:1866, 1961.

[69] J. U. Nöckel and A. D. Stone. Resonance line shapes in quasi-one-dimensional scattering. *Phys. Rev. B*, 50:17415, 1994.

[70] B. J. van Wees, H. van Houten, C. W. J. Beenakker, J. G. Williamson, L. P. Kouwenhoven, D. van der Marel, and C. T. Foxon. Quantized conductance of point contacts in a two-dimensional electron gas. *Phys. Rev. Lett.*, 60:848, 1988.

[71] A. Otero-de-la Roza and V. Johnson, E. R.and Luaña.

[72] H. Song, Y. Kim, Y. H. Jang, M. A. Jeong, M. A. Reed, and T. Lee. Observation of molecular gating. *Nature*, 462:1039, 2009.

[73] M. Misiorny and J. Barnaś. Magnetic switching of a single molecular magnet due to spin-polarized current. *Phys. Rev. B*, 75:134425, 2007.

[74] N. J. Tao. Probing potential-tuned resonant tunneling through redox molecules with scanning tunneling microscopy. *Phys. Rev. Lett.*, 76:4066, 1996.

[75] J. E. Green, J. W. Choi, A. Boukai, Y. Bunimovich, E. Johnston-Halperin, E. DeIonno, Y. Luo, B. A. Sheriff, K. Xu, Y. S. Shin, H.-R. Tseng, J. F. Stoddart, and J. R. Heath. A 160-kilobit molecular electronic memory patterned at 10^{11} bits per square centimetre. *Nature*, 445:414, 2007.

[76] C. Benesch, M. F. Rode, M. Čížek, R. Härtle, O. Rubio-Pons, M. Thoss, and A. L. Sobolewski. Switching the conductance of a single molecule by photoinduced hydrogen transfer. *J. Phys. Chem. C*, 113:10315, 2009.

[77] A. R. Rocha, V. M. Garcia-Suarez, S. W. Bailey, C. J. Lambert, J. Ferrer, and S. Sanvito. Towards molecular spintronics. *Nature Mater.*, 5:335, 2005.

[78] S. Sanvito. Spintronics goes plastic. *Nature Mater.*, 6:803, 2007.

[79] G. Szulczewski, S. Sanvito, and M. Coey. A spin of their own. *Nature Mater.*, 8:693, 2009.

[80] S. Sanvito. Molecular spintronics. *Chem. Soc. Rev.*, 40:3336, 2011.

[81] S. U. Lee, R. V. Belosludov, H. Mizuseki, and Y. Kawazoe. The role of aromaticity and the π-conjugated framework in multiporphyrinic systems as single- molecule switches. *Small*, 7:962, 2008.

[82] J. Huang, W. Wang, S. Yang, H. Su, Q. Li, and J. Yang. A theoretical study of spin-polarized transport properties of planar four-coordinate Fe complexes. *Chem. Phys. Lett.*, 539:102, 2012.

[83] J. Huang, K. Xu, Lei S., H. Su, S. Yang, Q. Li, and J. Yang. Iron-phthalocyanine molecular junction with high spin folter efficiency and negative differential resistance. *J. Chem. Phys.*, 136:064707, 2012.

[84] J. Huang, W. Wang, S. Yang, Q. Li, and J. Yang. Efficient spin filter based on FeN_4 complexes between carbon nanotube electrodes. *Nanotechnology*, 23:255202, 2012.

[85] N. Wang, H. Liu, J. Zhao, Y. Cui, Z. Xu, Y. Ye, M. Kiguchi, and K. Murakoshi. Theoretical investigation on the electron transport path through the porphyrin molecules and chemisorption of CO. *J. Phys. Chem. C*, 113:7416, 2009.

[86] H. Kondo, J. Nara, and T. Ohno. Possibility of gas sensor using electronic transport properties of iron-porphyrin molecular junction system. *J. Phys. Chem. C*, 115:6886, 2011.

[87] Y. W. Li, J. H. Yao, C. J. Liu, J. W. Yang, and C. L. Yang. Theoretical investigation of the O_2 adsorption effect in the electron transport of single Fe-porphyrin molecule. *Phys. Lett. A*, 373:3974, 2009.

[88] K. Toyoda. Theoretical investigation of chemical spin doping into single porphyrin junctions toward ultrahigh-sensitive nitric oxide sensor. *Jpn. J. Appl. Phys.*, 51:045202, 2012.

[89] E. Lörtscher. Wiring molecules into circuits. *Nature Nanotech.*, 8:381, 2013.

[90] C. Bruot, J. Hihath, and N. Tao. Mechanically controlled molecular orbital alignment in single molecule junctions. *Nature Nanotech.*, 7:35, 2011.

[91] W. Liang, M. O. Shores, M. Bockrath, J. R. Long, and H. Park. Kondo resonance in a single-molecule transistor. *Nature*, 417:725, 2002.

[92] C. M. Guédon, H. Valkenier, T. Markussen, K. S. Thygesen, J. C. Hummelen, and S. J. van der Molen. Observation of quantum interference in molecular charge transport. *Nature Nanotech.*, 7:305, 2012.

[93] R. M. Metzger, B. Chen, U. Höpfner, M. V. Lakshmikantham, D. Vuillaume, T. Kawai, X. Wu, H. Tachibana, T. V. Hughes, H. Sakurai, J. W. Baldwin, C. Hosch, M. P. Cava, L. Brehmer, and G. J. Ashwell. Unimolecular electrical rectification in hexadecylquinolinium tricyanoquinodimethanide. *J. Am. Chem. Soc.*, 119:10455, 1997.

[94] S. Kubatkin, A. Danilov, M. Hjort, J. Cornil, J.-L. Brédas, N. Stuhr-Hansen, P. Hedegard, and T. Bjornholm. Single-electron transistor of a single organic molecule with access to several redox states. *Nature*, 425:698, 2003.

[95] S. Y. Quek, M. Kamenetska, M. L. Steigerwald, H. J. Choi, S. G. Louie, M. S. Hybertsen, Neaton J. B., and L. Venkataraman. Mechanically-controlled binary conductance switching of a single-molecule junction. *Nature Nanotech.*, 4:230, 2009.

[96] S. Thiele, F. Balestro, R. Ballou, S. Klyatskaya, M. Ruben, and W. Wernsdorfer. Electrically driven nuclear spin resonance in single-molecule magnets. *Science*, 344:1135, 2014.

[97] G. V. Nazin, X. H. Qiu, and W. Ho. Visualization and spectroscopy of a metal-molecule-metal bridge. *Science*, 302:77, 2003.

[98] X. Guo, J. P. Small, J. E. Klare, Y. Wang, M. S. Purewal, I. M. Tam, B. H. Hong, R. Caldwell, L. Huang, S. O'Brien, J. Yan, R. Breslow, S. J. Wind, J. Hone, P. Kim, and C. Nuckolls. Covalently bridging gaps in single-walled carbon nanotubes with conducting molecules. *Science*, 311:356, 2006.

[99] C. W. Marquardt, S. Grunder, A. Baszczyk, S. Dehm, F. Hennrich, H. von Lhneysen, M. Mayor, and R. Krupke. Electroluminescence from a single nanotube-molecule-nanotube junction. *Nature Nanotech.*, 5:863, 2010.

[100] F. Prins, A. Barreiro, J. W. Ruitenberg, J. S. Seldenthuis, N. Aliaga-Alcalde, L. M. K. Vandersypen, and H. S. J. van der Zant. Room-temperature gating of molecular junctions using few-layer graphene nanogap electrodes. *Nano Lett.*, 11:4607, 2011.

[101] D. H. Lee, W. J. Lee, W. J. Lee, S. O. Kim, and Y.-H. Kim. Theory, synthesis and oxygen reduction catalysis of Fe-porphyrin-like carbon nanotube. *Phys. Rev. Lett.*, 106:175502, 2011.

[102] M.-S. Liao, J. D. Watts, and M. J. Huang. Fe^{II} in different macrocycles: Electronic structures and properties. *J. Phys. Chem. A*, 109:7988, 2005.

[103] T. Wassmann, A. P. Seitsonen, A. M. Saitta, M. Lazzeri, and F. Mauri. Structure, stability, edge states, and aromaticity of graphene ribbons. *Phys. Rev. Lett.*, 101:096402, 2008.

[104] L. S. Panchakarla, K. S. Subrahmanyam, S. K. Saha, A. Govindaraj, H. R. Krishnamurthy, U. V. Waghmare, and C. N. R. Rao. Synthesis, structure, and properties of boron- and nitrogen-doped graphene. *Adv. Mater.*, 21:4726, 2009.

[105] A. Lherbier, X. Blase, Y.-M. Niquet, F. Triozon, and S. Roche. Charge transport in chemically doped 2D graphene. *Phys. Rev. Lett.*, 101:036808, 2008.

[106] Y.-C. Lin, C.-Y. Lin, and P.-W. Chiu. Controllable graphene N-doping with ammonia plasma. *Appl. Phys. Lett.*, 96:133110, 2010.

[107] J. Park, A. N. Pasupathy, J. I. Goldsmith, C. Chang, Y. Yaish, J. R. Petta, M. Rinkoski, J. P. Sethna, H. D. Abruña, P. L. McEuen, and D. C. Ralph. Coulomb blockade and the Kondo effect in single-atom transistors. *Nature*, 417:722, 2002.

[108] Y. Chen, A. Prociuk, T. Perrine, and B. D. Dunietz. Spin-dependent electronic transport through a porphyrin ring ligating an Fe^{II} atom: An ab initio study. *Phys. Rev. B*, 74:245320, 2006.

[109] Y. Okuno and S. Yokoyama. Theoretical study of molecular rectification in porphyrin dimer. *Thin Solid Films*, 516:2630, 2008.

[110] K. Salazar-Salinas, L. A. Jauregui, C. Kubli-Garfias, and J. M. Seminario. Molecular biosensor based on a coordinated iron complex. *J. Chem. Phys.*, 130:105101, 2009.

[111] C. Rovira, P. Ballone, and M. Parrinello. A density functional study of iron-porphyrin complexes. *Chem. Phys. Lett.*, 271:247, 1997.

[112] M. Momenteau and C. A. Reed. Synthetic heme dioxygen complexes. *Chem. Rev.*, 94:659, 1994.